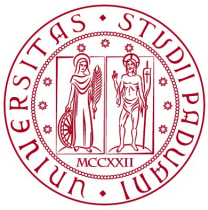

UNIVERSITÀ
DEGLI STUDI
DI PADOVA

Sede Amministrativa: Università degli Studi di Padova
Dipartimento di Ingegneria Industriale

Scuola di Dottorato di Ricerca in: Ingegneria Industriale
Indirizzo: Ingegneria dell'Energia
Ciclo: XXVII

HIGH PERFORMANCE WATERJETS: STUDY OF AN INNOVATIVE SCOOP INLET AND DEVELOPMENT OF A NOVEL METHOD TO DESIGN DUCTED PROPELLERS

Direttore della Scuola : Ch.mo Prof. Paolo Colombo

Coordinatore d'indirizzo: Ch.ma Prof.ssa Luisa Rossetto

Supervisore :Ch.mo Prof. Ernesto Benini

Dottorando : Davide Papale

Alla mia famiglia

Sommario

Il documento riassume il progetto di dottorato sugli idrogetti ad alte prestazioni condotto dall'autore nel periodo che va dal 2012 al 2014. Durante il triennio sono stati affrontati due filoni principali di ricerca riguardo questi propulsori, focalizzandosi in particolare sullo studio dell'imbocco e del sistema pompante.

Un idrogetto è una propulsore navale che riesce a produrre una forza propulsiva accelerando una massa d'acqua; durante questo processo la massa d'acqua, originariamente presente libera nell'ambiente marino o fluviale, attraversa quattro diversi componenti: l'imbocco, il sistema pompante, l'ugello e il sistema sterzante. Ogni componente possiede una sua funzionalità ma in generale massimizzando l'efficienza di questi componenti è possibile osservare un generico aumento delle prestazioni complessive. Il lavoro qui presentato si è focalizzato sullo studio dell'imbocco e del sistema pompante; volendo essere di carattere innovativo, le configurazioni e le idee qui presentate rappresentano delle alternative costruttive o metodologiche sostanzialmente differenti dalla comune prassi industriale.

Lo studio dell'imbocco ha avuto come linea guida il confronto tra un imbocco commerciale di stampo tradizionale (i cosiddetti imbocchi flush) e un imbocco dinamico di derivazione aeronautica (imbocchi scoop). Lo studio, oltre a rappresentare forse l'unico caso in letteratura di studio specifico su imbocchi dinamici, mette in luce le criticità dell'imbocco tradizionale mostrando una via alternativa alla prassi industriale. Lo studio analizza le performance in termini di perdite di pressione totali e fattore di distorsione di questi due imbocchi, con e senza la presenza dell'albero di trasmissione, attraverso diverse analisi CFD. Interessante è la derivazione aeronautica dell'imbocco dinamico preso “in prestito” da studi NASA riguardanti un imbocco per un aereo sperimentale caratterizzato da importanti spessori dello strato limite. Lo studio dimostrerà, per il caso in analisi, la superiorità dell'imbocco dinamico rispetto a quello tradizionale nei termini di paragone sopra descritti, dimostrando la necessità di affrontare con critico approfondimento lo studio degli imbocchi sugli idrogetti in ambito industriale, rimettendo in discussione molti dogmi dati per scontati nella

realtà industriale ma in verità mai dimostrati nella letteratura scientifica.

Lo studio dell'apparato pompante è stato affrontato in due fasi, la prima squisitamente teorica , la seconda di carattere sperimentale. La fase teorica ha visto la definizione di un nuovo metodo per la progettazione di un apparato pompante assiale. Il metodo, che è stato successivamente implementato in un programma Matlab e validato, è un metodo di carattere generale frutto della combinazione di diversi metodi analitici già utilizzati in letteratura ma in maniera concettualmente differente; anche se sviluppato originariamente per una pompa di un idrogetto, è stato pensato per avere una validità generale e può essere utilizzato per lo studio di una qualsiasi pompa assiale intubata. Il metodo rappresenta una combinazione di un metodo BEM (Blade Element Momentum) con due teorie analitiche per il calcolo dei coefficienti di portanza e resistenza dei profili alari (Weinig e Lieblein) e dell'equazione di Eulero per le turbomacchine. Il metodo risultante è un metodo fortemente iterativo che permette di calcolare la geometria di una pompa assiale intubata e le sue prestazioni anche fuori dal punto di progetto senza la necessità di utilizzare fattori empirici di discutibile attendibilità; esso si dimostra quindi un metodo innovativo e flessibile per lo studio completo di un generico propulsore intubato. Il metodo è stato implementato e testato sia numericamente che sperimentalmente grazie alla collaborazione della “University of Southampton” e della ditta “TSL Technology” su un propulsore elettrico attuato in periferia. Il propulsore in questione fa parte di una classe di propulsori di nuova concezione meglio conosciuti come RDP (Rim Driven Propeller) che fra le varie caratteristiche hanno quella di abbandonare la necessità di un albero per la trasmissione della coppia motrice con la conseguente assenza delle perdite dovute alla presenza dell'albero immerso nel flusso dell'acqua. La realizzazione sperimentale di questo propulsore, oltre ad aver sensibilmente migliorato l'efficienza del propulsore rispetto a quelli sviluppati in passato dalla ditta coinvolta, ha dimostrato l'attendibilità del modello analitico sviluppato.

Abstract

In the last decades the diffusion of waterjet systems for commercial applications in the high speed field is on the increase. These marine propulsors show remarkable qualities in terms of fuel consumption, noise, vibrations and manoeuvrability but they have some disadvantages which make their use optimal only for a limited speed range and which limit the overall propulsive efficiency. In the present document is described a way to modify a conventional waterjet with the aim of reducing these problems, increasing the overall efficiency.

Many problems are dealt with. In chapter 3 it is shown how the substitution of a conventional flush inlet with a new scoop inlet could be an efficient way to minimise the total pressure losses and the non-uniformity velocity distribution upstream the pump, limiting in this way the influence of the boundary layer ingestion on the machine performance. In chapter 4 a novel method to study and design axial pumps is developed and explained. In chapter 5 a rim driven propeller is designed and tested numerically and experimentally demonstrating the good prediction capabilities of the method.

Page intentionally left blank

Table of Contents

Page intentionally left blank

Table of Figures

Nomenclature

Latin letters

a	Free-vortex coefficient	[unitless]
A_{1p}	Projection of the inlet area	[m^2]
A_i	Area of section i	[m^2]
A_R	Actuator disk area of the rotor	[m^2]
A_S	Actuator disk area of the stator	[m^2]
b	Forced-vortex coefficient	[unitless]
C_d	Aerodynamic drag coefficient	[unitless]
$\hat{c}_i$	Area averaged velocity at section i	[m/s]
$\bar{c}_i$	Mass flow averaged velocity at section i	[m/s]
C_l	Aerodynamic lift coefficient	[unitless]
$\bar{c}_{zi}$	Mass flow averaged velocity in the axial direction at section i	[m/s]
$\bar{c}_{\vartheta i}$	Mass flow averaged tangential speed at i section	[m/s]
D	Pump diameter	[m]
$DPCP_{avg}$	average SAE circumferential distortion descriptor	[unitless]
F	Designed thrust	[N]
$f(\theta_i)$	Extent function	[unitless]
F_{ST}	Frictional wall forces	[N]
g	Gravitational acceleration	[m/s^2]
$g(\theta_i)$	Extent function	[unitless]
H	Hydraulic head	[m]
h	Suction depth	[m]
H_t	Theoretical hydraulic head	[m]
h^T	Total enthalpy	[J/kg]
i	Generic section index	[unitless]
I_p	Phase current	[A]
k	Constant-vortex coefficient	[unitless]
K_{cl}	Core loss coefficient	[W $(min/rev)^{1.6}$]

l	Aerofoil chord	[m]
l	Stage length	[m]
$\dot{m}$	Mass flow rate	[kg/s]
N	Rotational speed	[rad/s]
n	Constant dependent from Reynolds number	[unitless]
n	Exponent of power law profile	[unitless]
N_s	Specific speed	[unitless]
$\bar{p}_i^0$	Mass flow average total pressure, at section i	[Pa]
p_a	Ambient static pressure	[Pa]
$p_{avg,i}$	Area average total pressure for the ring i on the pump interface	[Pa]
$\hat{p}_i$	Area average static pressure, at section i	[Pa]
p_i^0	Total pressure at section i	[Pa]
$p_{l,avg,i}$	Area average total pressure in the low-pressure region (defined by extent) for the ring i on the pump interface	[Pa]
$p_{t,2,avg}$	Area averaged total pressure at the pump interface	[Pa]
Q	Volumetric flow rate	[m^3/s]
q	Steady-state dynamic pressure	[Pa]
r	Radius	[m]
r	Generic radius	[m]
R_c	Copper resistance	[Ω]
Re	Reynolds number	[unitless]
$r_{e,i}$	External radius at section i	[m]
$r_{i,i}$	Internal radius at section i	[m]
R_{mean}	Mean radius	[m]
RPM	Revolution per minute	[rev min^{-1}]
S	Designed thrust	[N]
T	Designed thrust	[N]
$T_{bearing}$	Bearing friction torque	[N m]
T_{duct}	Thrust generated by the duct	[N]
T_{pump}	Thrust generated by the pump	[N]

u_∞	Free stream velocity	[m/s]
u_j	Average velocity at outlet location	[m/s]
u_w	Average velocity at wake location	[m/s]
v_∞	Free stream velocity	[m/s]
v_a	Speed of advance	[m/s]
v_{inlet}	Average velocity at inlet location	[m/s]
v_{pump}	Average velocity at pump location	[m/s]
v_{ship}	Free stream velocity	[m/s]
Y	Distance from the wall	[m]

Greek letters

α_0	Zero lift angle	[°]
β_1	Relative velocity angle at the leading edge	[°]
β_2	Relative velocity angle at the trailing edge	[°]
β_e	Relative velocity angle at the trailing edge	[°]
β_{inf}	Average relative velocity angle	[°]
δ	Local boundary layer thickness	[m]
ΔH_{loss}	Hydraulic head losses	[m]
η^R_{hyd}	Hydraulic efficiency of the rotor	[unitless]
η_{st}	Static pressure ratio	[unitless]
θ	Circumferential extent element that is the angular region in degrees in which ring pressure is below the average pressure of the pump interface	[°]
λ	Empirical value	[unitless]
ρ	Density	[kg/m^3]
τ	Thrust ratio	[unitless]
υ	Kinematic viscosity	[m^2/s]

Page intentionally left blank

Acronyms

AIP	Aerodynamic Interface Plane
BEM	Blade Element Momentum
BET	Blade Element Theory
BLI	Boundary Layer Ingesting
CAD	Computer-Aided Design
CFD	Computational Fluid Dynamic
IBLM	Integral Boundary Layer Method
IVR	Intake velocity ratio
NPSH	Net Positive Suction Head
OPC	Overall Propulsive Efficiency
RANS	Reynolds-Averaged Navier-Stokes
RDP	Rim Driven Propeller
RPM	Revolution per minute
SAE	Society of Automotive Engineers
SES	Surface Effect Ship
SST	Shear Stress Transport

Page intentionally left blank

1. Introduction

A waterjet system is a marine propulsor that creates a high speed jet of water for propulsion; the first concept of waterjet was developed by Toogood and Hays in the early 17h century, but for a long time its use has been confined to small high-speed crafts and work boats because screw propellers were generally considered simpler, lighter and more efficient [1]. From 1980 onwards, the use of waterjets in commercial applications really started to grow [2] due to the high request of high speed and high manoeuvrability crafts. Nowadays they are typically used for applications in the speed range of 15-25m/s, where they are more attractive for designers compared to open propellers because of their higher Overall Propulsive Efficiency (OPC); in this speed range waterjet systems equipped with mixed flow pump impellers can give an OPC in the range 0.5-0.75 [3]. An interesting parallel can be recognised considering aeronautical applications, where propellers have been replaced by jet engines in order to achieve higher speed. In the marine industry, a similar trend is envisaged where waterjets substituting screw propeller in the high speed field [4]. Compared to conventional screw propellers, a waterjet system has several advantages: reduced fuel consumption at high speed, reduced noise and vibrations, improved manoeuvrability, etc. but also some disadvantages; the most important are the lower efficiency at low speed (lower than 10m/s), the bigger weight and the greater cost [5]. In addition to these drawbacks, other problems are widely recognised in limiting the efficiency and the usability of waterjet systems: the boundary layer ingestion, the non-uniformity velocity distribution upstream of the pump, the risk of cavitation in high loaded applications and a non-friendly procedure to start the system at zero speed.

The aim of this Ph.D. thesis was to find a way to limit the impact of these problems to obtain in the near future a new class of waterjets capable of increasing the conventional speed range with a higher propulsive efficiency and a lower power consumption. Achieving these objectives could represent a significant improvement in marine transportation.

Latest literature references and recommendations about waterjet propulsion may be found in [6] and [7].

1.1. Waterjet system

A typical waterjet can be divided in four components: inlet, pump, nozzle and steering device (Fig. 1).

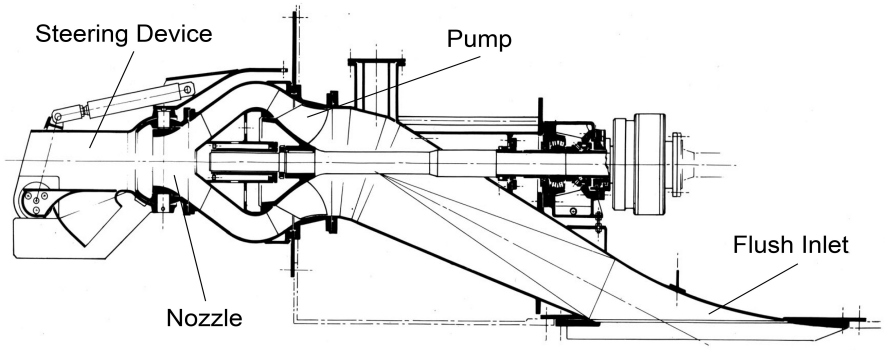

Figure 1: Waterjet geometry; from [8]

1.2. Inlet

The inlet is a water intake; it is essentially a duct that connects the pump, which is usually placed inside the hull, with the external environment and then the water. There are three classes of inlets: flush inlets, ram (or pod) inlets and scoop inlets. The first type is the most used in nowadays waterjets; its inlet entrance is parallel to the water flow and any sort of drag appendages or supports protrude into the water. Such inlets are characterized by a quite high performance at the design point operating condition but, as velocity departs from the cruise speed, negative behaviours may occur.

Defining:

$$IVR = \frac{v_{ship}}{v_{pump}} \tag{1.1}$$

where v_{pump} is the averaged axial inflow water velocity at the pump section, it is possible to observe that at relatively low ship speed IVR is smaller than 1; this condition might lead to cavitation and/or separation at the inlet location on the upper side of the lip (fig. 2 up). On the contrary at high speed (>30m/s) IVR is higher than 2.

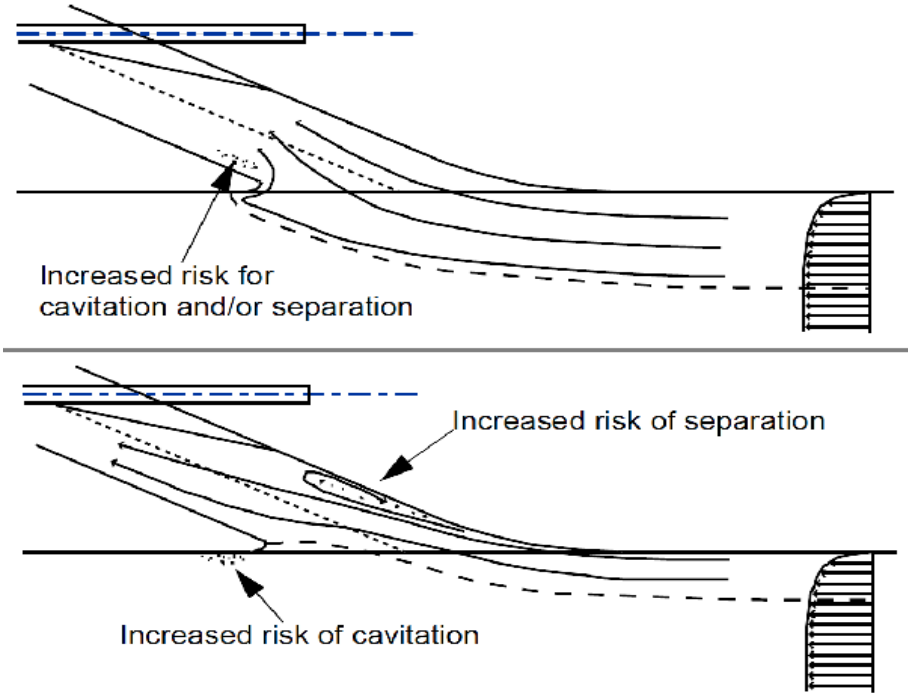

Figure 2: Flow phenomena at low IVR (up) and at high IVR (down); from [1]

For this reason the hull side of the lip may become susceptible of cavitation and, if the adverse pressure gradient created by the deceleration becomes too large, flow separation might occur at the top side of the inlet (fig. 2 down).

Ram (or pod) and scoop inlets have the entrance more or less perpendicular to the flow direction (see fig. 3). A ram inlet has the opening deep under the hull surface to capture the water from an area undisturbed by hull boundary layer and to prevent the air ingestion in those fast ferries, like SES (surface effect ship) or hydrofoils, that otherwise will have the opening of the inlet too close to the waterline. Due the protruding parts submerged in the water, ram inlets suffer from high drag and then they are usually used only when the disadvantages due to the air ingestion or to the interaction between hull and the hull boundary layer are considered too serious. On the other hand scoop inlets represent a hybrid form between ram and flush intakes; nowadays they are rarely employed even though there is not a clear explanation for such tendency. In fact, as it is clearly demonstrated in chapter 3, scoop inlets are appealing in terms of minimization of both the flow distortion and total pressure loss.

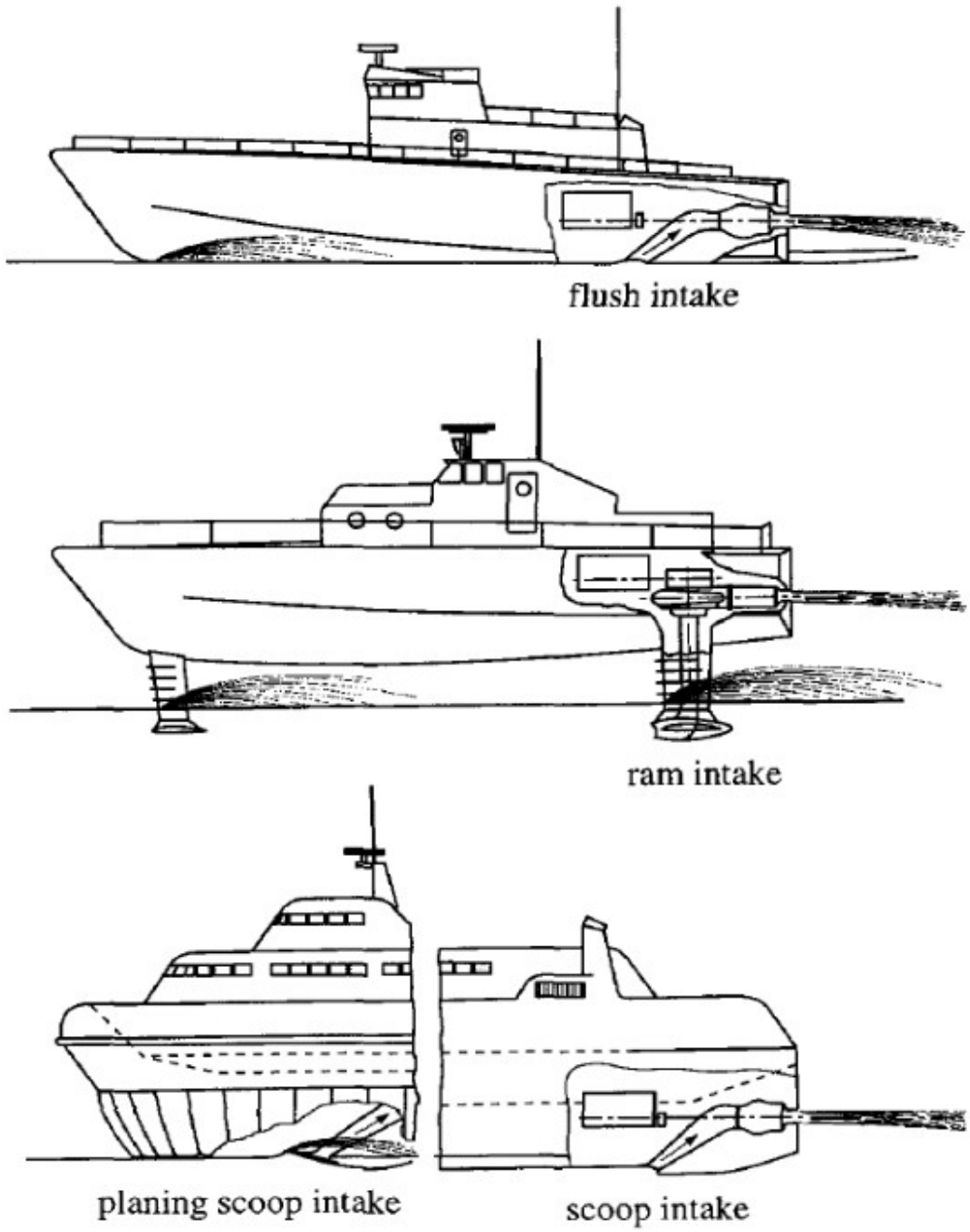

Figure 3: Basic intake concept, from [10]

1.3. Pump

The main component of a waterjet system is the pump, which produces the hydraulic head necessary to accelerate the jet of water at the nozzle exit. Different types of pumps can be used for this purpose: centrifugal pumps, axial pumps or mixed pumps, which are characterized by radial, axial and mixed flow, respectively. Centrifugal pumps exploit centripetal acceleration to generate pressure that is converted into velocity thanks to the nozzle. The main drawback is related with the low mass flow rate that can be elaborated: compared to an axial pump, for the same thrust and power unit, the centrifugal pumps are generally larger and heavier. Axial pumps increase flow pressure by diffusing the fluid while it is passing through the impeller blades and stator vanes; axial pumps output is characterized by high flow and a low pressure ratio that makes axial pump recommended for waterjet applications; compared to centrifugal pumps, axial pumps are usually lighter, smaller and run at higher rpm. Mixed pumps incorporate features of both centrifugal and axial pumps; the characteristics of these pumps may vary according to the design.

The pump configuration adopted for a waterjet system can be related with the specific speed of the pump:

$$N_s = \frac{N Q^{1/2}}{g H^{3/4}} \tag{1.2}$$

where Q is the volumetric flow rate, N is the rotational speed, g the gravitational acceleration and H is the hydraulic head. Pure centrifugal pumps are usually adopted for low values of specific speed whereas for high values of N_s pure axial pumps are normally used [9]. There is a limit to how much the flow can be diffused before flow separation or flow cavitation occurs, resulting in a loss of thrust. For this reason high loaded waterjets in use today usually use mixed flow pump units.

1.4. Nozzle

The function of the nozzle is to convert the static pressure of the water at the pump exit into kinetic energy, in order to produce the axial thrust through the evacuation of the water jet. This conversion can be studied, with good approximation, by one-dimensional gas dynamic equations assuming the process as isentropic. Nozzles used for waterjets are clearly converging nozzles because of the subsonic speed of the water flow.

1.5. Steering device

Waterjet systems may be provided with rotating nozzles and deflector vanes to redirect the water jet with the aim to produce turning force or reverse thrust. At full power, the side force generated by a jet deflection of 6° can reach the 10% of the total force; the available reverse thrust may be expected to be 30-40% of the maximum static thrust for the system [3].

This device represent a marked improvement over screw propeller and allow to have ships with a very high manoeuvrability. In the next figure it is possible to see a steering device in different operating conditions.

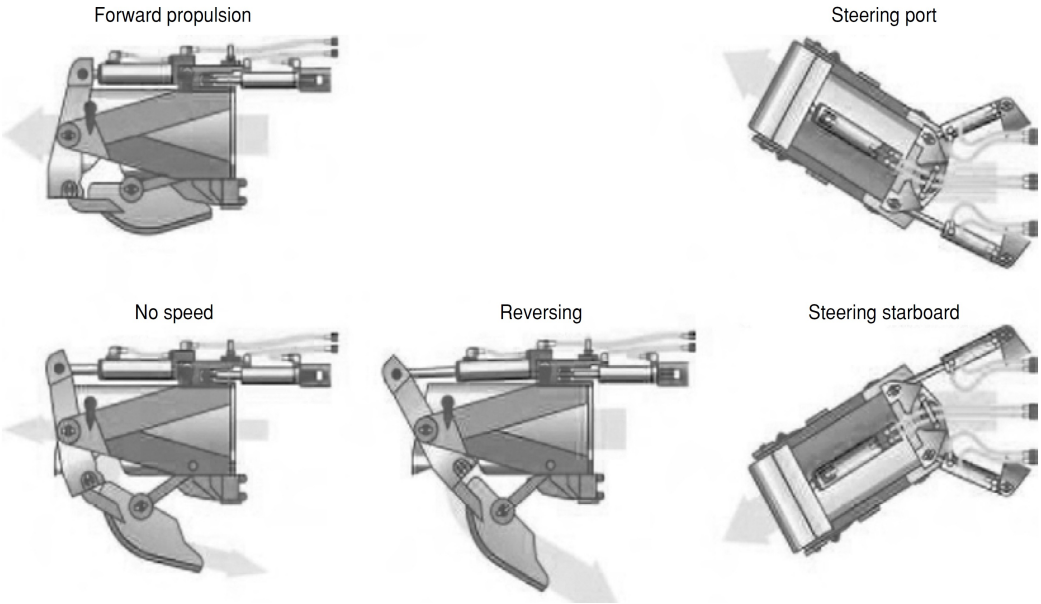

Figure 4: Steering device; from [11]

1.6. References

[1] J. Carlton, **Marine Propellers and Propulsion,** Butterworth-Heinemann, 2007.

[2] N. F. Warren & N. Sims, **Waterjet propulsion, a shipbuilder's view,** Proceedings RINA Waterjet Propulsion Conference, London, 1994.

[3] L. Yun & A. Bliaut, **Theory Design Air Cushion Craft**, Arnold, 2000

[4] N. W. H. Bulten, **Numerical Analysis of a Waterjet Propulsion System**, Ph.D. thesis, Eindhoven University of Technology, 2006.

[5] J. Allison et al., **Marine Waterjet Propulsion**, SNAME Transactions, Vol. 101, pp. 275-335, 1993.

[6] ITTC, **Report of the Specialist Committee on Validation of Waterjet Test Procedures**, Proceedings of 24th International Towing Tank Conference, Vol. II, Edinburgh, 2005.

[7] ITTC, **Recommended Procedures and Guidelines**, 26th International Towing Tank Conference, section 7.5-02-05, Rio de Janeiro, 2011.

[8] C. Katsavos et al., **Analisi fluidodinamica e simulazione CFD dell'idrogetto Castoldi turbodrive 340 HC**, Master degree thesis, University of Padova, 2012.

[9] A. F. Molland, **The Maritime Engineering Reference Book: a Guide to Ship Design Construction and Operation**, Butterworth-Heinemann, pp 356-357, 2008.

[10] C. Kruppa et al., **Wasserstrahlantriebe für Hochgeschwindigkeitsfahrzeuge**, Jahrbuch der STG 62, Band 1968, Nov., pp. 228-258, 1968.

[11] O. M. Faltinsen, **Hydrodynamics of High-Speed Marine Vehicles,** Cambridge University Press, 2010.

Page intentionally left blank

2. Inlet Hydrodynamics

In the design of a reliable and efficient waterjet system, among all the design specifications and variables, important phenomena must be carefully analysed otherwise they may affect the correct functioning of the pump system and cause detrimental energy losses. The effects of these phenomena, which are described in the next paragraph, could be more or less relevant at different cruise speeds and they usually cannot be totally prevented; it is then very important to minimize them in order to achieve the best overall efficiency possible. In addition to the total pressure loss, the main consequence of these phenomena is the distortion of the flow entering the pump that could generate an unsteady loading of the rotor blades increasing the risk of cavitation at the rotor location.

2.1. Inlet/Pump Compatibility and Hydrodynamic Inlet Losses

The function of an inlet is to supply the water flow rate to the pump system with an adequate pressure recovery and to minimize the flow distortion and losses at the pump interface. The sources of distortion and losses are many; some are the same you can encounter in air intakes, others are peculiar only of water inlets. The most relevant are depicted in fig. 5; they can be summarised as:

- Duct flow separation;
- Lip separation;
- Boundary layer profile distension on the inside walls of the duct;
- Wall separation from high diffusion rates;
- Boundary layer ingestion generated by the presence of the hull;
- Cavitation at lip or hull side;
- Swirl of the flow entering the pump;
- Losses induced by the drive shaft.

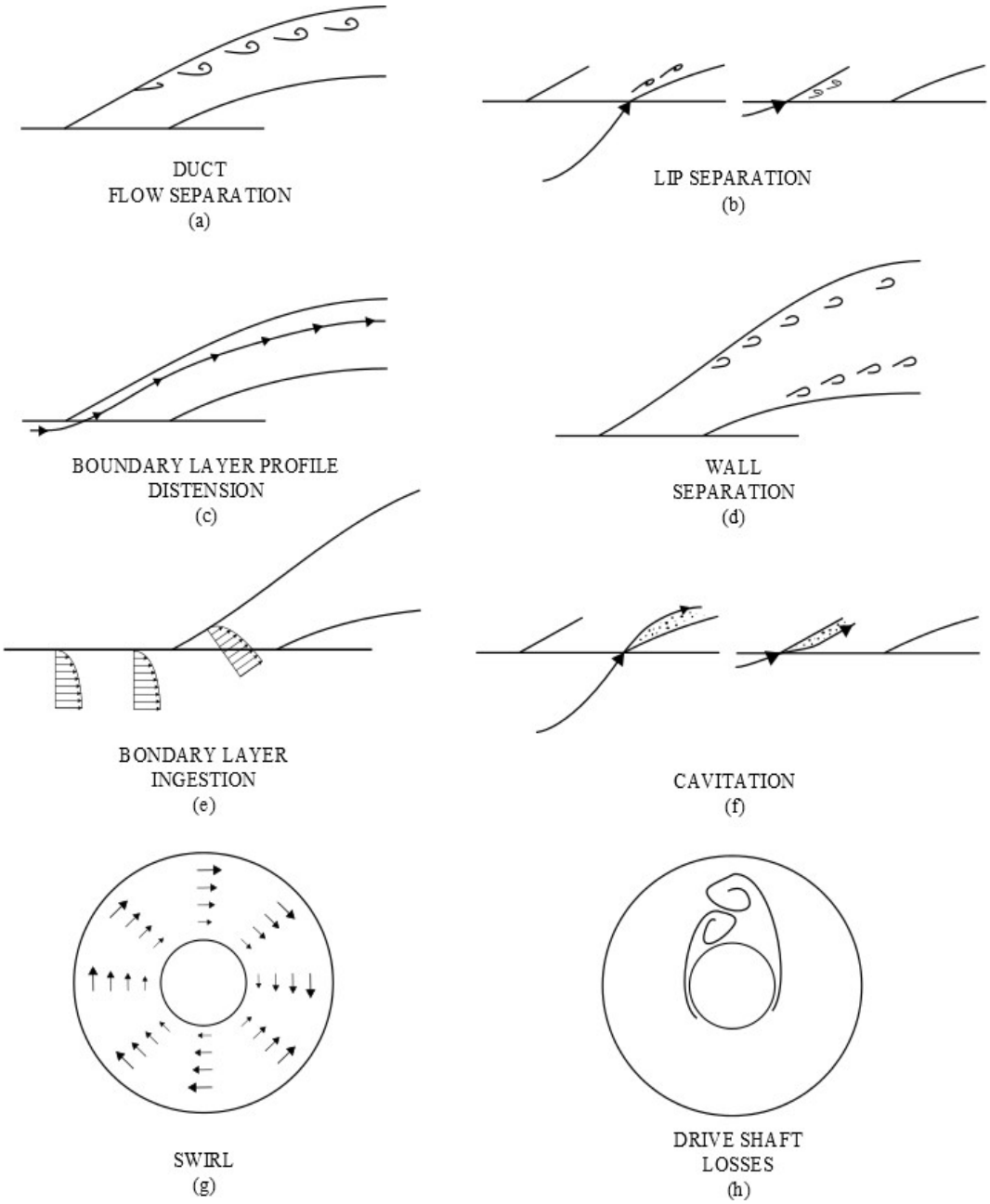

Figure 5: (a) - (h) Source of distortion and losses

Duct flow separation (a), lip separation (b) and wall separation (c) are sources of distortion which arise with a fluid separation phenomenon. Duct flow separation appears in curved diffusers when there is a sudden variation of the duct slope. Lip separation arises when the incidence angle of the duct is too high with respect to the fluid direction; this phenomenon is similar to the stall of an aerofoil. Wall separation (c) appears when the diffusion rates of the intake is too hight. “In separated flow conditions, the intake distortion can be highly turbulent and have eddy sizes sufficiently large to contribute significantly to the spatial distribution of the total pressure at the engine entry plane” [1]. This could cause the malfunctioning of the pump and the decreasing of the overall efficiency; therefore, in the design procedure the incidence of the duct, the internal area variation and the lip angle of attack should be carefully chosen.

The boundary layer profile distension (c) is the relaxation of the fluid velocity profile and it is usually more evident on the inside walls of bends. The boundary layer ingestion (e) is the ingestion of water from the boundary layer of the hull; the contribution of these two phenomena to the non-uniform distribution of the total pressure at the pump interface depends on the amount of water sucked directly from the hull boundary layer and the geometric characteristics of the duct.

Swirl phenomenon (g) appears when the inlet is located in an offset position with respect to the compressor necessitating thereby of an S-shaped duct; it is the result of the interaction between the centrifugal pressure gradient and a low energy region at the duct bends locations [2]. When the swirl persist the flow condition at the leading edge of the rotor blade could be very different from the one considered during the design operation; furthermore, this could contribute to increase the risk of cavitation and cause annoying vibrations. Once again, this could cause malfunctioning of the pump and reduce the waterjet efficiency.

In the design phase attention should be paid since the perturbation of the total pressure distribution at the pump interface is not a characteristic of the inlet by itself; instead it is a consequence of the interaction between intake and pump.

The problems described since here are very common in aeronautical intakes and

for this reason it is possible to find a rich literature on the subject; see [1], [2] and [3] for reference. On the contrary, the literature about these topics in the waterjet field is very poor; one of the few author that studied these problems is Bulten that in [4] wrote:“In the literature relatively little attention has been paid so far to the effects of non-uniform inflow to the waterjet pump. This may be attributed to its close relation to the conventional ship propeller, which also operates in a non-uniform wake field in general. This wake field is determined by the shape of the vessel, so the propulsion system designer has to cope with it”. Anyway, there are at least other three phenomena which are typical of waterjet propulsion which should take into account in the design phase: the deceleration of the flow at the pump location, the cavitation phenomenon and the presence of a drive shaft submerged in the flow field.

Conventional waterjets usually operate in IVR conditions of 1.3 to 1.8 [4], where IVR is defined as in eq. (1.1). This means that the averaged speed of the water at the pump location is smaller than the ship speed and then a diffusion phenomenon have to be taken into account. Betz demonstrated in [5] that when a velocity profile is non-uniform at the entrance of a diffusor the non-uniformity level will increase at the its exit. Therefore if the velocity profile near the inlet entrance is non-uniform, due to the boundary layer or other causes, a high diffusion ratio will make this non-uniformity worse.

Cavitation (f) is the well-known phenomena of formation of vapour bubbles in the water when the static pressure locally reaches the vapour pressure; this phenomenon could cause vibrations, acoustic noise and damages. In waterjet inlets cavitation is usually localised at the lips location; clearly this phenomenon should be avoided.

The presence of the drive shaft in the flow field is an important issue: when the water reaches the drive shaft location several eddies are generated from this submerged part; moreover, if the drive shaft is not protected by a case, the rotating surface of the shaft is in direct contact with the water; this, of course, increases the flow distortion and the losses. Different strategies could be adopted to limit this

phenomenon; the first strategy is to move the shaft location in the rear part of the craft, downline of the pump system, although this could produce problems in the design of the transmission system. The second possibility is the use of a hydrodynamic case to protect the drive shaft; this layout should be well designed because the risk of a bad interaction with the rotor pump is very high. The third strategy is more drastic and consist in a complete abandonment of the drive shaft, using a system capable of driving the propeller from its periphery. One way to do this is the use of an electric Rim Driven Propeller (RDP). In chapter 5 it is explained in detail what is a RDP and what are the benefits of using such device in waterjet propulsion. This option is clearly the most fascinating but several problems should be solved before employing this technology for waterjets since these propulsors are usually high loaded.

In the next figure it is shown a typical total pressure distribution at the inlet/pump interface.

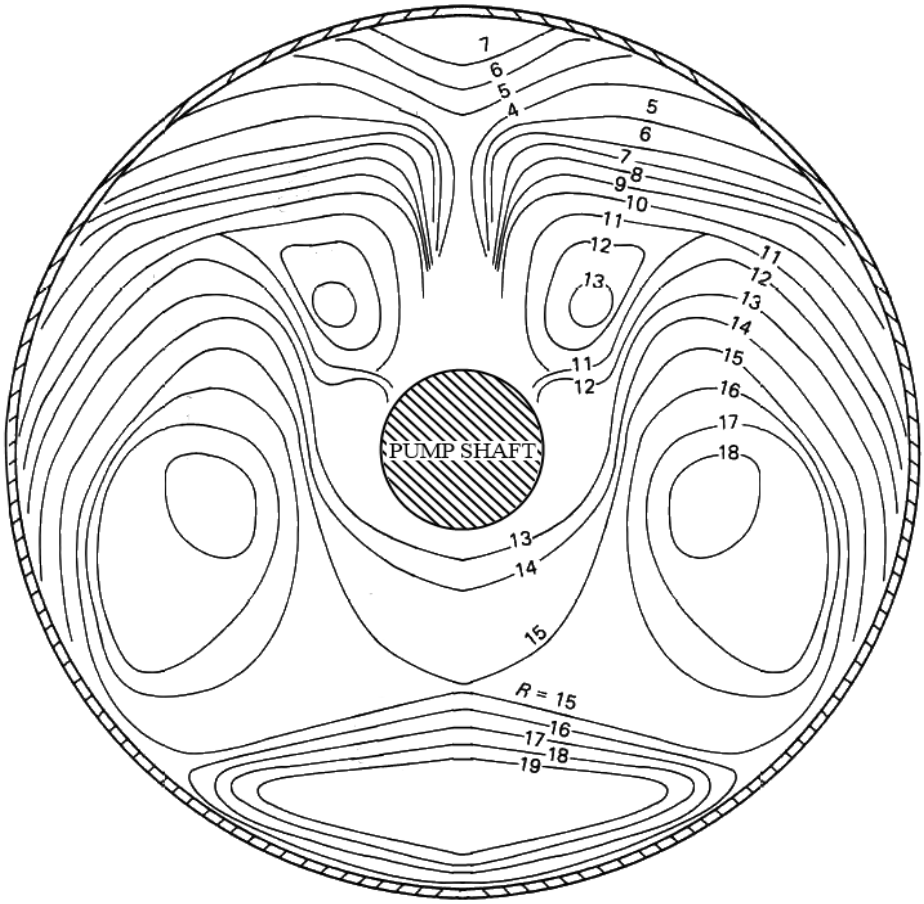

Figure 6: Typical total pressure distribution at the inlet/pump interface. [6]

2.2. Distortion descriptor

A typical total pressure distribution at the pump interface is a complex pattern; it is then very difficult to describe the flow field and even more to understand how this pattern may influence the pump response, without making any simplification that allows to better understand the situation. For this reason, during the past decades, some distortion descriptors have been invented to make this chore easier; these descriptors are widely used in aeronautic applications when a steady state analysis of the flow is sufficient to predict the losses.

The more common distortion descriptors in the aeronautical field are the ones recommended by SAE [7] and the ones used by Rolls-Royce; the procedure entails to divide the pump interface in some rings, usually five, and then divide these rings in different slices. For each slice, as shown in fig. 7, a Pitot probe is used to measure the area averaged pressure and then to know the radial distribution of the pressure.

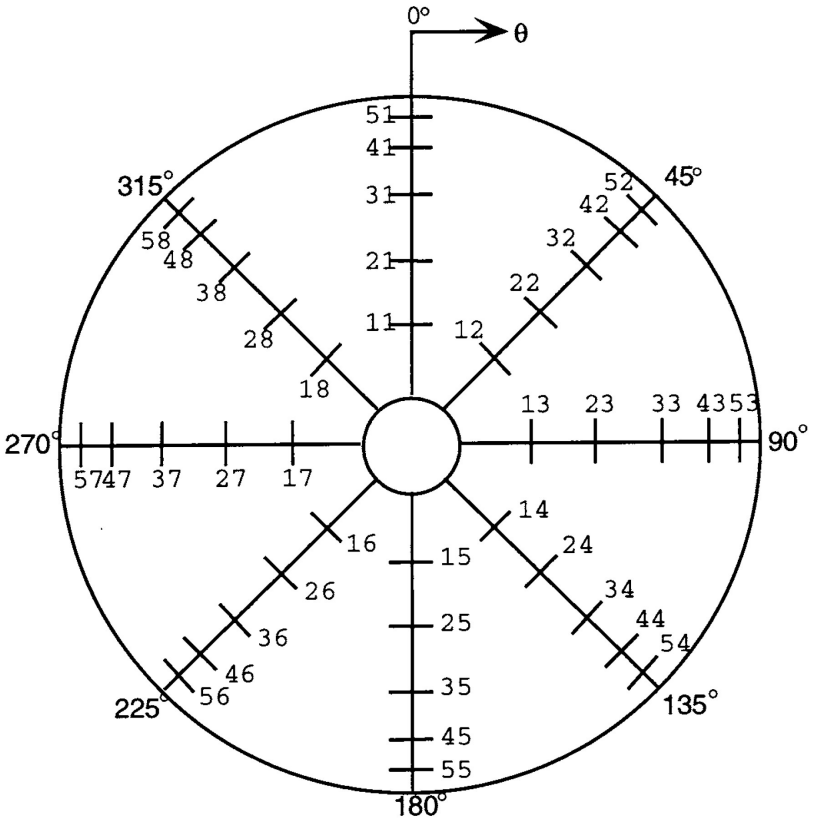

Figure 7: Probe orientation; from [7]

Defining:

- $p_{avg,i}$ as the average total pressure for the ring i on the pump interface;
- $p_{l,avg,i}$ as the average total pressure in the low-pressure region (defined by extent) for the ring i on the pump interface;
- $p_{t,2,avg}$ as the area weighted average total pressure at the pump interface;
- θ_i^- as the circumferential extent in degrees of the low pressure sector width;

it is possible to write the following equations:

$$DPCP_{avg} = \frac{1}{j} \cdot \sum_{i=1}^{j} f(\theta_i^-) \cdot Intensity_i \quad (2.1)$$

$$DPRP_i = g(\theta_i^-) \cdot \frac{p_{t,2,avg} - p_{avg,i}}{p_{t,2,avg}} \quad (2.2)$$

where $Intensity = \frac{p_{avg,i} - p_{l,avg,i}}{p_{avg,i}}$, j is the total number of rings (5 in the SAE recommendations), $f(\theta_i^-)$ and $g(\theta_i^-)$ are extent dependent functions. The low-pressure region is defined as the region where the total pressure value is smaller than the averaged total pressure, ring by ring; see the following figure for a better understanding.

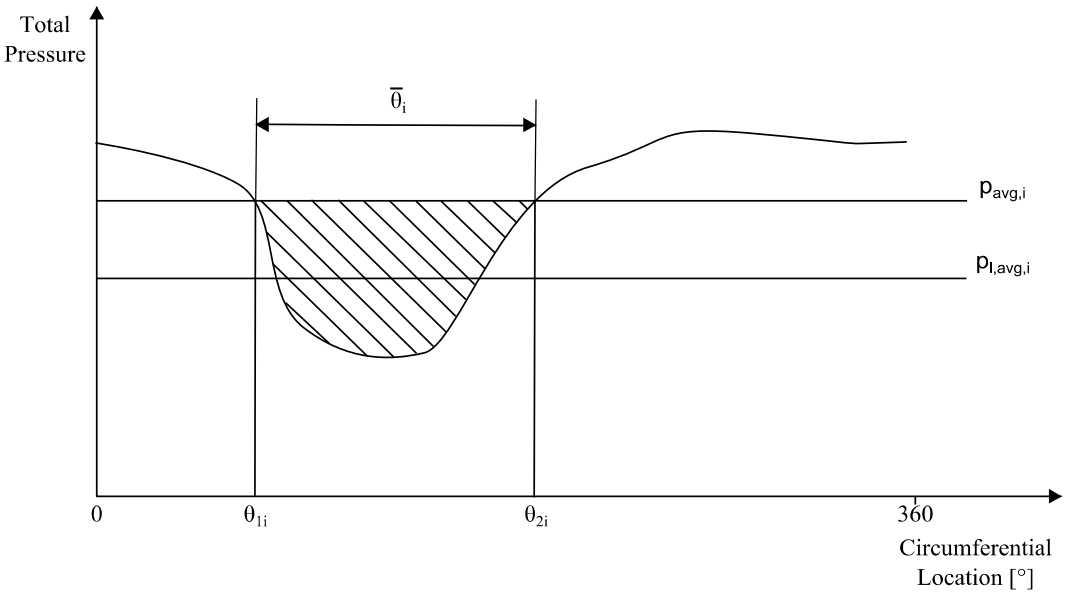

Figure 8: Example of circumferential distribution of the total pressure for a ring

The previous terms are the overall distortion parameters used in the SAE recommendations. They are very useful because once the numerical values of those descriptors for a particular inlet are known, it is easy to predict the losses of the compressor joined with that inlet using simple analytical formulas. For this reason, these parameters are considered an easy way to determine the quality of an intake and could be useful to establish its performance at different conditions of use.

When there is little or no variation of θ_i^- between the rings, θ_i^- could be considered equal to θ^-. For aeronautical compressors with a single-lobed circumferential distortion it has been found that the extent function $f(\theta^-)$ of the $DPCP_{avg}$ may be taken equal to one when $\theta^- \geq \theta_{crit}$ and equal to θ^-/θ_{crit} when $\theta^- < \theta_{crit}$; this happen because the loss of compressor surge line become constant once the extent of the distortion lobe exceed a certain critical value [1].

Based on this consideration Rolls-Royce has develop its own distortion parameter:

$$DC(\theta_{crit}) = DPCP_{avg} \cdot p_{avg,i}/q \tag{2.3}$$

where q is the steady-state dynamic pressure and θ_{crit} is usually considered equal to 60°. Despite Rolls-Royce's parameter has been widely adopted in the aeronautic field, there is no evidence that such parameter could be more suitable for water applications than the SAE distortion parameters.

As told before, in the waterjet field very little attention has been paid to the analysis of the distortion of the flow at the pump interface; for this reason it is not possible to find in literature a correlation between the reduction of performance of waterjet pumps and any kind of distortion parameter; Bulten in [8] defined a way to calculate a distortion parameter for waterjet applications. The coefficient proposed is the following:

$$\zeta = \frac{1}{Q}\int \sqrt{(v - v_{pump})^2}\ dA$$

where Q is the volumetric flow rate, A is the area, v is the local axial velocity and v_{pump} is the average axial velocity.

To this day, there are not experimental tests that may correlate this parameter or the parameters described before with a decreasing of pump performance or that may predict the pump response in their function. As a result, in this work (see the next chapter) it has been arbitrarily decided to adopt the SAE distortion parameter to evaluate the distortion level of the flow incoming into the pump; it was used only as term of reference to compare different kind of inlets, not to try to predict the pump response.

2.3. References

[1] E.L Goldsmith & J. Seddon, **Practical Intake Aerodynamic Design**, Blackwell Scientific Publications, 1993.

[2] J. Seddon & E.L. Goldsmith, **Intake Aerodynamics Second edition**, AIAA Education Series, 1999.

[3] A. Sóbester, **Tradeoffs in Jet Inlet Design: A Historical Perspective**, Journal of Aircraft, Vol. 44, No. 3, 2007.

[4] N. W. H. Bulten, **Numerical Analysis of a Waterjet Propulsion System**, Ph.D. thesis, Eindhoven University of Technology, 2006.

[5] A. Betz, **Introduction to the theory of flow machines**, Pergamon Press, Oxford, 1966

[6] K. Haglund et al., **Design and testing of a high performance waterjet propulsion unit,** Proc. 2Nd Symp. on Small FastWarships and SecurityVessels. Trans RINA, Paper No. 17, 1982.

[7] Anon, **Gas Turbine Engine Inlet Flow Distortion,** Soc. of Automotive Engineers Report ARP-1420, 1978.

[8] N.W.H. Bulten, **Influence of boundary layer ingestion on waterjet performance parameters at high ship speeds**, Proceedings of the 5th international conference on Fast Sea Transportation, pp 883-892, Seattle, 1999.

3. Study and comparison of different inlets

As reported in chapter 1, (see fig. 3) three different types of inlets are known in the waterjet industry: flush, ram and scoop inlet. Flush inlets have the inlet entrance parallel to the water flow and are widely used because they do not suffer from drag due to protruding parts. Ram inlets have the entrance parallel to the water flow and are completely separated from the hull surface (similar to turbofans on commercial airplanes); they are often used in hydrofoil applications because even though the introduction of supports to hold the propulsor increases the overall drag, their particular configuration allows to minimize the air ingestion. Scoop inlets are considered a hybrid form between the previous two and they are rarely used even though there is not a clear explanation for that. The literature is essentially mute about these kind of intakes and the deepest information about scoop inlet can be summarized with the following: “Hybrid forms are not often applied any more. They may be used wherever the disadvantages of flush type intakes are considered too serious, but the drastic ram intake solution is considered overdone” [1]. The most probable reason of not using a scoop inlet is that the protruding duct could cause an additional drag; this is partially true, but the benefit of this choice could overcome the drawbacks. For this reason an investigation using CFD simulations has been carried out with the aim of comparing a conventional flush inlet with a scoop inlet derived from the aeronautical field and therefore finding the pros and cons of these two different inlets.

3.1. Analysis of a conventional flush inlet

In the present paragraph the analysis of a commercial flush inlet is shown; the inlet studied is the intake of a Castoldi turbodrive 340 HC widely described in [2]. This waterjet is a conventional waterjet system with a power input up to 625kW; at 522kW and 23.15m/s it is able to develop a thrust of 13,4kN with a mass flow rate of 885kg/s. This system uses a conventional combustion engine therefore a drive shaft is used with a cover case to minimize the hydraulic losses.

The aim of this chapter is to compare the performance of a flush inlet with the performance of a scoop inlet in terms of hydraulic losses and fluid distortion. It was not the purpose of this thesis to strictly test the Castoldi waterjet in detail, so the hydraulic rotor and stator were omitted and their presence simulated simply imposing an appropriate mass flow rate condition at the exit of the duct. To understand which percentage of the losses was due to the inlet shape and which one was due to the presence of the drive shaft, the inlet was also tested without the presence of the drive shaft case.

3.1.1. Geometry

The shape of the Castoldi inlet is similar to the majority of flush inlets commonly used in the waterjet industry (see fig. 9). A big inlet throat similar to a smoothed trapezoid and parallel to the free stream velocity is located on the hull surface; at the pump interface the duct is perfectly circular. The distance between the two surfaces is not big, to minimize the hindrance of the propulsor, then there is a sudden variation of the internal area. For this specific inlet the throat area was of $0.2078mm^2$ and the pump interface area was $0.0716mm^2$.

Within the duct there is a case which encapsulate the drive shaft to reduce the hydraulic losses. As explained before, a version of this inlet without the shaft case was designed and tested; to keep the pump interface area unchanged, a conical nose cone was used (see fig. 10).

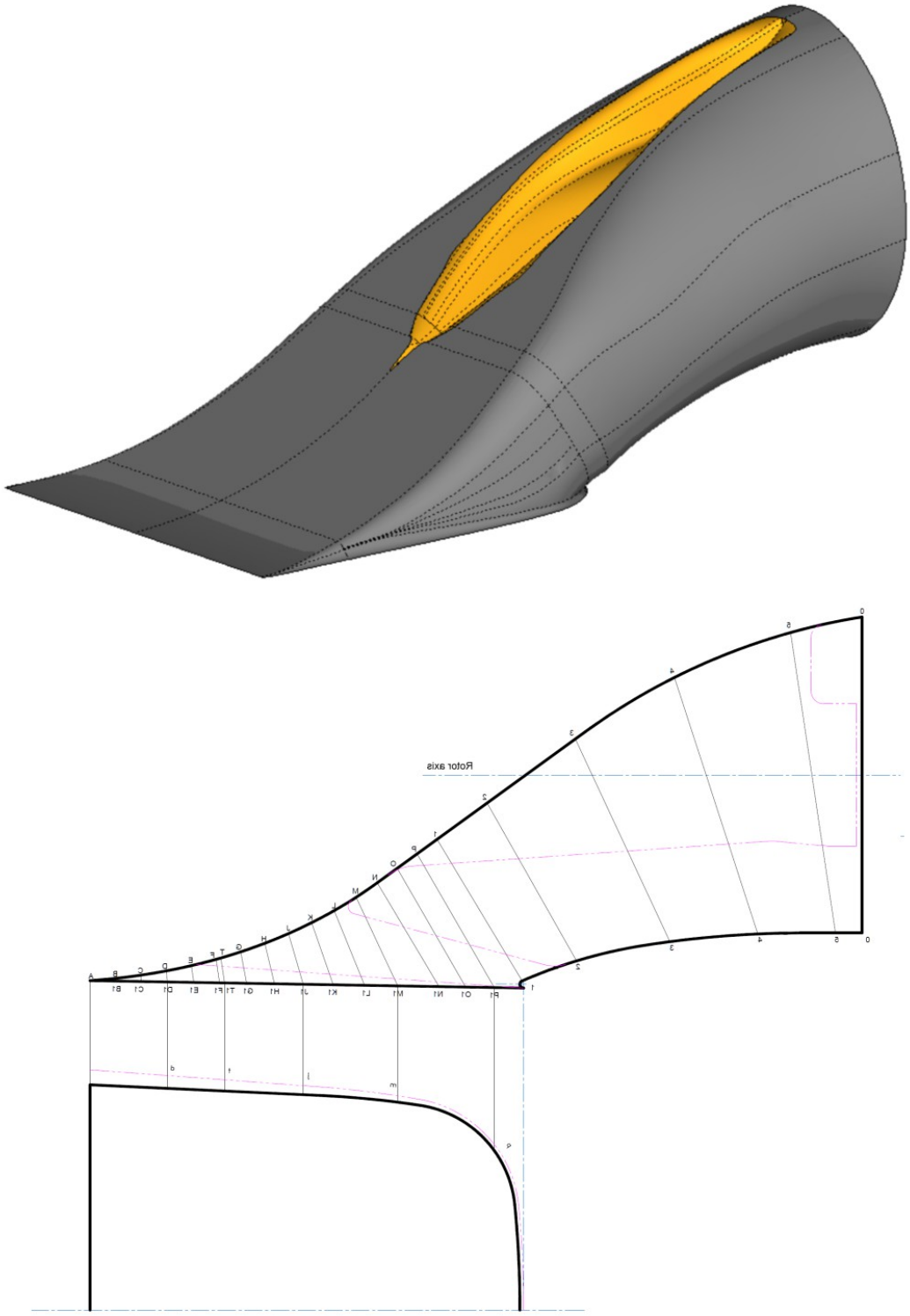

Figure 9: Up a 3D image of the Castoldi TD 340 HC inlet. Down its orthogonal projection; from [2]

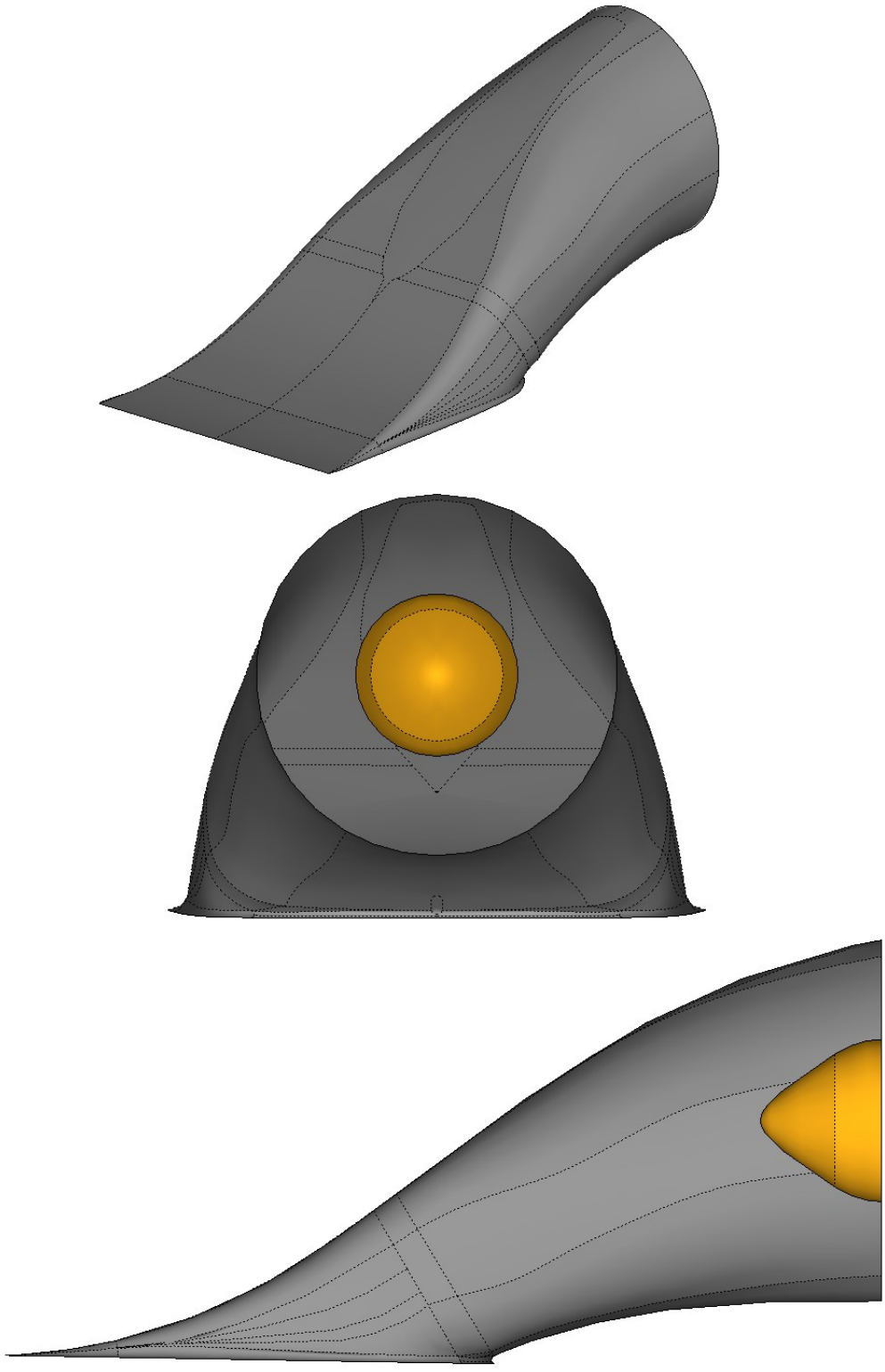

Figure 10: 3D image, rear and right views of the Castoldi TD 340 HC inlet without the drive shaft.

3.1.2. Mesh and simulation setting

Following the guidelines of paragraph 3.2.2 the two inlet geometries were meshed and then numerically tested. The fluid domain contained half of the machine geometry; a symmetry condition was then used on the symmetry plane. An inlet condition with a suitable velocity was applied on the inlet location; the velocity was not constant in order to simulate the velocity distribution in the boundary layer:

$$\frac{v_{inlet}}{v_{\infty}} = \left(\frac{Y}{\delta}\right)^{\frac{1}{n}} \tag{3.1}$$

Where v_{inlet} denoted the local velocity in the boundary layer at a distance Y normal to the wall, v_{∞} the free stream velocity, δ the local boundary layer thickness and n, equal to 6.5, the power law index. This correlation was used as suggested by N. Bulten in [3].

This inlet condition was prescribed to minimize the number of cells without losing the right distribution of the velocity at that location; it was then possible to simulate a hull surface of 4.5m having only 1.5m of space between the inlet location and the inlet lip. This solution gave good results in the test case in

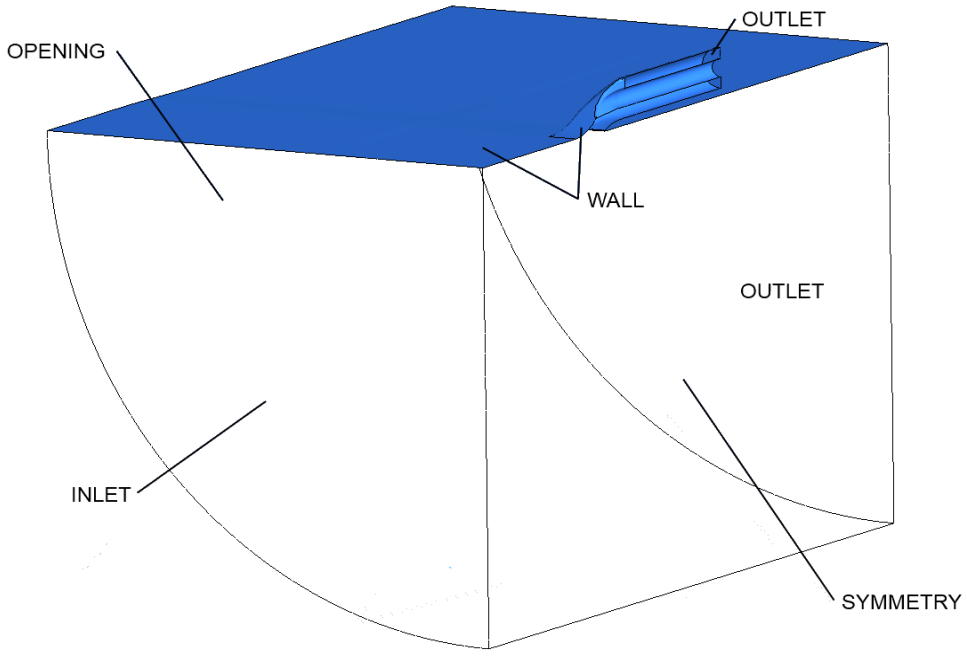

Figure 11: Fluid domain of CFD mesh

paragraph 3.2 for which experimental data were available.

An opening condition and an outlet condition with a relative static pressure equal to zero were used at their respective locations (see fig. 11). An outlet condition was imposed at the duct outlet location specifying the mass flow rate. A wall condition with no slip option was used at the hull and duct location.

The domain was a portion of a cylinder with a radius of 4m; the distance between the inlet location and the outlet location was 6.5m.

For each geometry (with drive shaft case and without it) 5 tests were done at different free stream velocities and different mass flow rates. The test conditions are summarized in the next table.

Case	1	2	3	4	5
V_∞ [m/s]	5	10	15	20	25
ṁ **[kg/s]**	300	500	700	800	1000

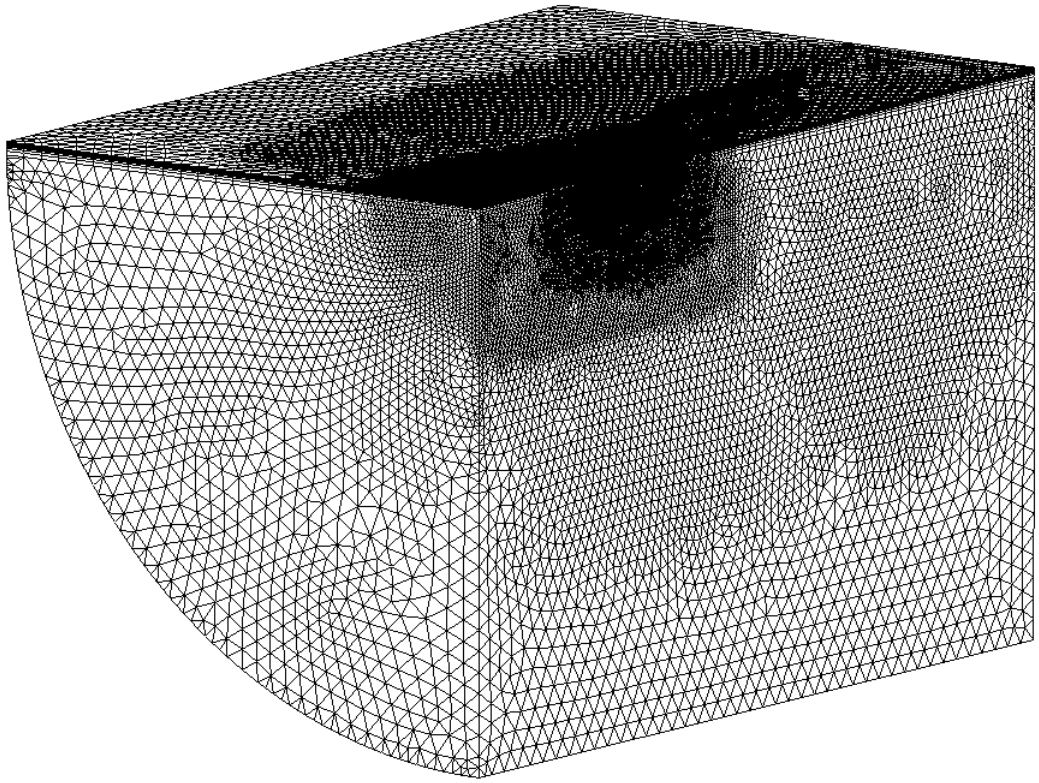

Figure 12: Details of the global mesh.

For each geometry the mesh employed was a tetrahedral mesh with a number of elements around to 4.2 millions. A boundary layer with 15 prismatic layers was used on the wall locations. The minimum dimension of the surface triangles was 0.005m; the maximum one was 0.15m at the inlet, outlet and opening locations. The expansion ratio of the tetrahedral mesh was 1.1. The expansion factor of the prismatic mesh was 1.2; the height of the first layer was 0.28mm that led to a y+ between 30 and 300. A k-ω SST turbulence model and an isotherm condition were used.

A mesh sensitivity analysis was done to verify that this mesh allowed to get trustworthy results; to made that the complete configuration of a Castoldi turbodrive 340 HC waterjet was tested in a steady-state CFD analysis, deducting the pump and nozzle geometries from the details reported in [2]. The results obtained during the analysis were compared with the experimental test results of the Castoldi waterjet, using as terms of reference the mechanical power consumption and the global thrust. The procedure adopted to made these simulations is not reported in this document because this would go beyond the purpose of the Ph.D. thesis and it could distract the reader from the original goal, that is to compare a generic flush inlet with a scoop inlet. However, the thrust and hydraulic power, calculated with the CFD analysis which employed the mesh above described, are reported in the next table where they are directly compared with the experimental Castoldi results.

	CFD	**Experimental**	**Error**
Thrust [kN]	13.19	13.41	-1.64
Mech. Power [kW]	553.38	522.20	+5.97

As it is possible to see, the error in the estimation of the reference quantities were acceptable; no considerable improvements were achievable further increasing the mesh density.

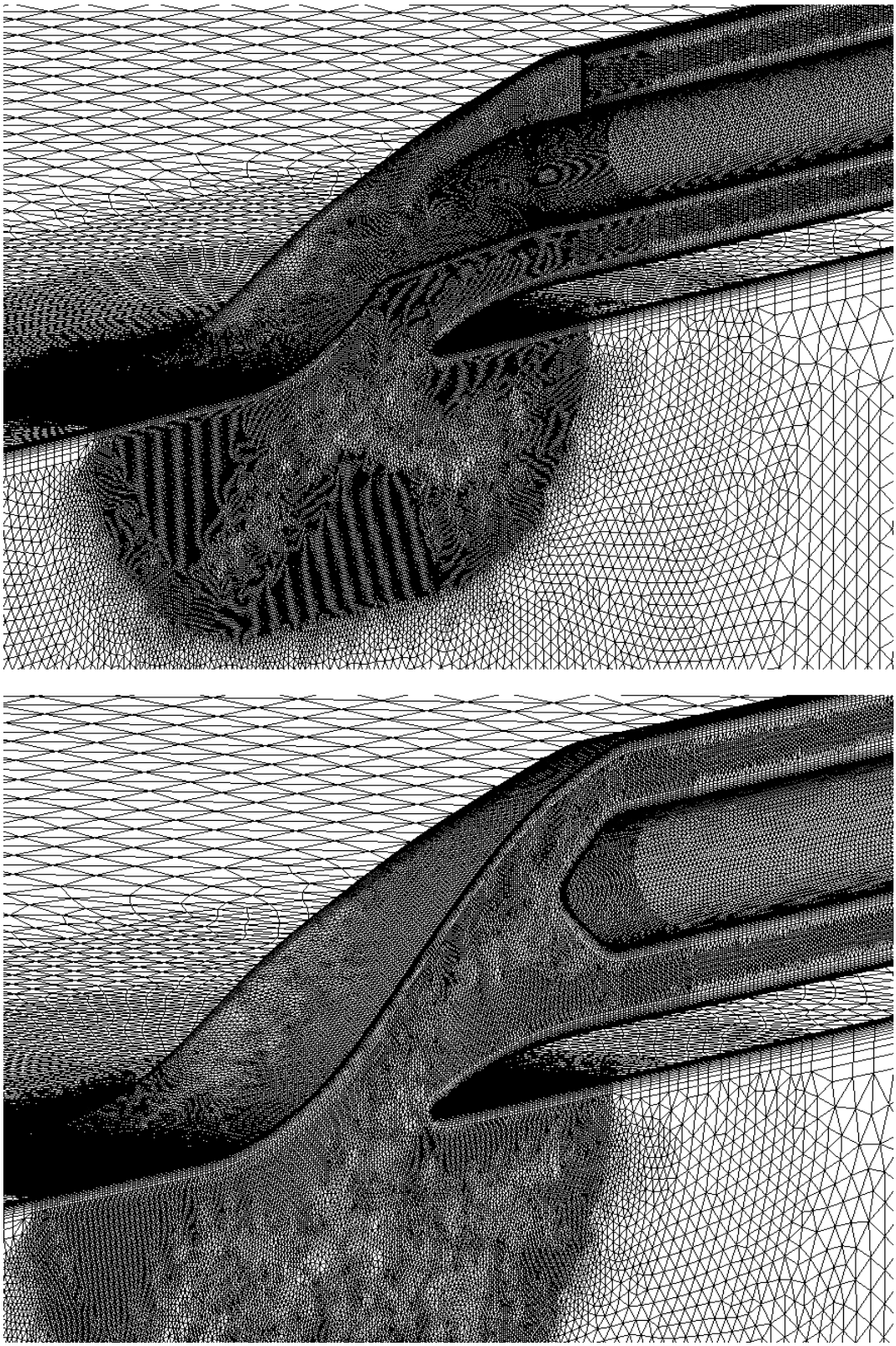

Figure 13: Details at the inlet location of the mesh with the drive shaft case (up) and without it (down).

3.1.3. CFD results

From the analysis of the numerical simulations interesting information about the flow field could be understood. As previously explained in chapter 2, the pump interface is of utmost importance because a distorted pattern in the fluid distribution may lead to a remarkable decreasing in the performance of the pump system; thereby, the pump interface was taken as survey station on which the performance of the inlets, for all the tested conditions, were compared. In particular, two parameters were adopted for comparison:

- the ratio between the area averaged total pressure at the pump interface and the total pressure at the free stream location: $\frac{p_{t,2,avg}}{p_{t,\infty}}$
- the $DCPC_{avg}$, with $f(\theta_i^-)$ equal to one and j equal to 5: $DPCP_{avg} = \sum_{i=1}^{5} \frac{Intensity_i}{5}$ from (2.1)

Although the results were known in detail for every node of the mesh grid the data were treated as if they were experimental and the recommendations of the SAE international association were followed; in particular, at the pump interface forty virtual probes were placed, each of which characterized by its own area, and from each probe the weighted-area relative total pressure was extracted.

For all calculations, the results of the numerical simulation were considered acceptable when the maximum residue were lower than 10-4.

In figure 14 and 15 it is possible to see the distribution of the normalized total pressure for the flush inlet with the drive shaft case and without it. The simulations did not take into account the presence of both the pump system and the grid rake, which usually protect the inlet from ingestion of dangerous rubble; for this reason these analysis were not reflective of the flow distribution in the real waterjet system; anyway, despite these simplifications, the considerations which could be inferred from these simulations are still of general validity, and they are worth doing to compare different inlet geometries and to gain insight on those problems that could reduce the efficiency of the system.

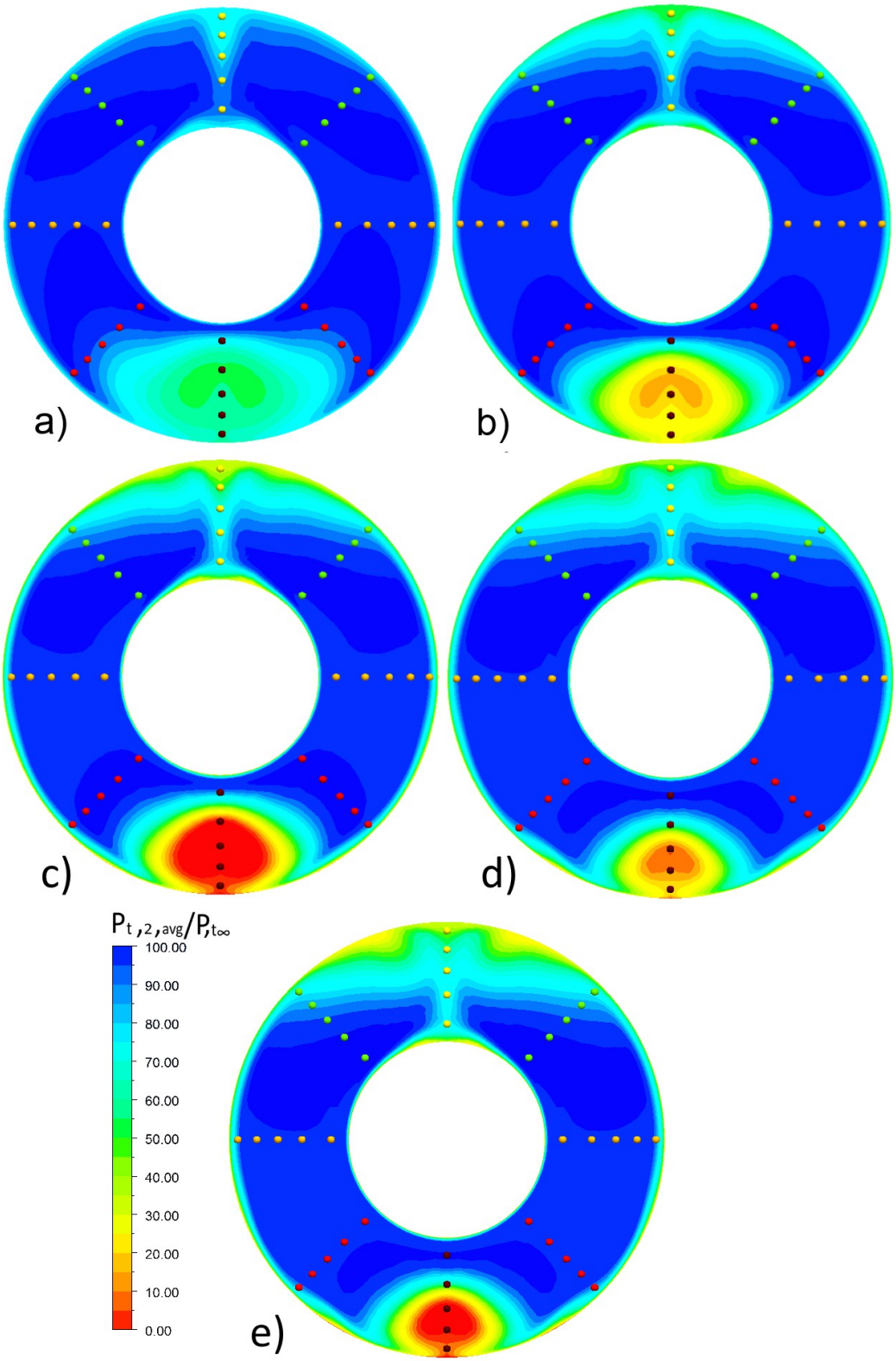

Figure 14: $p_{t,2} / p_{t,\infty}$ *of the inlet with the drive shaft case; from 5m/s to 25m/s respectively from a) to e)*

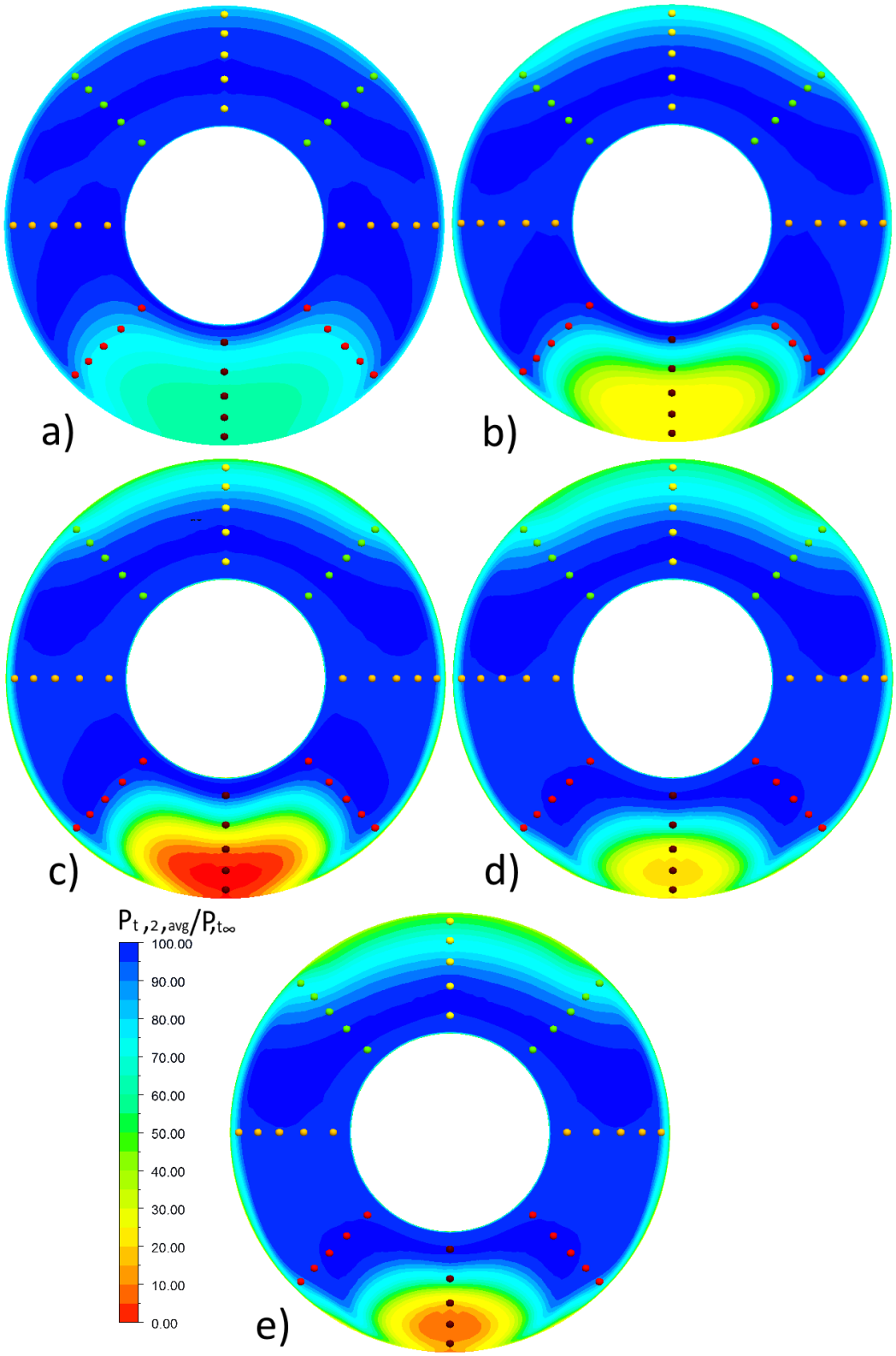

Figure 15: $p_{t,2}/p_{t,\infty}$ *of the inlet without the drive shaft case; from 5m/s to 25m/s respectively from a) to e)*

Looking at the images it is clear how the Castoldi inlet, and flush inlets in general, may lead to important hydraulic losses and flow distortions. The red zones show that, for some conditions, it was possible to locally reach the cavitation point due to secondary flows and eddies. In all the cases, for both inlets configurations, it was possible to see the consequences of the boundary layer profile distension on the lower part of the duct; this phenomenon is more evident looking at the total pressure distribution at the symmetry location in figure 16. It is also possible to see the flow separation phenomenon; the red zone represents the region where the axial velocity is equal to zero so it could be imagined as the limit of the separation eddy. As explained in chapter 2, the problem of flow separation is well known in the waterjet industry and even when a flush inlet is well designed, this phenomenon could appear at speeds far from the cruise speed, when the mass flow rate is too high for that condition, or when the incidence angle of the flow is too big; this condition, for example, is typical of the starting condition.

In the next table a direct comparison between the original Castoldi flush waterjet and the one without the drive shaft is reported. It is important to underline that even though the flush inlet was a Castoldi intake, there is no reason to believe that inlets from other companies perform a lot better than the Castoldi's one, since companies are accustomed to take inspiration from geometries of their own competitors. Therefore, these results and the related conclusions should be considered generally applicable.

		Cruise speed [m/s]				
		5	**10**	**15**	**20**	**25**
Flush inlet with drive shaft	$\frac{p_{t,2,avg}}{p_{t,\infty}}$ **[%]**	91.68	86.59	82.56	85.33	83.60
	$DPCP_{avg}$	0.219	0.415	0.563	0.421	0.488
Flush inlet without drive shaft	$\frac{p_{t,2,avg}}{p_{t,\infty}}$ **[%]**	91.11	88.61	86.92	87.91	86.45
	$DPCP_{avg}$	0.190	0.406	0.492	0.333	0.385

The $DPCP_{avg}$ shows an important fluid distortion on the pump interface in both cases; the reason was explained before and lies on the boundary layer profile distension at the lower duct location; there are no data in literature that correlate the $DPCP_{avg}$ distortion parameter with the losses to which it may lead to the pump system. In the next future a hard work should be undertaken to better understand this aspect; anyway, there is a big chance that a value as big as the one observed could lead to important losses in the pump system.

The percentage of absolute total pressure loss for the original Castoldi inlet varied from 8.32% in best case to 17.54% in the worst case. The same inlet without the case shaft had the losses between 8.89% and 13.55%; so the presence of the drive shaft is responsible for 2-3% of the total pressure decreasing at the cruise speed, that is for the Castoldi inlet 23.15m/s. In any case the efficiency of the waterjet inlet seems not particularly good if compared with ordinary aeronautical inlets that usually have total pressure losses lower than 5% [4]. The main reason of this, as easily understandable, is the fact that is very difficult to keep the water flow attached to the duct walls and prevent the boundary layer profile distension when the water ingestion is performed perpendicularly to the speed vector.

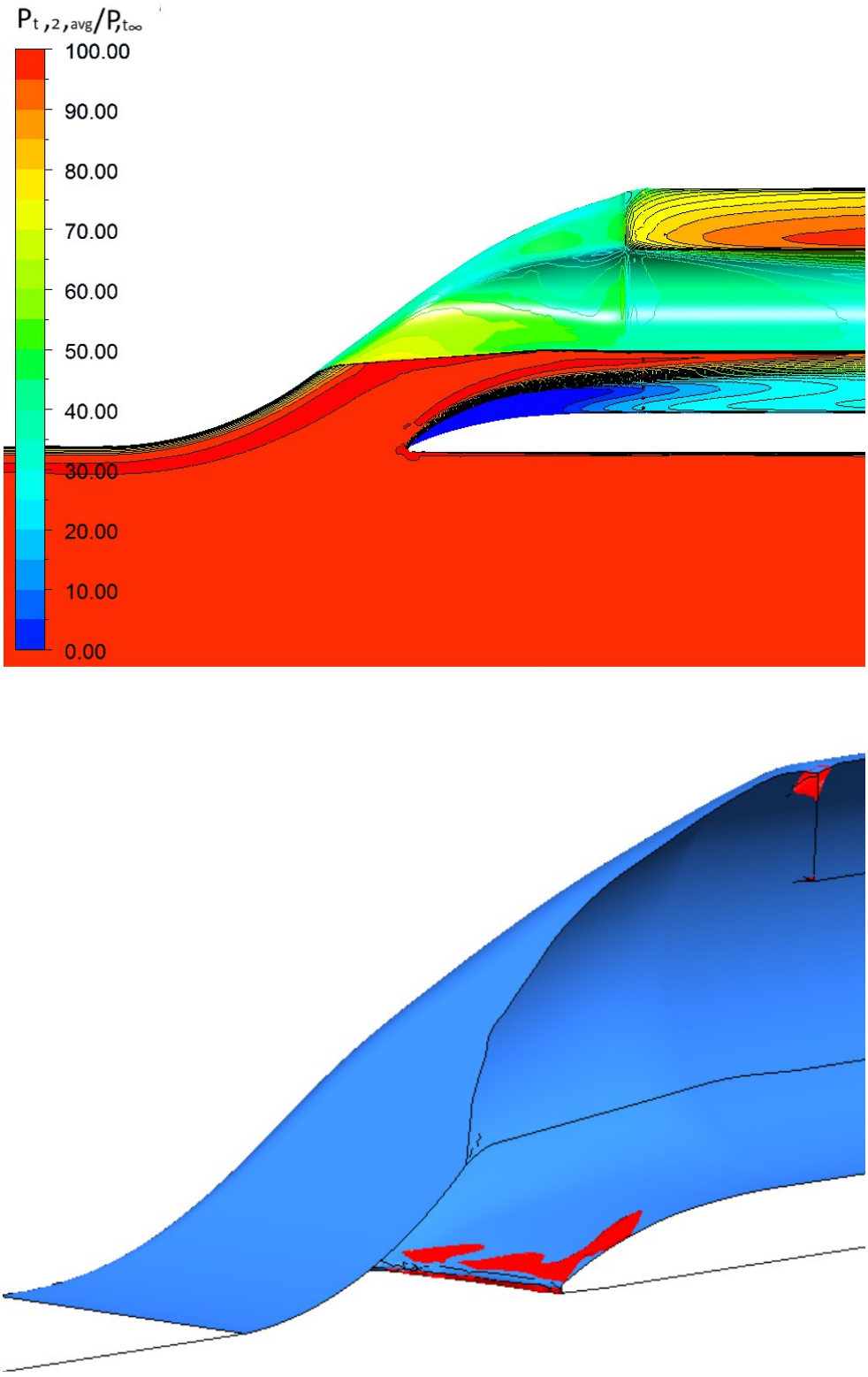

Figure 16: Up the total pressure distribution at symmetry and duct location for the waterjet with the drive shaft at 20m/s. Down, in red, the evidence of flow separation.

3.2. NASA BLI inlet

Due to the absence of literature about scoop inlets in the naval field, a research in the aeronautical field was done with interesting results. Among all different types of aeronautical intakes, it was found a class of inlets with several similarities with waterjet scoop inlets. These intakes are called Boundary Layer Ingesting (BLI) inlets and are expressly designed to work with a thick boundary layer and an S-shape duct.

The use of S-shape duct is not novel in the aeronautical field; several examples of these kind of intake can be found in military and commercial airplanes as the Boeing 727 and the Lockheed L-1011. These intakes are integrated in the forward portion of the fuselage so the thickness of the boundary layer is not significant. On the contrary BLI inlets are integrated in the backward portion of the fuselage so the thickness of the boundary layer is significant and may reach the 30 percent of the inlet height [5]. The benefit of this choice is that the ingestion of the boundary layer and the consequent energization of the aircraft wake may allow to decrease the power consumption; the reason of this is easily understandable looking at fig. 17 where there is a comparison between a conventional pod inlet and a BLI inlet, which is able to ideally ingest all the boundary layer. Called F the force needed to the engine to compensate the drag, $P_{no\ BLI}$ the power consumption with the pod inlet and P_{BLI} the power consumption with the BLI inlet:

$$F = \dot{m}\left(u_\infty - u_w\right) \tag{3.1}$$

$$P_{no\,BLI} = \frac{\dot{m}}{2}\left(u_j^2 - u_\infty^2\right) = \frac{F}{2}\left(u_j + u_\infty\right) \tag{3.2}$$

$$P_{BLI} = \frac{\dot{m}}{2}\left(u_\infty^2 - u_w^2\right) = \frac{F}{2}\left(u_w + u_\infty\right) \tag{3.3}$$

Since uj>uw the power consumption using a BLI inlet is lower.

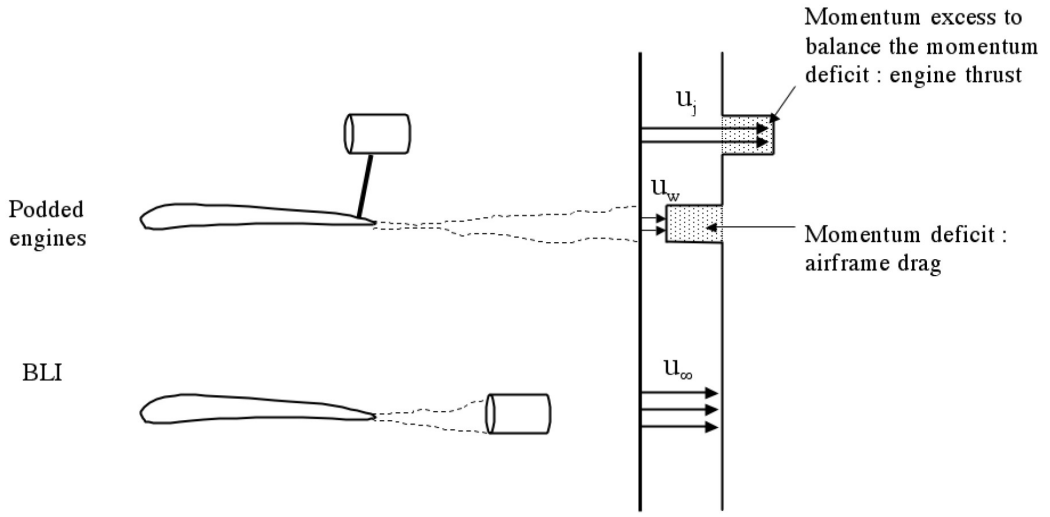

Figure 17: Energization of aircraft wake using a BLI inlet. From [6]

In a real case the BLI inlet is not able to ingest all the boundary layer but there is still a significant benefit in using this kind of inlet; systems studied for blended wing body airplanes (BWB) have shown significant reductions in fuel consumption, from 0 to 16%; see [6] and [7] for reference. This is not, of course, a "free lunch" and there are two big problems which should be taken into account before using this particular configuration to avoid other problems that may compensate or overcome this benefit. The first is the complexity of the external inlet aerodynamics which consists of a combination of a degraded boundary layer, shocks at transonic speed and an adverse pressure gradient due to inlet blockage [8]; fortunately these problems are less important in high speed water application. The second problem is the non uniform total pressure distribution on the engine interface; this problem is described in chapter 2 and must be considered carefully in waterjet applications.

In the following paragraphs the CFD analysis of a BLI inlet developed by NASA in collaboration with Boeing is presented; this intake, deeply described in [5], works with a boundary layer thickness that is about 30 percent of the inlet height, it is S-shaped and it can work with a Reynolds number of the same order of magnitude of the one of conventional waterjets. The geometry of the intake and the data information acquired during the CFD simulations and the sensitivity analysis were used as starting point for the design and the simulation of the scoop

inlet for the waterjet system described in paragraph 3.3. Due to the impossibility of realising an experimental test campaign of the waterjet inlet in this phase of the work, the analysis of the NASA BLI inlet was conducted with particular attention.

3.2.1. Geometry

The BLI inlet analysed in the following paragraphs was the one described in the "High Reynolds Number Investigation of a Flush-Mounted, S-Duct Inlet With Large Amounts of Boundary Layer Ingestion" [5] and there denoted as "inlet A". This inlet had a nearly semicircular throat aperture and a circular interface at the compressor plane. The sections between the throat and the AIP (Aerodynamic Interface Plane) were composed of various couples of semi-superellipses (top and bottom for each couple). A superellipse is defined as $|x|^e+|z|^e=1$; that particular shape was used to increase the passage area of the duct without sudden variations with the aim of reducing the secondary flows importance. The diameter of the aerodynamic interface plane was 0,062m (2.448in) and the ratio between the AIP area and the inlet throat area was 1.070; the distance between the inlet throat and the AIP was 0,196m (7.697in); the height of inlet throat was 0,043m (1.703in) and the captured area was 0.0037m^2 (5.760 in^2).

The inlet lip geometry had a ratio between the length and height equal to two; the external shape of the duct had no other function than reducing the drag. The expected Reynolds numbers, based on aerodynamic interface plane diameter, were in the range 5.1 million up to 13.9 million at cruise speed from 0.25 Ma to 0.85 Ma.

The next figure shows the geometry details of the inlet.

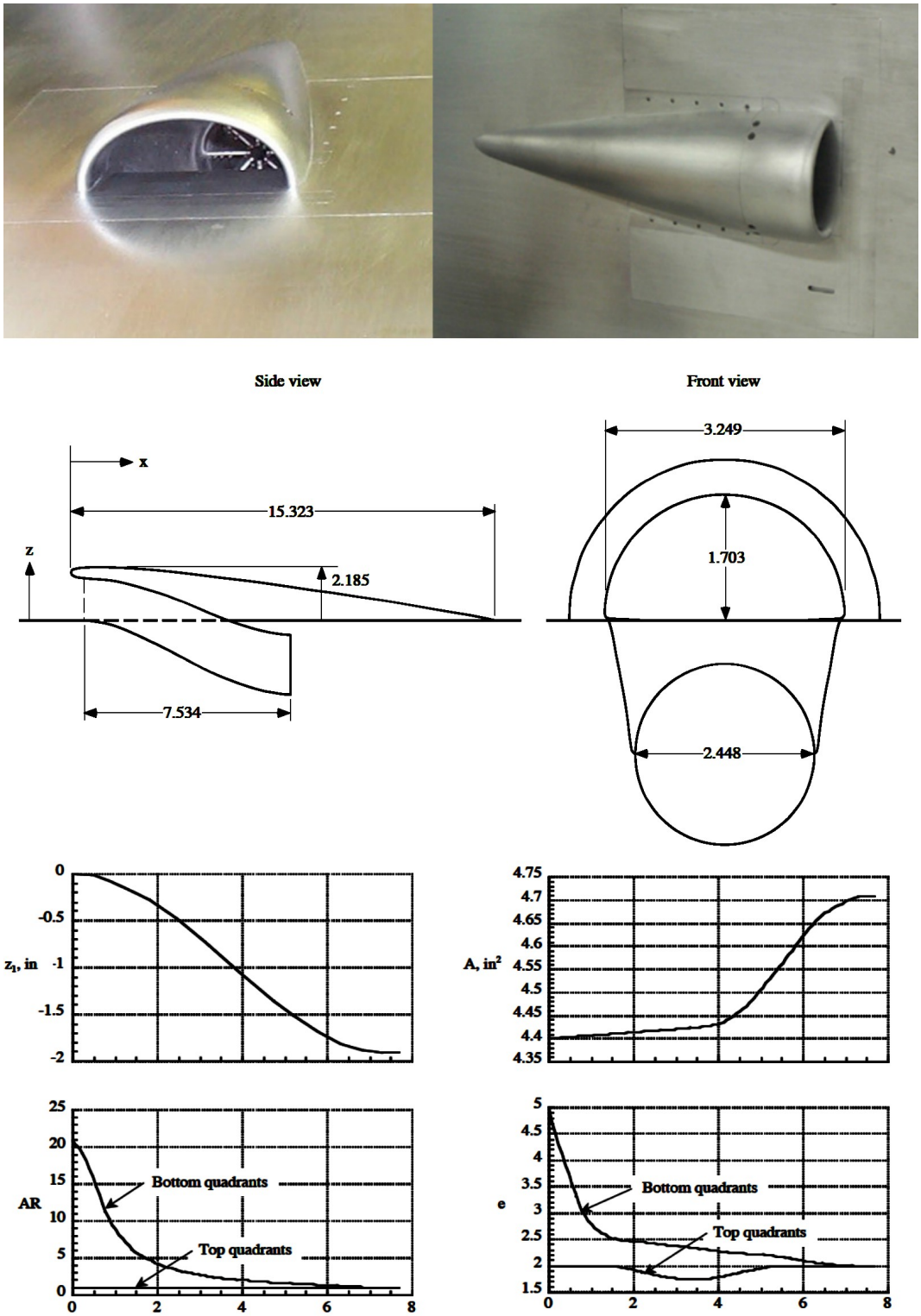

Figure 18: NASA BLI inlet A. Details of geometry. Side and front views not to same scale. Dimension in inches. From [5]

3.2.2. CFD analysis and mesh sensitivity

Due to the fact that this BLI inlet was used, with slight changes, as scoop inlet of a waterjet system (paragraph 3.3) and that there were no information about CFD analysis of scoop waterjet inlets in the literature, the CFD analysis and the mesh sensitivity study were carried with particular attention using the NASA experimental results as comparison.

The mesh sensitivity study required numerous tests and simulations that are summarized in the following:

- three grid refinement levels were tested: the first mesh with 1.5 millions of cells, the second with 3 millions of cells and the third with 6 millions of cells; all grids featured a hybrid layout, i.e., prismatic layers near walls and tetrahedral elements for the rest of the computational domain; in particular, the prismatic layer was composed by either 24 prismatic boundary layers or 18 prismatic boundary layers. The free stream velocity was uniform at the inlet location and an isothermal condition was prescribed. The calculation results were not in good agreement with NASA experiments, regardless the number of prismatic layers, which indeed seems to not introduce appreciable differences in the numeric solution;
- the same meshes used in the previous test were used only with a change: the isotherm condition was changed with a total energy condition. The results were more similar to NASA ones: total pressure distribution at the AIP was comparable to the one in NASA results, but the same could not be said with regard to the $DPCP_{avg}$ (average circumferential distortion descriptor) even though an improvement was observable with the increasing of cells density;
- after a reduction of the virtual wind tunnel length, the uniform velocity condition at the inlet location was changed with a velocity profile described by a power law (n=8.3) to take in account the boundary layer velocity distribution at the hull surface [9]. Improvements in accuracy were found both in the total pressure distribution and the $DPCP_{avg}$ at the

AIP. Different tests were done with 12, 15, 18 and even 41 prismatic boundary layers and different cell densities.

For all mesh sensitivity tests a k-ω SST turbulence model with y+ between 30 and 150 at walls was used. At the end of this mesh sensitivity analysis the configuration that gave best results was the mesh with more than 5 millions of cells, with 15 prismatic boundary layers and with a power law velocity profile (n=8.3) as inlet boundary condition to describe the boundary layer velocity distribution.

Figure 19 shows the mesh domain used in the simulation; the boundary conditions were imposed as follow: the free stream velocity was imposed to be equal to 46,63m/s (1835,97in/s), the atmospheric pressure was 4.320E05Pa (62.655psi) and the mass flow rate imposed on the exit area of the duct was 1.447kg/s (3.190lb/s).

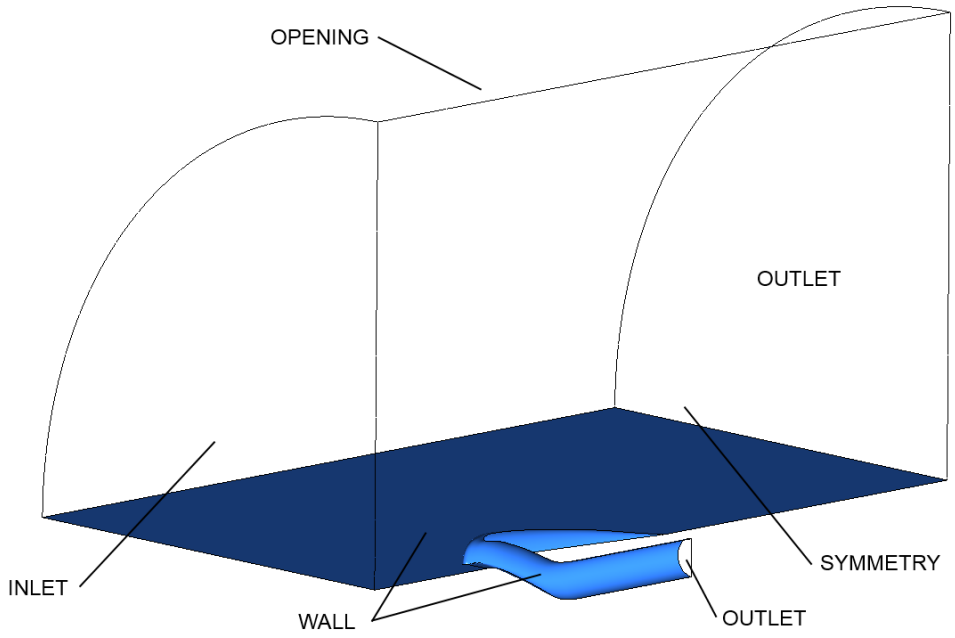

Figure 19: Fluid domain of CFD analysis

In the next figure it is possible to see the mesh density on the main surfaces.

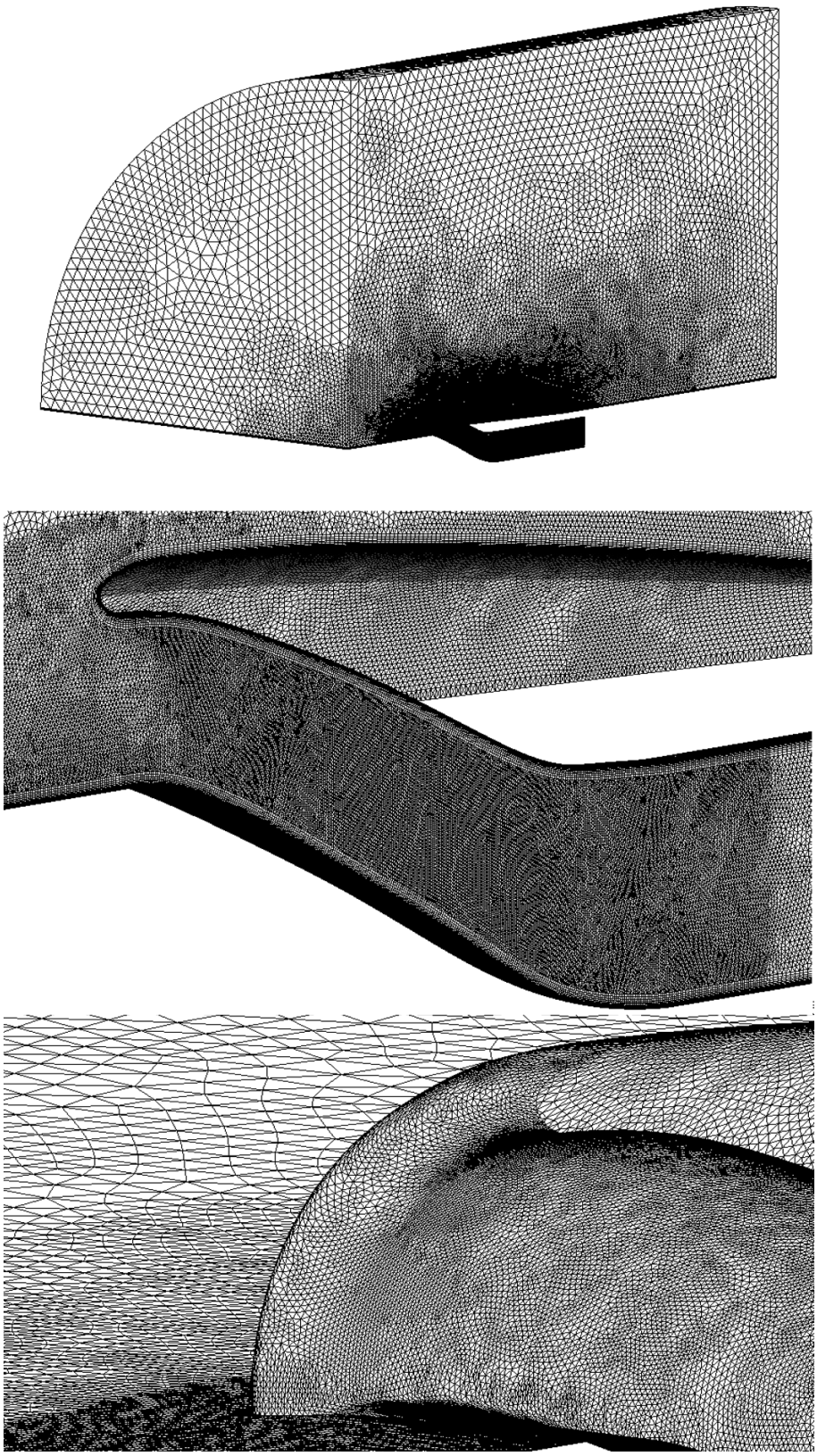

Figure 20: Details of different mesh surfaces

3.2.3. CFD results

The examination of the results on particular zones of interest showed a good prediction of the flow distribution using the test condition described in the above paragraph. The flow pattern calculated in this document was not everywhere equal to the one predicted in the NASA paper (see fig 20-21); in particular on the AIP secondary flows of modest extent seemed to be present while they were not predicted in NASA results. The flow pattern on the duct entrance and on the duct lip was concordant. As for averaged quantities, there were no appreciable differences between the two simulations, therefore the small differences in the flow pattern could be related to the different software used to perform the calculations (i.e., in this document was used CFX while in the NASA paper was used OVERFLOW; see [10] and [11] for reference) and to the fact that the geometry was reproduced using the data contained in [5] and then slight changes from the original geometry could be involuntarily made.

The CFD results obtained by the author agreed with NASA results with a deviation of 0.10% for the total pressure distribution and 0.83% for the $DPCP_{avg,}$ at the AIP; these discrepancies were considered acceptable.

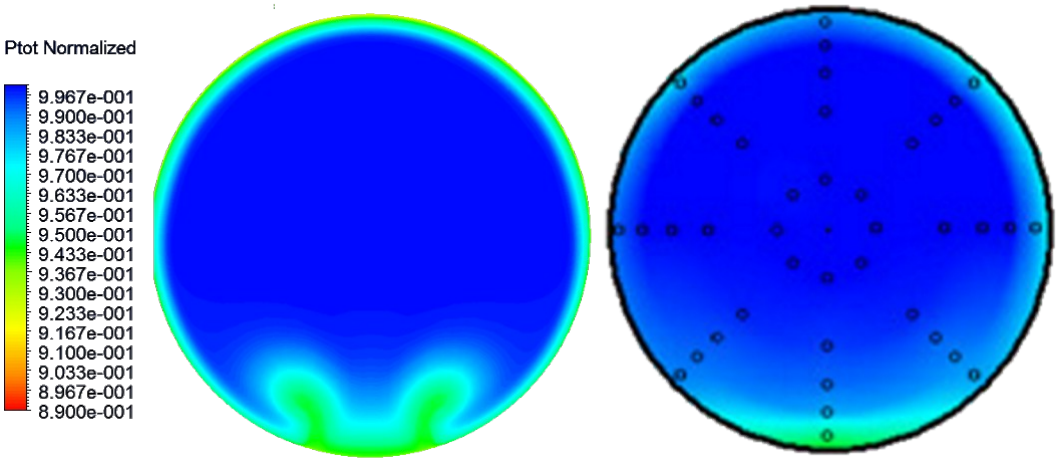

Figure 21: Total pressure distribution on the AIP; on the left the one calculated by the author, on the right the one calculated by NASA [5]

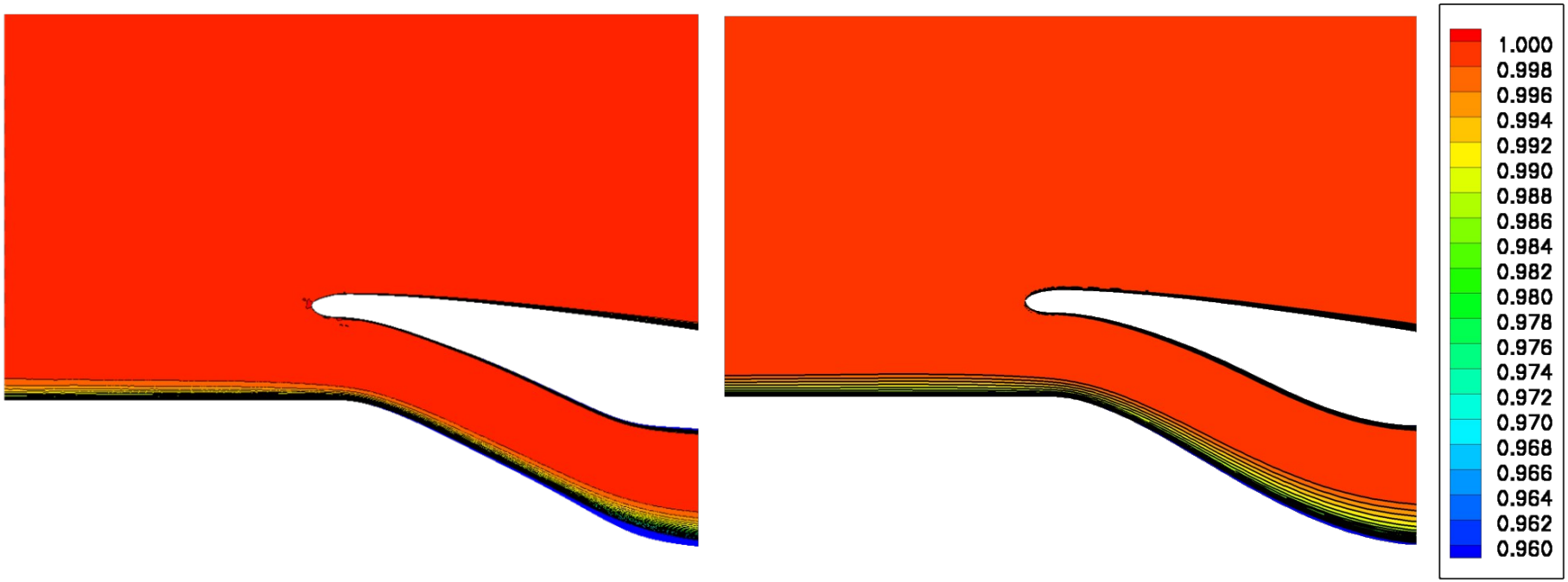

Figure 22: Total pressure distribution on the symmetry plane; on the left the one calculated by the author, on the right the one calculated by NASA [5]

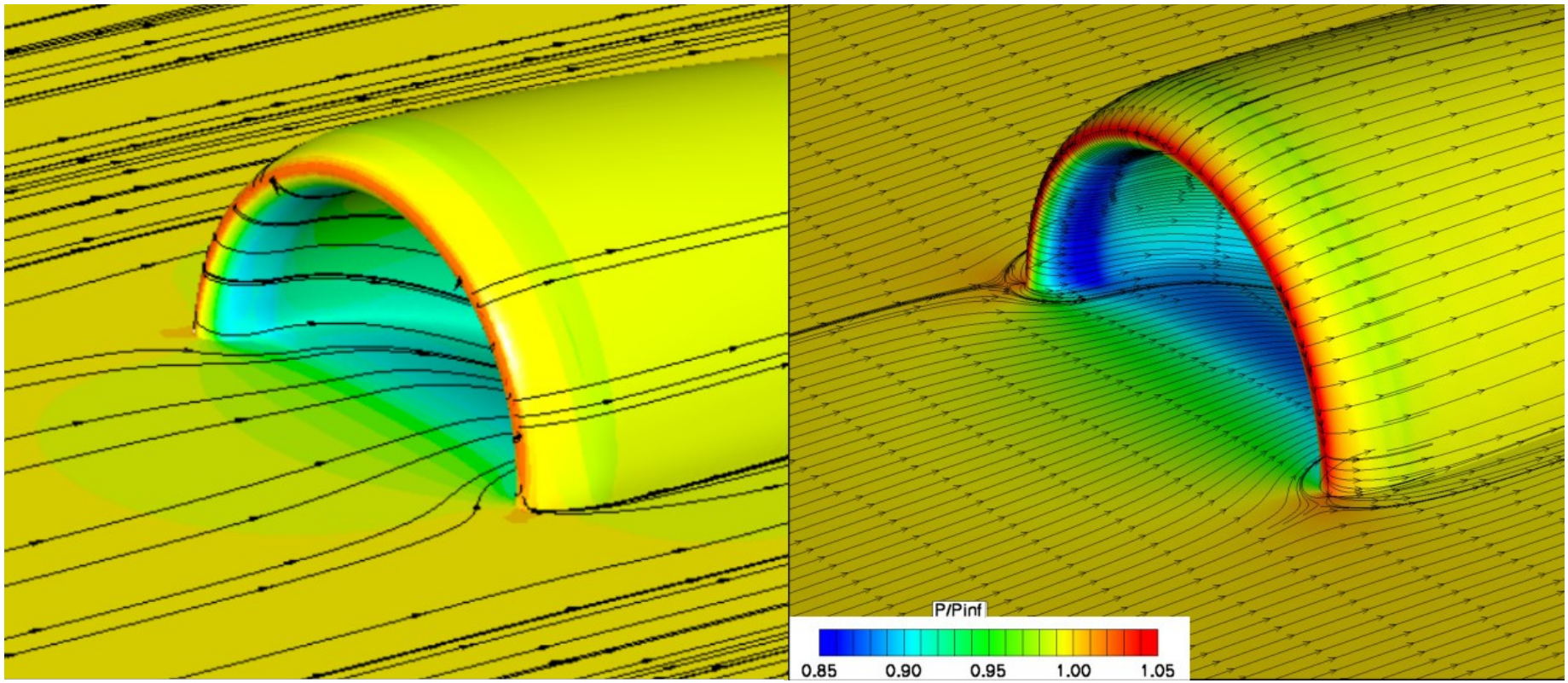

Figure 23: Figure 13: Static pressure distribution on the duct; on the left the one calculated by the author, on the right the one calculated by NASA [5]

3.3. Inlet S-X02

With the aim to discover performance of a non conventional inlet for a waterjet system, a scoop inlet derived from the aeronautical field was developed and tested numerically. As disclosed in the previous paragraph, this inlet derived from an experimental BLI inlet; it had a nearly semicircular throat aperture and a circular interface at the compressor plane. The sections between the inlet throat and the AIP were studied to minimize secondary flows.

The main objective of the analysis was the comparison of this scoop inlet with a conventional flush inlet with the aim of finding the differences of these two inlets in terms of the total pressure loss and the distortion descriptor $DPCP_{avg}$. As it was done in the previous paragraphs, the hydraulic rotor and stator were omitted and their presence simulated simply imposing an appropriate mass flow rate condition at the exit of the duct. To understand which percentage of the losses was due to inlet shape and which one was due to the presence of the drive shaft, the inlet was also tested without the presence of the drive shaft case.

3.3.1. Geometry

The shape of the inlet S-X02 was similar to the NASA BLI inlet described in the previous paragraph. The inlet throat is nearly semicircular and protruding from the hull surface; at the pump interface the duct is perfectly circular. The sections between the throat and the AIP are composed by two different semi-superellipses (top and bottom). The inlet throat area was $0.0716m^2$; the external diameter of the pump interface was 0.338m, while the internal one was 0.152m; The pump interface had exactly the same dimensions of the pump interface of the Castoldi TD 340 HC (paragraph 3.1). The distance between the inlet throat and the AIP was 1m. The height of the rotor axis with respect to the hull surface was 0.215m, the same of the Castoldi inlet. As described earlier, two versions of this inlet were tested, the first with the drive shaft case and the second without it. The shape of the case was similar to the one used in the Castoldi inlet.

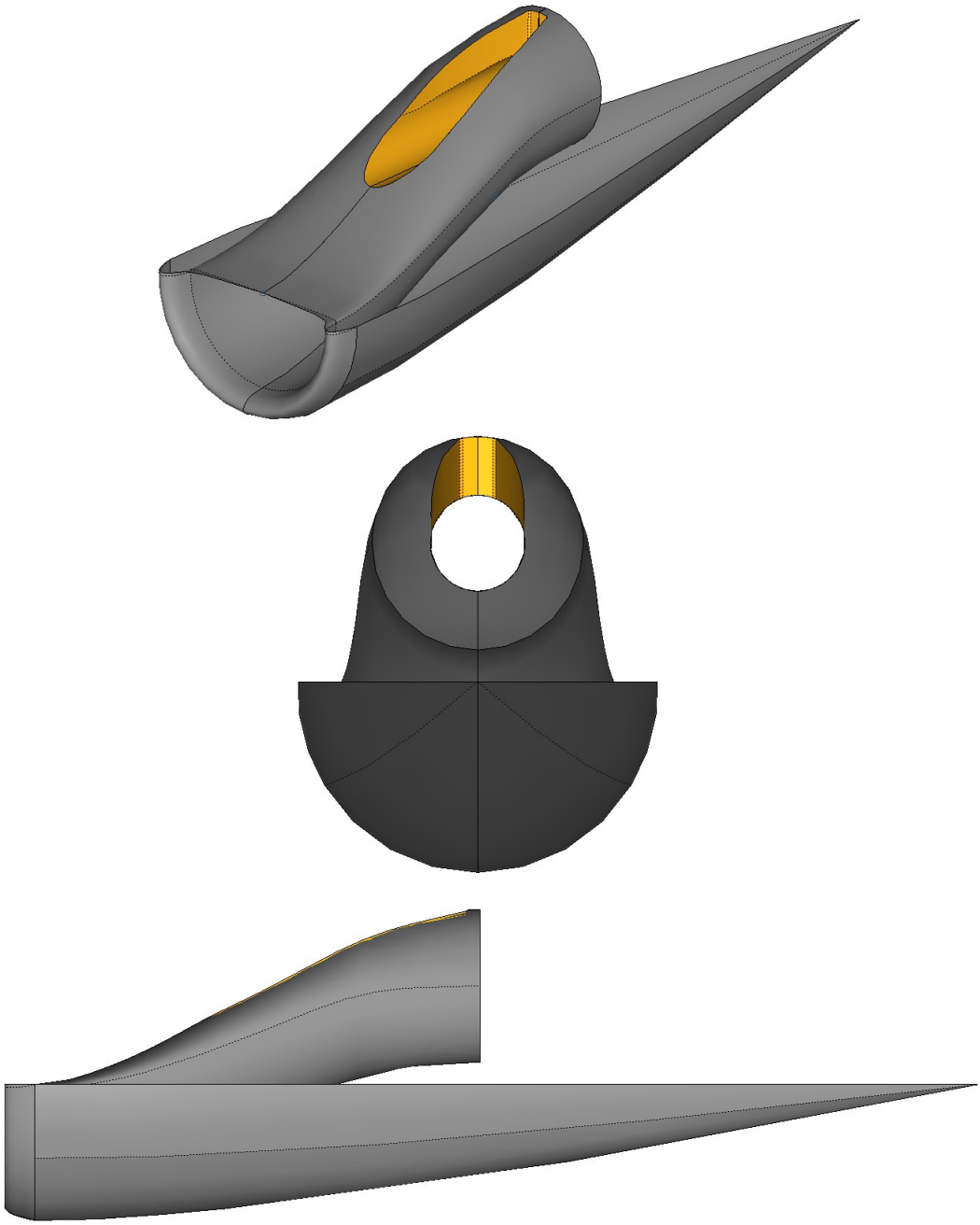

Figure 24: 3D image, rear and right views of the S-X02 inlet with the drive shaft.

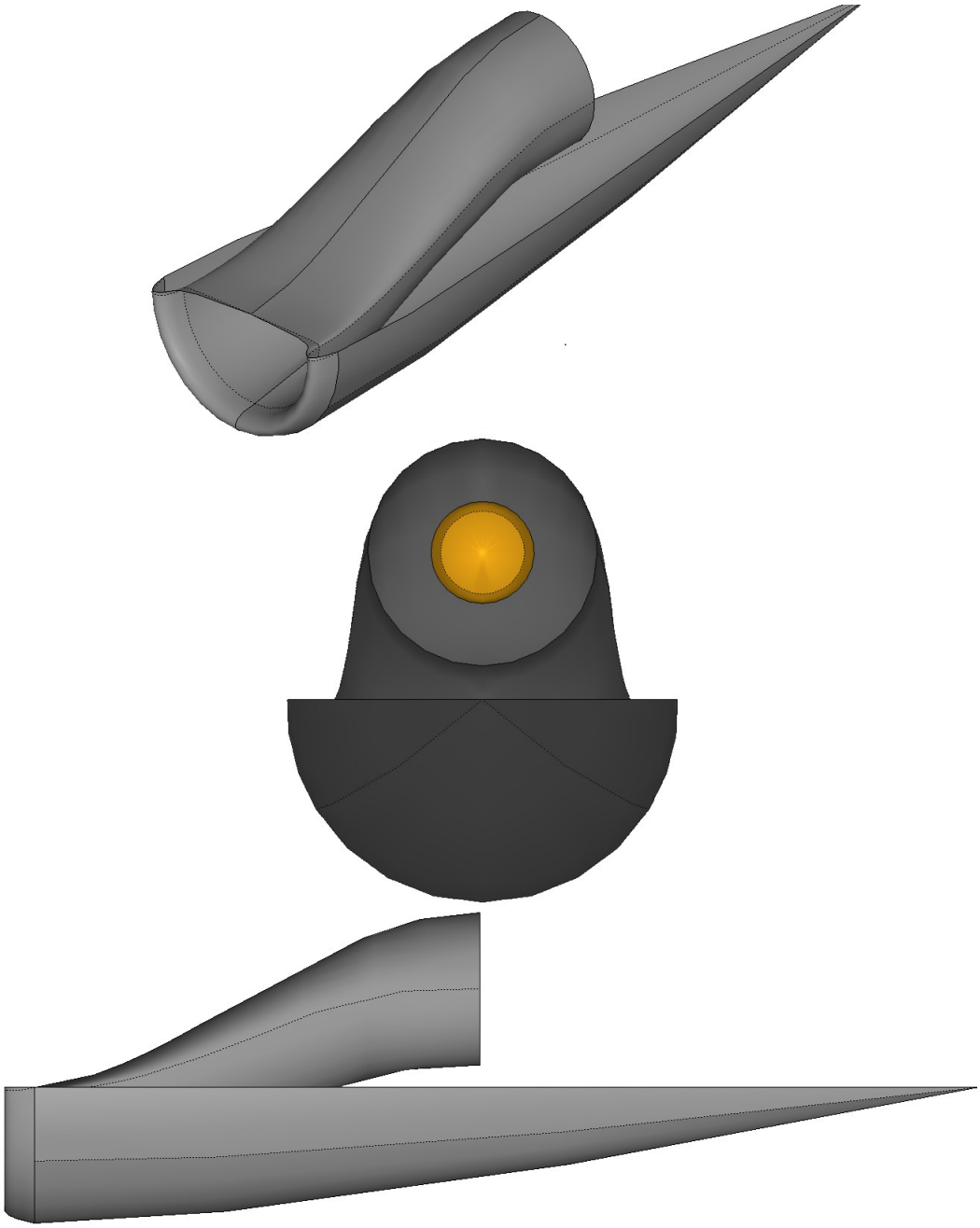

Figure 25: 3D image, rear and right views of the S-X02 inlet without the drive shaft.

3.3.2. Mesh and simulation setting

Following the guidelines of paragraph 3.2.2, the two inlet geometries were meshed and then numerically tested. The fluid domain contained half of the machine geometry; a symmetry condition was then used on the symmetry plane. An inlet condition with a fixed inlet velocity was applied on the inlet location. The velocity profile was not constant, in order to simulate the velocity distribution in the boundary layer; a power law with n equal to 6.5 was used. This configuration was chosen to minimize the number of cells in the mesh without losing the correct distribution at that location; it was then possible to simulate a hull surface of 4.5m having only 1.5m of space between the inlet location and the inlet lip. This solution gave good results in the case test in paragraph 3.2. An opening condition and an outlet condition with a relative static pressure equal to zero were used at their respective locations (see fig. 26). An outlet condition was imposed at the duct outlet location specifying the mass flow rate. A wall condition with no slip option was used at the hull and duct location. The domain was a portion of a cylinder of radius 4m; the distance between the inlet location and the outlet location was 6.5m.

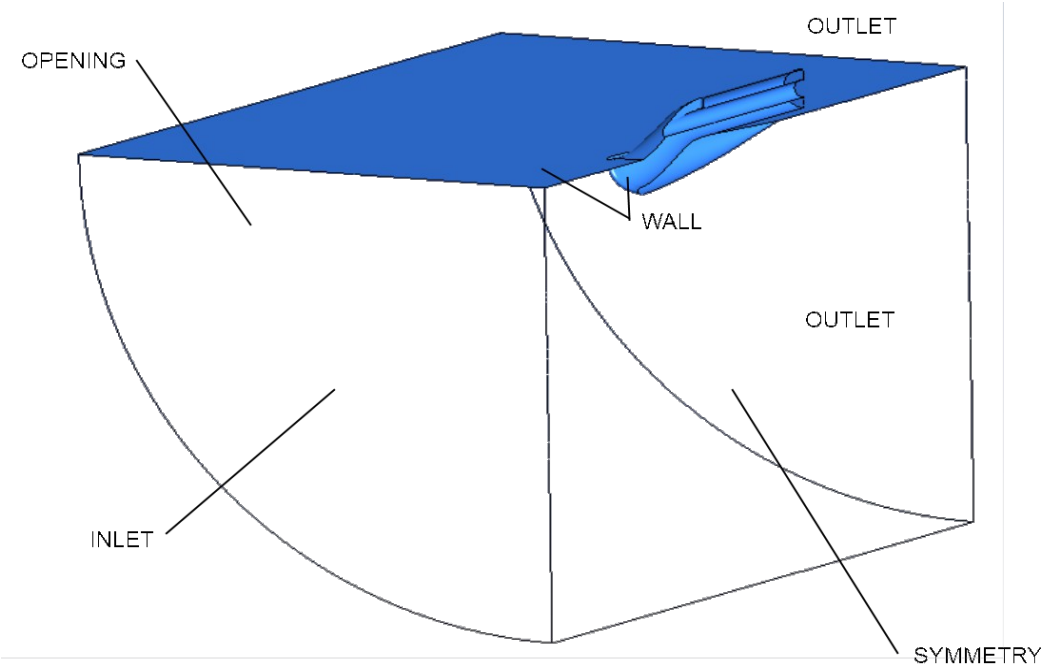

Figure 26: Fluid domain of CFD analysis

For each geometry (with drive shaft case and without) 5 tests were done at different free stream velocity and different mass flow rates. The different test condition are summarized in the next table.

Case	1	2	3	4	5
V_∞ [m/s]	5	10	15	20	25
ṁ **[kg/s]**	300	600	700	800	1000

For each geometry the mesh was a tetrahedral mesh with a number of element near to 8.5 millions. A boundary layer with 15 prismatic boundary layers was used on the wall locations. The number of elements of this mesh was twice the number of elements of the flush inlet mesh just because of the external part of the duct: the guidelines of the design of this mesh were the same of the ones used for the flush inlet. The minimum dimension of the surface triangles were 0.005m; the maximum one was 0.15m at the inlet, outlet and opening locations. The expansion ratio of the tetrahedral mesh was 1.1. The expansion factor of the prismatic mesh was 1.2; the height of the first layer was 0.28mm that led to a y+ between 30 and 300. A k-ω SST turbulence model and an isothermal condition were used.

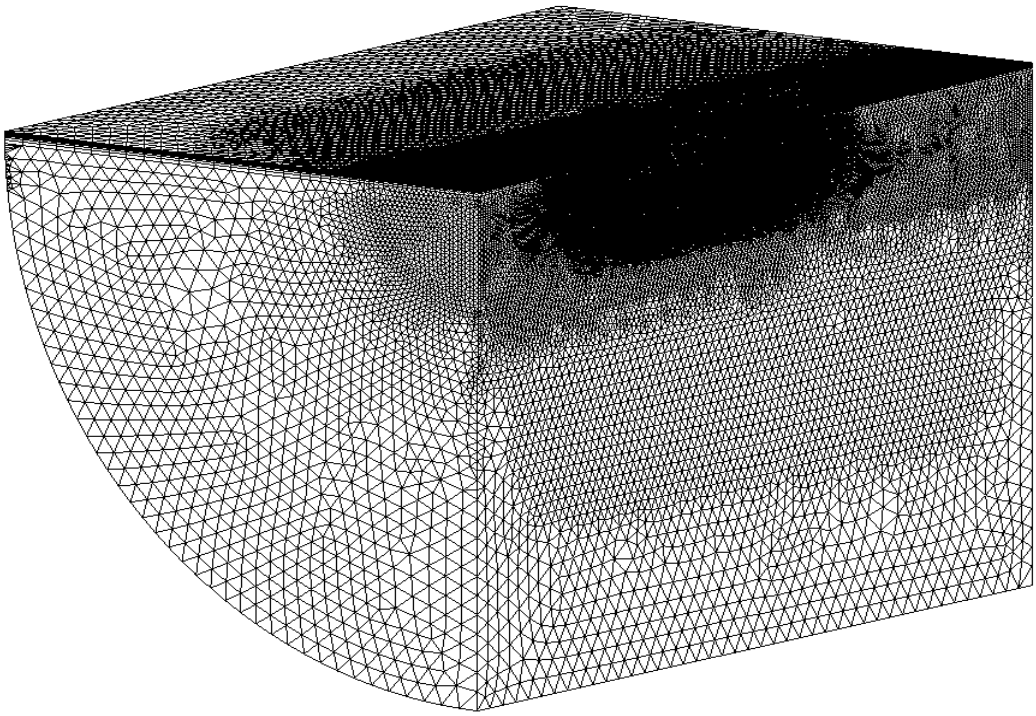

Figure 27: Details of the global mesh.

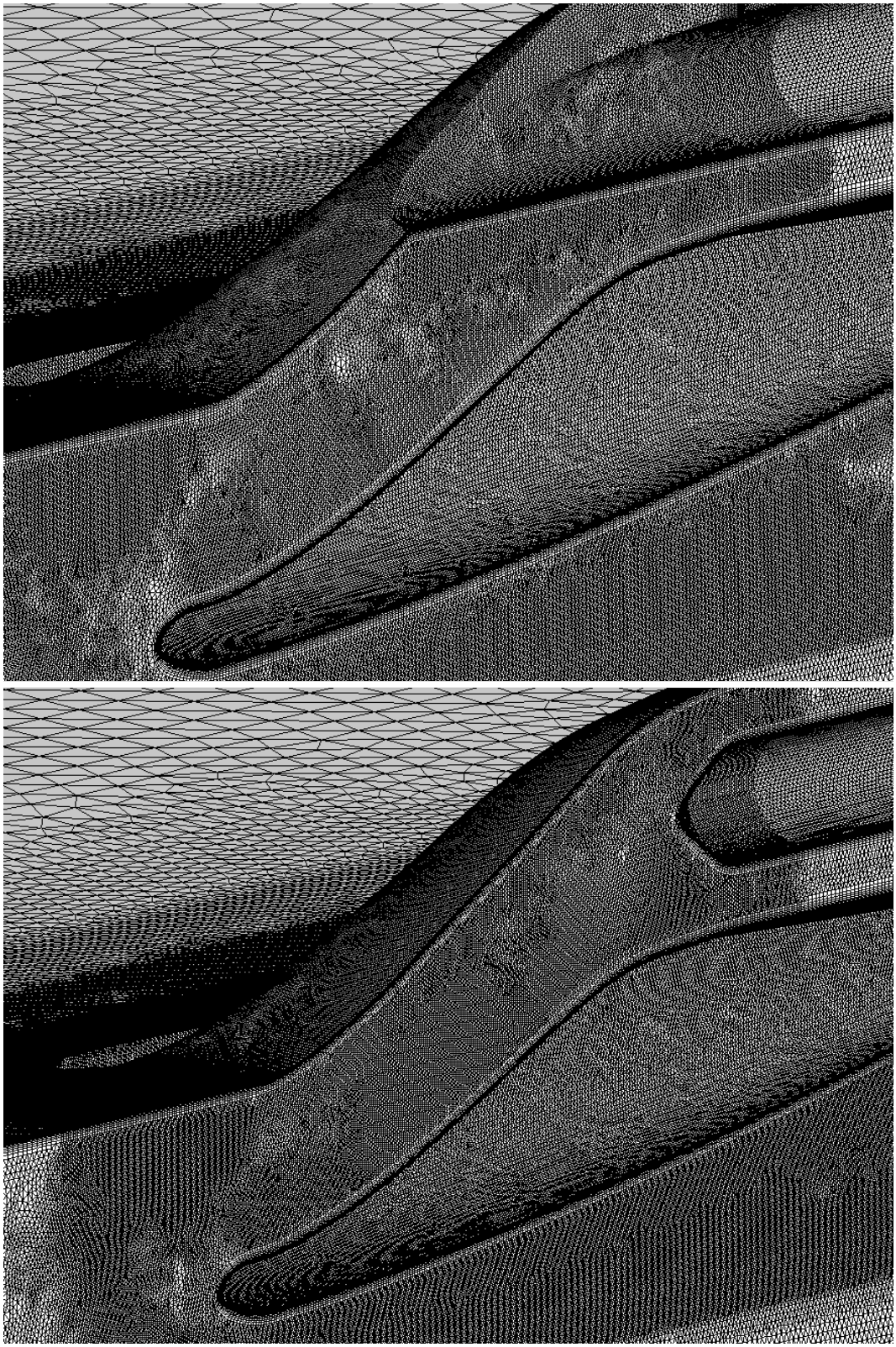

Figure 28: Details at the inlet location of the mesh with the drive shaft case (up) and without (down).

3.3.3. CFD results

From the analysis of the numerical simulations interesting information about the flow field can be understood. As previously explained in chapter 2 and paragraph 3.1.3, a particular area of interest was the pump interface because a remarkably distorted pattern in the fluid distribution leads to a decrease in the performance of the pump system; the pump interface was then the zone chosen to understand the inlet performance at the different conditions tested.

The two parameters used as criterion of comparisons were:

$$\frac{p_{t,2,avg}}{p_{t,\infty}} \quad \text{and} \quad DPCP_{avg} = \sum_{i=1}^{5} \frac{Intensity_i}{5} \quad \text{from (2.1)}$$

Even if the results were known in detail for every node of the mesh grid, the data were treated as if they were experimental and the recommendations of the SAE international association were followed.

The results of the numerical simulation were considered acceptable when the maximum residuals were lower than 10^{-4}.

In figure 28 and 29 the distribution of the normalized total pressure for the flush inlet with the drive shaft case and without it is pictured. The interface area was the same for both cases as well as the main geometrical quantities, which were all exactly the same of the Castoldi's one. The simulations did not take into account the presence of the pump system and of the grid rake, that usually protect the inlet from the ingestion of dangerous rubble, and then these analyses were not reflective of the flow distribution in the real waterjet system; anyway the considerations which could be extracted from these are still useful to predict possible problems that could reduce the efficiency of the system and to compare different inlet geometries.

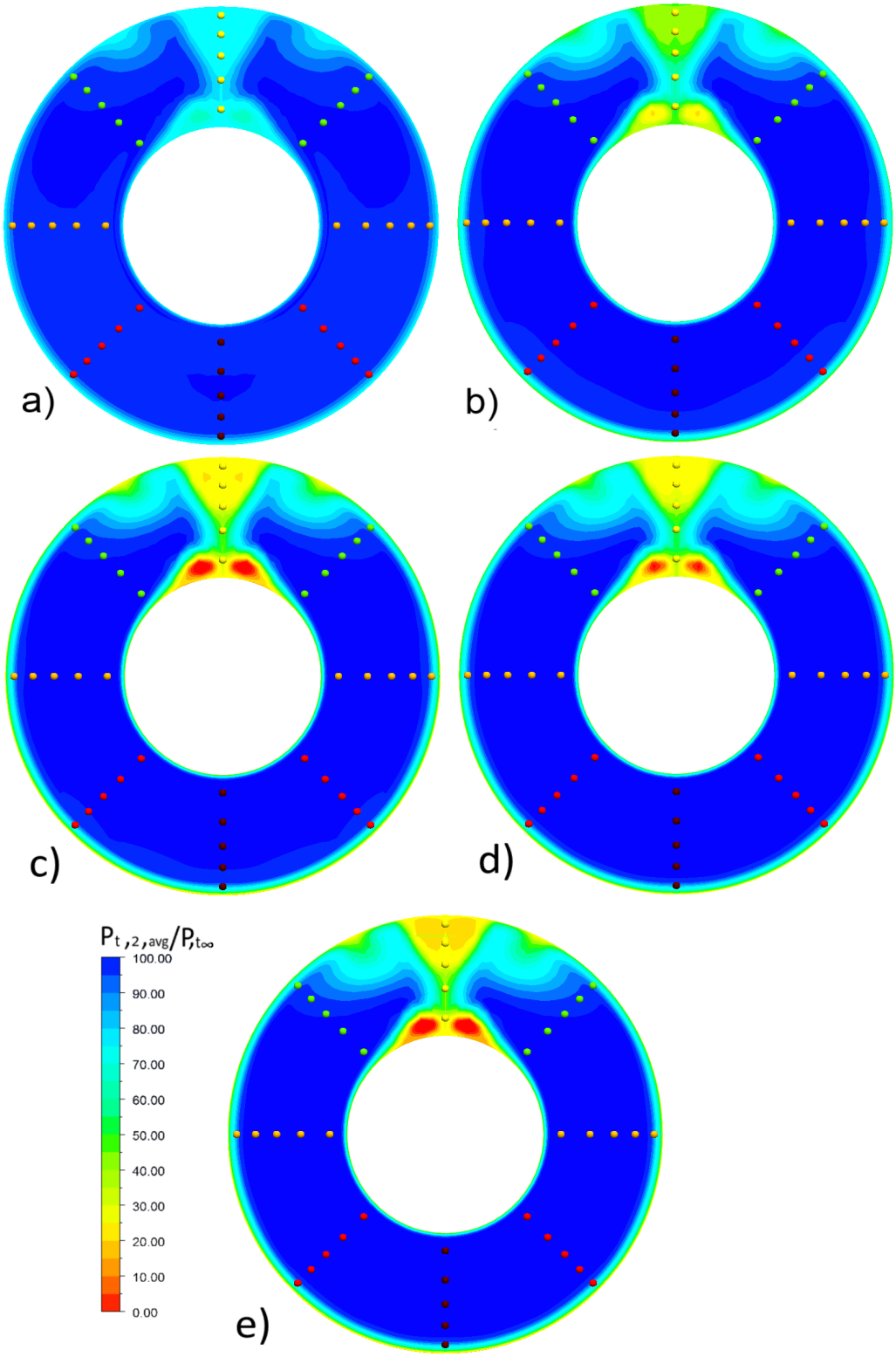

Figure 29: $p_{t,2} / p_{t,\infty}$ *of the inlet with the drive shaft case; from 5m/s to 25m/s respectively from a) to e)*

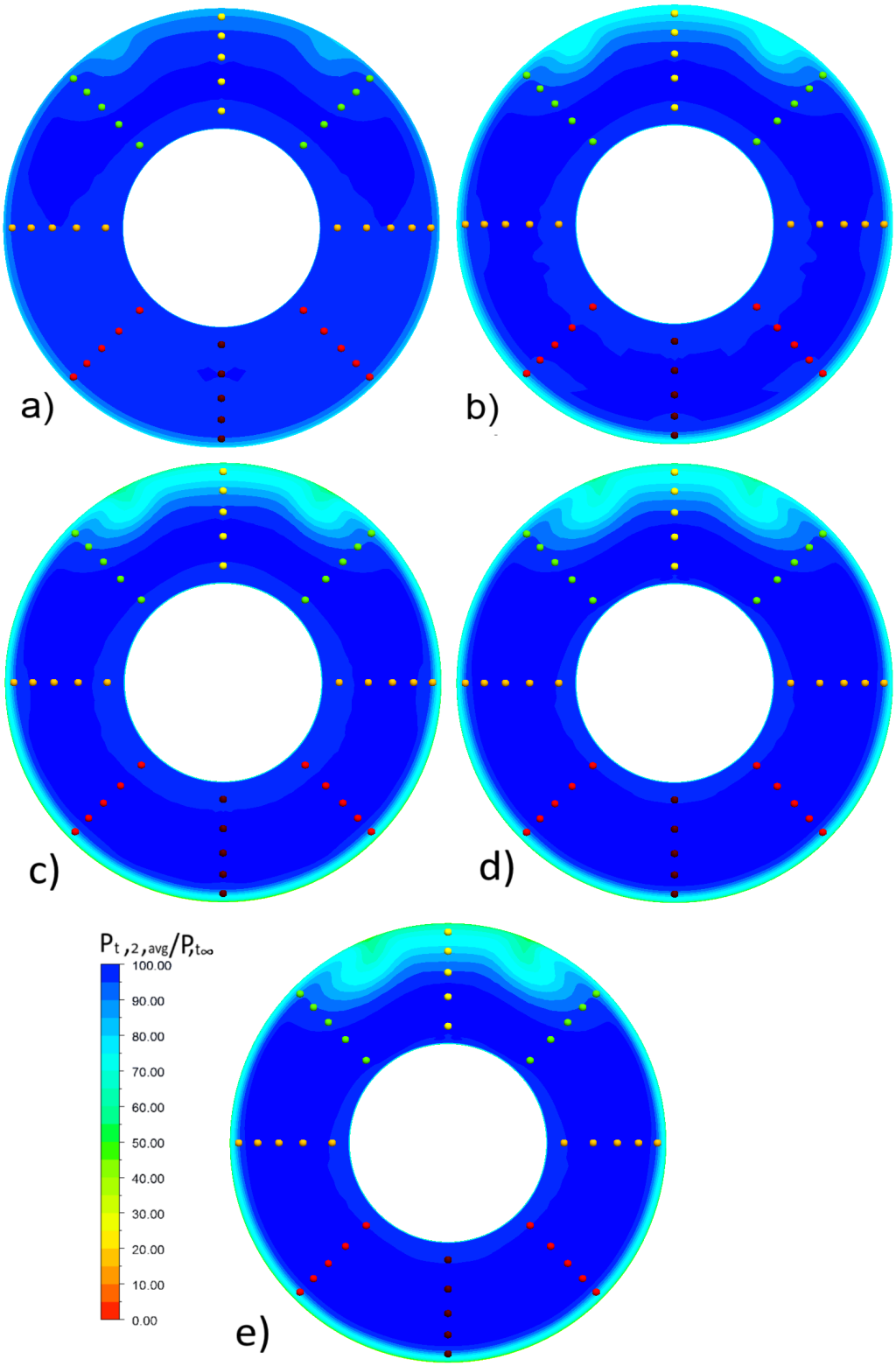

Figure 30: $p_{t,2} / p_{t,\infty}$ *of the inlet without the drive shaft case; from 5m/s to 25m/s respectively from a) to e)*

From these figures, it can be seen the effectiveness of the intake derived from the NASA BLI inlet in terms of homogeneity of the fluid pattern, which exhibits a very low distortion level at the pump interface. The red zone in the model with the drive shaft were due to recirculation eddies and, if necessary, they could be easily reduced using a shape of the hub case more hydrodynamic. In this work, we did not modify the shape of that part to allow a direct comparison between this inlet and the Castoldi flush inlet.

In these simulations we did not encounter any flow separation phenomena; using this kind of inlet seems to be easier to prevent the flow separation at the duct walls location if the diffusion factor of the intake and its slope are within prudence limits. Looking at fig. 31 it is possible to see the wall shear stress at the duct location and the total pressure distribution at the symmetry location for the inlet with the hub case at 20m/s; the wall shear stress was always positive and the boundary layer profile distension was of modest intensity.

In the next table a direct comparison between the S-X02 inlet with the original Castoldi drive shaft case and the one without the hub case is reported.

		Cruise speed [m/s]				
		5	**10**	**15**	**20**	**25**
Scoop with inlet drive shaft	$\frac{p_{t,2,avg}}{p_{t,\infty}}$ **[%]**	95.86	91.97	89.47	90.75	89.81
	$DPCP_{avg}$	0.212	0.453	0.633	0.579	0.653
Scoop inlet without drive shaft	$\frac{p_{t,2,avg}}{p_{t,\infty}}$ **[%]**	98.60	97.43	96.74	97.30	97.07
	$DPCP_{avg}$	0.006	0.015	0.025	0.029	0.032

The $DPCP_{avg}$ shows an important fluid distortion on the pump interface only in the model with the drive shaft case; this proofs that the idea explained in the next chapters of using a propulsion system which does not need a drive shaft, could be an interesting way to increase the overall performance of a generic waterjet system.

As said before, the drive shaft case of the Castoldi company seemed to be not well shaped to minimize the hydraulic losses and flow distortion. By modifying the shape of the case it could be possible to obtain a performance not so far between the two configurations, even though the configuration without the hub case should perform better in any case for obvious reasons.

The percentage of absolute total pressure lost by the S-X02 with the hub case was between 4.14% in the best case and 10.53% in the worst one. The same inlet, without the case shaft had the losses between 2.93% and 3.26%. The presence of the drive shaft was responsible of approximately the 7% of the total pressure losses at the cruise speed of 23m/s. In any case the inlet performance was lower than the original BLI inlet, which for a Reynolds number of 6.83E06 was subjected to a total pressure loss of 0.6% and a $DPCP_{avg}$ of 0.005. For the S-X06 the Reynolds number was one order of magnitude lower, so using a duct expressly designed for a waterjet application the performance should be even better with respect to the one obtained in these simulations.

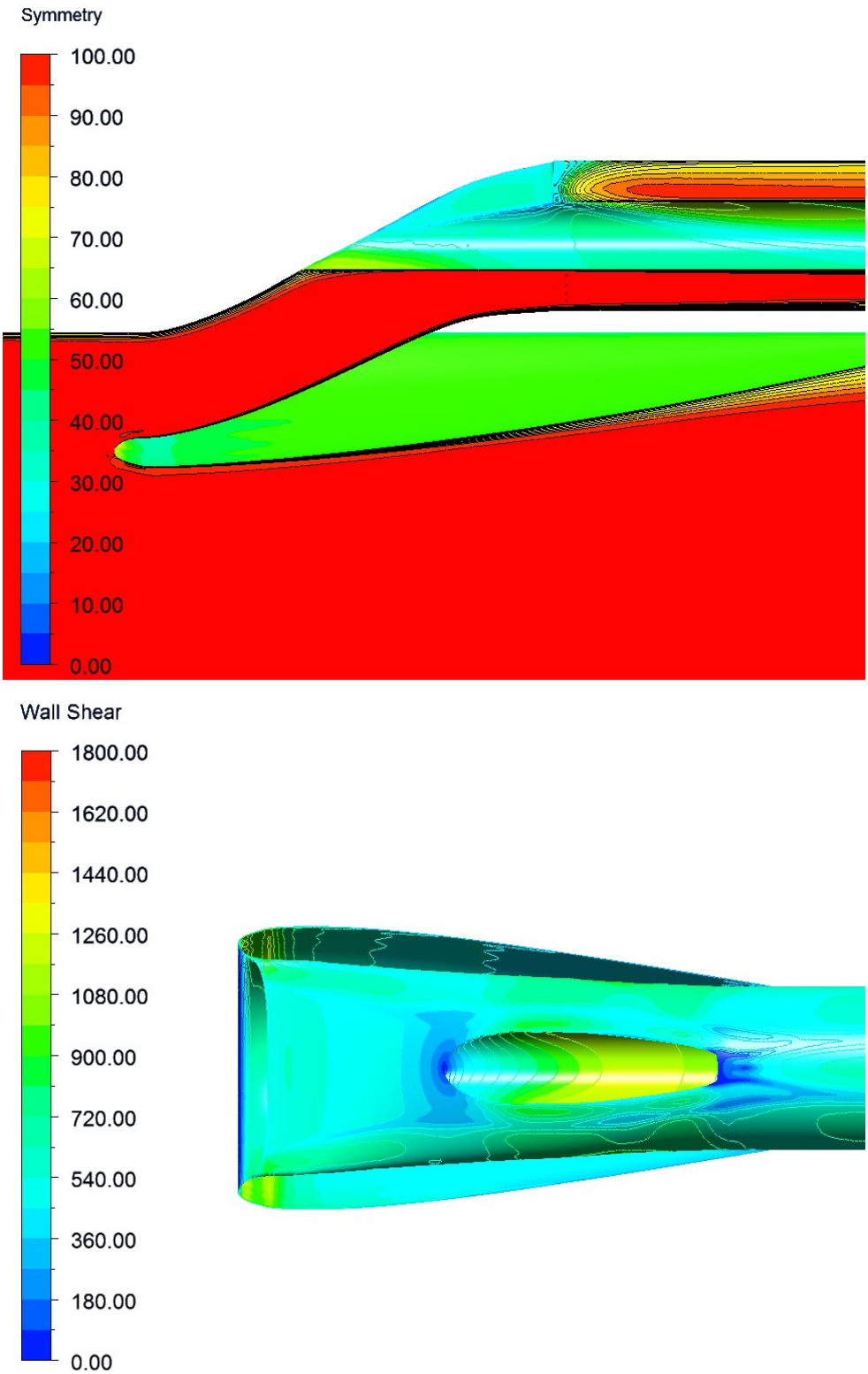

Figure 31: Up the total pressure distribution at symmetry and duct location for the waterjet with the drive shaft at 20m/s. Down the wall shear stress at the throat location.

3.4. Comparison of S-X02 and a conventional flush inlet

From the analysis of the four different inlet configurations it was possible to deduce some considerations.

The first and probably the most obvious was that the presence of a case shaft could substantially reduce the hydraulic efficiency of an intake. Of course the use of a case to encapsulate the drive shaft is better than using nothing at all, but if possible it would be better to avoid the presence of a drive shaft upstream the pump system. This choice is not easy to undertake because this means only two things: the movement of the shaft downstream the pump system or the use of another technology for the production of the torque. The former choice is sometimes implemented moving the drive shaft after the pump system but the drawbacks are many, for instance a different distribution of the mass on the boat and the necessity of a more sophisticated transmission system. The latter choice is the one suggested in the next chapter that is the substitution of the combustion engine with an electric motor coaxial with the pump system. To this day this choice is only a speculative solution because no-one has yet realised a real prototype for a waterjet system, highlighting the pros and cons of this choice.

The second consideration was that scoop inlet performance in terms of total pressure loss at the pump interface and distortion factor was substantially better than flush inlet performance. The reason of this was that a scoop inlet, having the entrance perpendicular to the water flow and a duct shape with a smooth area variation, minimizes the secondary flows and prevents the excessive boundary layer profile distension typical of the flush inlet configurations.

Looking at figure 32 it is possible to observe the behaviour of the flush and scoop inlet with the drive shaft case. The performance of the scoop inlet was substantially better in terms of both the pressure recovery and the total pressure distribution.

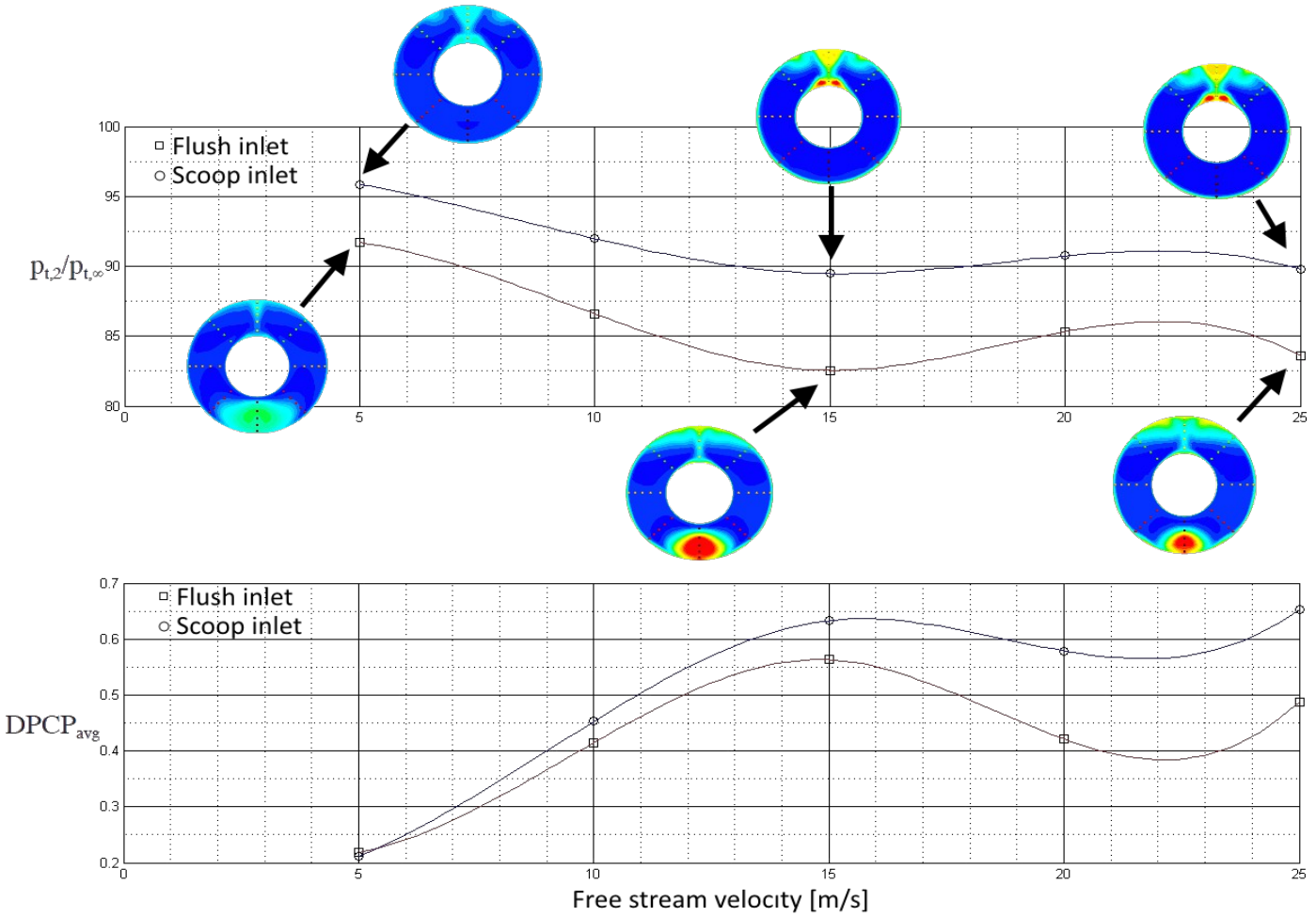

Figure 32: Effect of the speed and inlet mass flow rate on pressure recovery and distortion for the intake with the drive shaft case

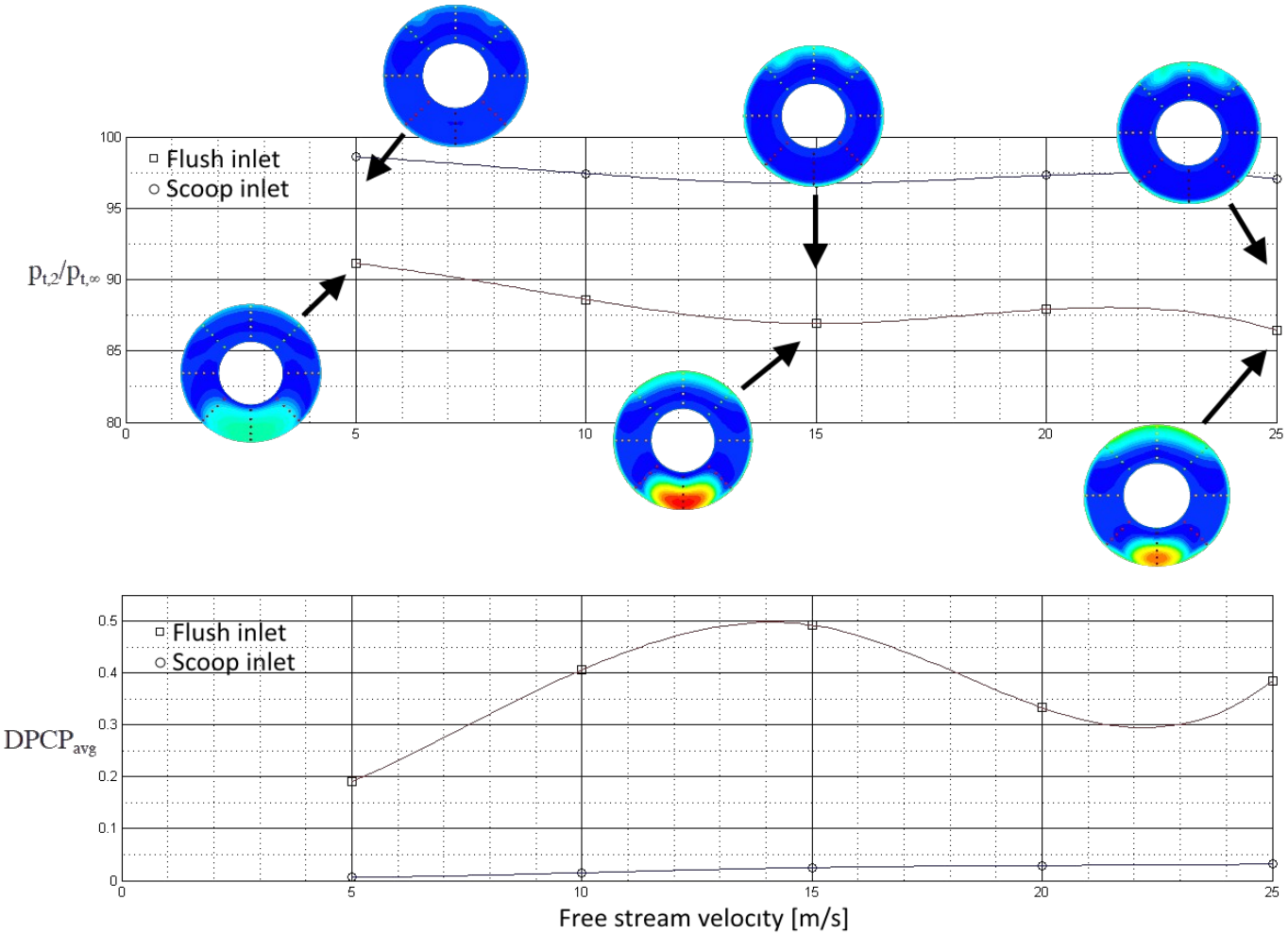

Figure 33: Effect of the speed and inlet mass flow rate on pressure recovery and distortion for the intake without the drive shaft case

The same consideration could be done observing the simulations analysis without the hub case, represented in figure 33. Without the shaft case the performance of both the inlets got better but the superiority of the scoop inlet was clear thanks to a difference in the pressure recovery up to 9.5 percentage points and a distortion parameter one order of magnitude lower, in the best case.

The benefits described since here are very important, but there is a consideration that could be even more important for water applications; the minor total pressure loss has an important consequence in having higher static pressure on the pump interface; this means that the NPSH available by the pump system was higher for a scoop inlet than a flush inlet. For this reason the cavitation phenomenon, that is the very first worry of a waterjet designer, could be better controlled. Furthermore, this saved static pressure jump did not need to be developed by the hypothetical pump system, so the gain was double. In the next table it is possible to see the area averaged static pressure at the pump interfaces.

		With drive shaft case		**Without drive shaft case**	
		$p^f_{s,avg}$ [Pa]	**$p^s_{s,avg}$ [Pa]**	**$p^f_{s,avg}$ [Pa]**	**$p^s_{s,avg}$ [Pa]**
Speed [m/s]	**5**	91861.50	96616.65	91207.13	99737.63
	10	81050.00	89181.25	84101.25	97439.25
	15	64102.52	78835.60	73409.55	94363.50
	20	57212.25	73512.50	64971.00	93197.50
	25	33620.75	59271.75	45393.00	89247.

In conclusion, from the results of this analysis the scoop inlet technology seems to be superior than flush technology. Further investigation are necessary to verify if any problem could be observed in a real model but, to this day, there is no evidence that this technology should perform worse than the traditional one. Attention should be paid to the fact that the flush inlet analysed was a commercial inlet and then it should be the state of art of flush technology whereas the scoop inlet tested was not optimised for a waterjet application and then there is more than one reason to believe that an optimised scoop inlet could perform even better; see [12] and [13] for reference about the optimization of BLI inlets in the aeronautical field.

3.5. References

[1] T. J. C. Terwisga, **Waterjet-Hull Interaction**, Ph.D. thesis, Delft University of Technology, 1996.

[2] C. Katsavos et al., **Analisi fluidodinamica e simulazione CFD dell'idrogetto Castoldi turbodrive 340 HC**, Master degree thesis, University of Padova, 2012.

[3] N. W. H. Bulten, **Numerical Analysis of a Waterjet Propulsion System**, Ph.D. thesis, Eindhoven University of Technology, 2006.

[4] J. Seddon & E.L. Goldsmith, **Intake Aerodynamics Second edition**, AIAA Education Series, 1999.

[5] B. L. Berrier et al., **High Reynolds Number Investigation of a Flush-Mounted, S-Duct Inlet With Large Amounts of Boundary Layer Ingestion**, NASA/TP-2005-213766, 2005.

[6] A. P. Plas et al., **Performance of a Boundary Layer Ingesting (BLI) Propulsion System**, 45th AIAA Aerospace sciences meeting and exhibit, 2007

[7] M.B. Carter et al., **Designing and testing a blended wing body with boundary-layer ingestion nacelles**, Journal of Aircraft, Vol. 43, No. 5, pp. 1479, 2006.

[8] M. S. Liou, **Minimizing Inlet Distortion for Hybrid Wing Body Aircraft**, Journal of Turbomachinery, Vol. 134, No. 3, 2012.

[9] H. Schlichting, **Boundary-layer theory**, Springer, chapter XXI, 1979.

[10] B. L. Berrier & B. G. Allan, **Experimental and Computational Evaluation of Flush-Mounted, S-Duct Inlets**, AIAA Paper 04-0764, 2004.

[11] P.G. Buning et al., **OVERFLOW User's Manual Version 1.8m**, Tech. Rep., NASA Langley Research Center, 1999.

[12] B.J Lee, **Optimizing a boundary-layer-ingestion offset inlet by discrete adjoint approach**, AIAA Journal, Vol. 48, No. 9, pp. 2008-2016, 2010.

[13] D.L. Rodriguez, **A Multidisciplinary Optimization Method for Designing Boundary Layer Ingesting Inlets**", Ph.D. thesis, Stanford University, 2001.

4. New Approach to the Design of a Ducted Propeller

To this day different methods have been developed to design and predict the performance of marine propellers, each one with a different level of trustworthiness and its owns pros and cons. The most sophisticated methods are probably the three-dimensional viscous flow models used in the modern Computation Fluid Dynamic software; much simpler methods are those based on blade element theories and momentum theories. CFD methods allow to understand the behaviour of the flow in detail by solving the three-dimensional incompressible Reynolds-Averaged Navier-Stokes (RANS) equations. Blade element theories study the behaviour of propellers dividing the blades in small pieces and determining the forces acting on each of these elements; they are inherently two-dimensional methods and are usually less accurate but with a low need of computational resources. Momentum theories are the easiest methods since they use an infinitely thin actuator disc on which is imposed a static pressure jump or an angular velocity jump, to simulate the action of the propeller; these theories are easy to implement but they can be used only if the conditions in the propeller plane are known.

In the next paragraph it is shown in detail a novel method outcome from the combination of momentum theories, blade element theories, blade vortex design methods, the Euler turbine equation and the Weinig [1] and Lieblein [2] methods. This method was implemented in a software called MPROP to design a ducted propeller and to predict its performance; the software was used to design an electric Rim Driven Propeller, in collaboration with the University of Southampton. What is an RDP and why it was chosen it is explained in the next chapter but it is important to know that this choice lead to have no necessity of using a theoretical model to study the tip clearance phenomenon because the tip clearance is totally absent in this kind of propulsors.

4.1. Combined momentum-blade element theory

Relative simple methods, widely used to predict the performance of propellers, are the BEM methods; originally developed by Glauert [3] and Betz [4], they combine two different theories: blade element theories and momentum theories. In blade element theory the propeller is divided into a predefined number of sections along the radius; for each section the correspondent streamtube is identified and a force balance on the two-dimensional profile of the blade is imposed. Momentum theory, developed by Rankine and Froude, assumes that the gain of total pressure in the rotor plane is caused by a pressure jump at the propeller location; from the combination of both the theories the gain of total pressure is imposed to be a direct consequence of the work done by the relative profile, strip by strip. This technique leads to obtain a set of non-linear equations that can be solved iteratively to determine the induced velocities and the aerodynamic forces on the rotor (or stator) plane. One of the limitations of BEM methods is that each element of the blade is considered independent from each other, so the surrounding elements do not influence the mass flow rate of the streamtube analysed; for this reason the radial flow is neglected and an unrealistic spanwise pressure variation is admitted. These theories were developed originally for marine screw propellers and in this field the errors in the estimation of thrust, angular momentum and velocity were considered acceptable.

4.2. A Novel Method

A way to reduce some of the inherent limitations of BEM was found by the author and here deeply described; to achieve this goal the theory at the root of BEM methods was combined with the Euler equation, the blade vortex design method and the Weinig and Lieblein methods. The method is strongly iterative and in some steps it uses numerical derivatives and integrals but it is still a method of quick resolution; to test it the method was implemented in a software called MPROP and then successfully used to design a low loaded ducted rim driven propeller (chapter 5).

The method was developed to study a generic ducted propeller (waterjet systems are, of course, included in this definition) even with more than one stage; the same method, with some changes, should be usable even for screw propellers.

The simplifying assumption used for our three-dimensional flow analysis are the following:

- The flow is steady
- The flow is axial at the inlet
- The flow is axisymmetric
- The flow is adiabatic
- The flow is incompressible
- The radial equilibrium is imposed
- The fluid is locally inviscid and non-heat conducting
- The blade geometry has zero tip clearance

The viscous losses do non affect locally the fluid flow but they are treated as total enthalpy losses stage by stage.

The method can be employed either to design a pump in a specific design condition or to test the propeller in off design conditions; the equations involved are the same but they are used in different ways or in different iterative cycles. For the sake of clarity these two approaches will be described in two different paragraphs.

4.2.1. Design point condition

In this condition the blade shape is not known *a priori* but the design specifications and the boundary conditions are known; in particular the free stream conditions, the geometrical dimensions of the system, the desired thrust and the rotational speed must be known or assumed.

The first step of the method involves calculation of the mass flow rate and average velocities at the different sections of the duct (see fig. 34) using a momentum

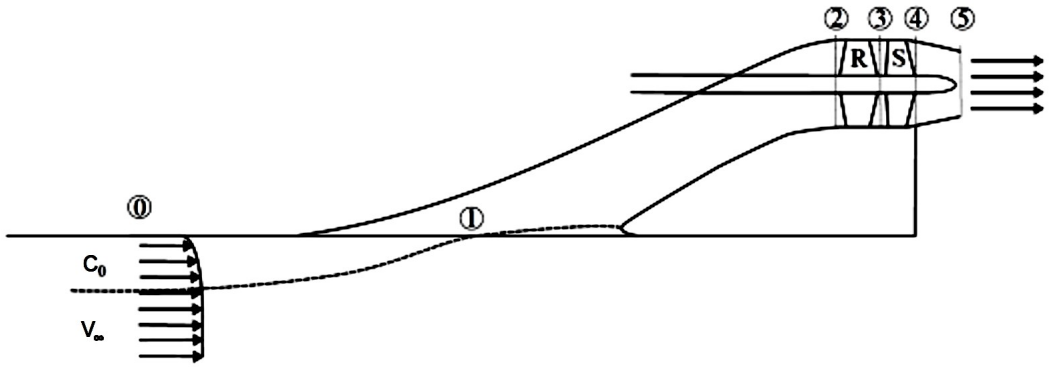

Figure 34: typical waterjet; from 0 to 5 the different sections of the system

method; on section 0, if we are using a waterjet or a ducted propeller with the inlet entrance next to the hull, the water flow is not undisturbed because of the turbulent boundary layer on the hull surface; the average velocity is then not known *a priori* and to calculate it the capture area should be defined; to calculate that area an approximation proposed in [5] is used. The shape is approximated with a rectangular box with a width of 1.3 times the pump diameter; the height of the box is calculated, once the velocity distribution in the boundary layer is known, using the following equation:

$$h = \left(\frac{\dot{m}}{\rho v_\infty \lambda D} \cdot \frac{n+1}{n} \cdot \delta^{(1/n)} \right)^{\frac{n}{n+1}} \qquad (4.1\ a)$$

This equation holds if h is bigger than the depth of the boundary layer. Instead, if the suction depth h is smaller than the boundary layer thickness, an alternative model is used:

$$h = \frac{\dot{m}}{\rho v_\infty \lambda D} \cdot \frac{\delta}{n+1} \qquad (4.1\ b)$$

$\dot{m}$ is the mass flow rate, ρ is the fluid density, λ is an empirical value imposed equal to 1.3, D is the pump diameter, δ is the depth of the boundary layer thickness and n is a constant dependent from the value of the Reynolds number.

If the Reynolds number is included between $5 \cdot 10^5$ and $1 \cdot 10^7$:

$$n = 7$$

$$\delta = 0.37 \cdot L \cdot Re^{-\frac{1}{5}} \qquad (4.2\ a)$$

If the Reynolds number is bigger than $1 \cdot 10^7$ but smaller than $1 \cdot 10^9$:

$$n = 9$$

$$\delta = 0.27 \cdot L \cdot Re^{-\frac{1}{6}} \qquad (4.2\ b)$$

where L is the length of the wetted hull.

On the other sections the distributions of static pressure, total pressure and velocity components are calculated and used when needed; when the averaged quantities are used (momentum theory) they are calculated averaging them with respect to the area or the mass flow rate. In particular the bar symbol is used to indicate a mass flow rate averaged quantity and the hat symbol to indicate the area averaged quantity; here some examples:

$$\hat{p}_i = \frac{1}{A_i} \int_{r1}^{r2} 2\pi r p \, dr \qquad (4.3\ a)$$

$$\bar{p}_i^T = \frac{1}{\dot{m}} \int_{r1}^{r2} 2\pi r \rho c_z p^T \, dr \qquad (4.3\ b)$$

$$\bar{c}_i = \frac{1}{\dot{m}} \int_{r1}^{r2} 2\pi r \rho c_z c \, dr \qquad (4.3\ c)$$

$$\hat{c}_i = \frac{1}{A_i} \int_{r1}^{r2} 2\pi r c \, dr \qquad (4.3\ d)$$

The subscript i is used to indicate the correspondent section (see fig. 34); the subscript z is used to indicate the axial component of the vectorial quantity.

Pressures and velocities at different sections are interdependent and related to the hydraulic efficiency of the axial propeller, to the type of blade vortex design chosen, to the hydraulic head of the propeller and to the losses in general. The mass flow rate used in the previous formula is not known at the beginning of the iteration process so its value is part of the iteration process. In this part of the

method we are using a momentum theory so one-dimensional formulas are used to correlate the known quantities to the mass flow rate value. If the external part of the duct does not contribute to the thrust, knowing the speed of advance, the design thrust, the hub and shroud diameters at the different sections it is possible to calculate the mass flow rate from the general thrust equation:

$$T = \dot{m} \cdot (\bar{c}_{z5}^2 - \bar{c}_{z1}^2) - A_{1p} \cdot (\hat{p}_1 - \hat{p}_a) + A_5 \cdot (\hat{p}_5 - \hat{p}_a) \tag{4.4}$$

where A_{1p} is the projected area of A_1 on the plane perpendicular to the speed advancement direction.

If the nozzle is a so-called Kort nozzle or a pump jet [6] and then part of the thrust is produced by the external surface of the duct, it is not possible to use the previous formula. The ratio between the total thrust and the thrust produced by the pump (rotor and stator) is usually called τ:

$$\tau = 1 - \frac{T_{duct}}{T} \quad \text{or} \quad \tau = \frac{T_{pump}}{T} \tag{4.5}$$

The value of τ is a function of the shape of the duct and it is correlated to the mass flow rate. Different methods are used to know τ in ducted propeller applications but the theory discussed in this document is not concerned about this calculation then the value of τ will be considered known using one the existing methods; see [6] for reference.

It is then possible to write the following equation:

$$T \cdot \tau = T_{pump}$$

$$T_{pump} = \dot{m} \cdot (\bar{c}_{z4}^2 - \bar{c}_{z2}^2) - A_2 \cdot (\hat{p}_2 - p_a) + A_4 \cdot (\hat{p}_4 - p_a) - \int_{r_{e2}}^{r_{e4}} 2\pi r (p - p_a) dr \tag{4.6}$$

Where the last component is the force acting on the shroud surface of the pump; see [7] and [8] for reference.

The propeller thrust is a design condition so, using the previous formulas, it is possible to know the first iteration values of the mass flow rate, of the inlet velocity and of the outlet velocity; all the quantities which are not known should

be supposed equal to an appropriate value at the first iteration.

The second step of the method is about the calculation of the hydraulic head and of the vortex design coefficients; the hydraulic head produced by the pump has to be high enough to allow an increment of the total pressure to the value calculated in the previous step. It is quite easy to calculate it if you consider the efficiency of the pump equal to one, if you neglect the viscous losses and if you suppose of having a stator that is able to totally de-swirl the fluid. Unfortunately these conditions are often very far from reality, so even the hydraulic head has to be calculated with an iterative process. Furthermore, if a ducted propeller is used, to calculate the mass flow rate equation (4.6) has to be used; in this case the pressure distribution on the internal surface of the duct is connected to the value of the tangential velocity (swirl velocity) at the exit of the rotor pump, then the iterative calculation of the mass flow rate and the iterative calculation of the hydraulic head have to be placed inside another iterative calculation. The parameter chosen to iterate both quantities is the tangential velocity at the rotor exit.

In any case, in the design phase the distribution of the tangential velocity at the rotor exit must be chosen by the designer. The tangential velocity distribution is imposed by a different shape of the blade: the design strategy is then very important because it could considerably change the cavitation margin and the shape of the blade. As it is known, the blade vortex design describes the swirl distribution of the flow downstream the blade; in the present document, the blade vortex design chosen is a combination of three different vortex designs: free-vortex design, constant-vortex design and forced-vortex design; it is left to the designer’s discretion to choose one of these methods rather than a combination of them. See [9] for instance.

It is possible to calculate the ideal hydraulic head necessary to develop the designed thrust as:

$$H = -\frac{1}{\rho g} \cdot \left[(\hat{p}_1 - \hat{p}_5) + \frac{\rho}{2}(\bar{c}_{z1}^2 - \bar{c}_{z5}^2) + \frac{\rho}{2}(\bar{c}_{\theta 1}^2 - \bar{c}_{\theta 5}^2) \right] + \sum_{i=1}^{5} \Delta H_{loss,i} \qquad (4.7)$$

$\bar{c}_{\vartheta 1}$ is the tangential velocity at the inlet location and it is equal to zero by hypothesis; $\bar{c}_{\vartheta 5}$ is equal to zero if the stator is able to totally de swirl the fluid flow or it will be dependent from the $\bar{c}_{\vartheta 3}$ value.

$c_{\vartheta 3}$ is a function of the values of the vortex design coefficients:

$$c_{\theta 3} = \frac{a}{r} + k + b \cdot r \qquad (4.8)$$

a, b and k are respectively the constants of the free-vortex design, the constant-vortex design and the forced-vortex design. It is not possible to define all the three values of the vortex design coefficients because a complete definition of them would be equivalent to have fixed the hydraulic head *a priori*; therefore one of these the three values cannot be imposed by the designer and it will be a result of the calculation. At the beginning of the iteration process, $\bar{c}_{\vartheta 3}$ is estimated.

The term $\sum_{i=1}^{5} \Delta H_{loss,i}$ is the sum of the hydraulic head losses stage by stage; it is dependent from the mass flow rate and the geometry of the duct.

The wall viscous losses are treated as a total hydraulic head loss stage by stage:

$$\Delta H_{loss,i} = \frac{F_{ST}}{\rho g \frac{(A_i + A_{i+1})}{2}} \qquad (4.9)$$

The frictional wall forces are calculated supposing turbulent the flow at the wall surfaces [10]:

$$F_{ST} = 0.036 \rho \hat{c}_z^2 \cdot 2\pi r l \left(\hat{c}_z \frac{l}{\upsilon} \right)^{1/5} \qquad (4.10)$$

The stator losses are calculated as shown in the previous equations but in addition to that value there is a term that took into account the blade losses; this term is calculated using the aerodynamic coefficient C_d that is calculated in the second

part of the method; therefore even the first iterative value of the stator losses has to be estimated. The rotor losses are taken into account in the efficiency term so they will not be considered in the $\sum_{i=1}^{5} \Delta H_{loss,i}$ term:

$$H_t = \frac{H}{\eta_{hy}^{R}} \tag{4.11}$$

where η^{R}_{hy} is the hydraulic efficiency of the rotor, which has to be estimated at the first iteration, and that is calculated in the second part of this method with eq. (4.24).

Once calculated the first iteration value of the hydraulic head and of the theoretical hydraulic head with eq. (4.7) and (4.11) it is possible to determine the remaining unknown quantities.

The radial derivative of the stagnation pressure in the absolute frame of reference may be written as:

$$\frac{1}{\rho}\frac{dp^{T}}{dr} = \frac{1}{\rho}\frac{dp}{dr} + c_z\frac{dc_z}{dr} + c_\theta\frac{dc_\theta}{dr} + c_r\frac{dc_r}{dr} \tag{4.12}$$

For axial pumps and compressors it is common to neglect the radial velocity component imposing a radial equilibrium condition on the stream surface:

$$\frac{dp}{dr} = \rho\frac{c_\theta^2}{dr} \tag{4.13}$$

This choice allows the simplification of equation (4.12), even if this leads to an unrealistic representation of the fluid physical quantities distributions; however the error committed is usually small, so this procedure is commonly accepted in the literature; see [11] for reference.

From (4.12) and (4.13) we can write

$$\frac{1}{2}\frac{dc_z^2}{dr} = \frac{1}{\rho}\frac{dp^{t}}{dr} - \frac{c_\theta}{r}\frac{d(r\,c_\theta)}{dr} \tag{4.14}$$

Remembering that for an incompressible fluid:

$$h^T = \frac{1}{\rho} p^T \tag{4.15}$$

and using the Euler turbine equation:

$$h^{T,3} = \omega\left(r_3 c_{\theta 3} - \cancel{r_2 c_{\theta 2}}\right) = \omega a + \omega k r + \omega b r^2 \tag{4.16}$$

it is possible to integrate equation (4.14) to obtain the axial distribution in function of a generic reference radius r_m and the corresponding axial velocity c_{zm}

$$c_{z3} = c_{zm}\sqrt{1 + \frac{2}{c_{zm}^2}\cdot I}$$

$$I = \left[\left(r^2 - r_m^2\right)\left(\omega b - b^2\right) + \left(r - r_m\right)\left(\omega k - 3 b k\right) + \left(\frac{1}{r} - \frac{1}{r_m}\right) a k - \ln\left(\frac{r}{r_m}\right)\left(2 a b + k^2\right)\right] \tag{4.17}$$

c_{zm} could be chosen to be equal to the area averaged velocity and then deduced from the definition of mass flow rate:

$$\dot{m} = \rho \cdot A_3 \cdot \hat{c}_3 = \rho \cdot A_3 \cdot c_{zm} \tag{4.18}$$

The reference radius r_m is therefore the radius at which the local axial velocity is equal to the averaged velocity; the following identity must be imposed for the closure of the problem:

$$c_{zm} \equiv \frac{1}{A_3}\int_{r_{i,3}}^{r_{e,3}} 2\pi r c_{z3} dr \tag{4.19}$$

where $r_{i,3}$ and $r_{e,3}$ are the internal and external radii of the rotor exit stage.

Remembering that for an incompressible fluid the hydraulic head is equal to the total enthalpy over the gravitational acceleration, from eq. (4.16) is possible to write the following

$$H_t = \frac{1}{\dot{m}}\int_{r_{i,3}}^{r_{e,3}} 2\pi r \rho c_{z3} \frac{\omega}{g}\left(a + k r + b r^2\right) dr \tag{4.20}$$

with c_{z3} from (4.17).

From the previous equations it is possible to calculate the unknown blade vortex coefficient and then the second iteration value of tangential velocity at the rotor exit. At this point of the method the first iteration of the first part is concluded; therefore, all the other averaged physical quantities can be calculated now, if needed.

The procedures explained up to this point are summarised in the next figure.

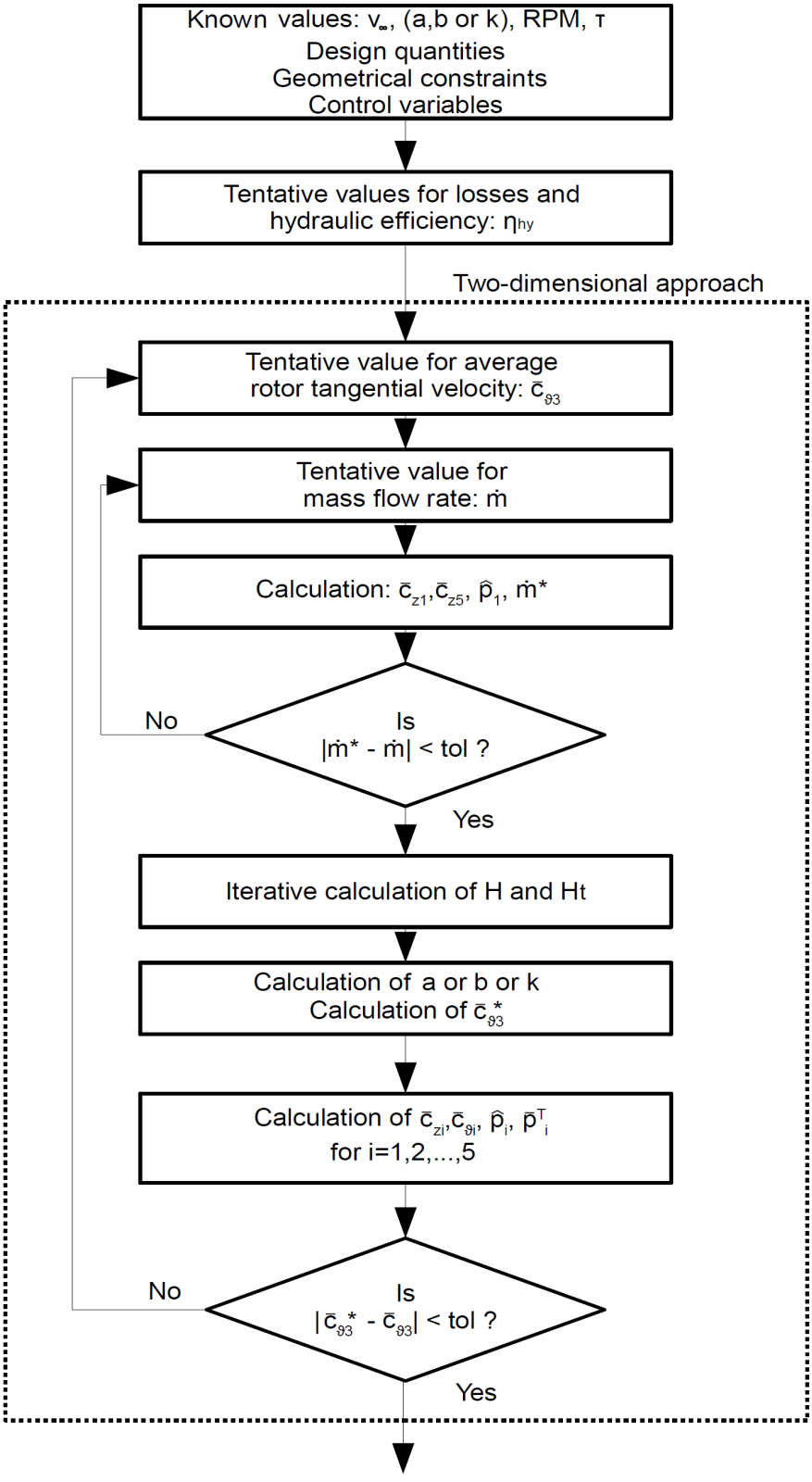

Figure 35: Flow chart of the first half of the method

To calculate the efficiency and the shape of the pump blades a method derived from blade element theories is used; first of all, a discretization of the domain has to be made using concentric streamtubes; the method is based on the assumption that each streamtube could be analysed independently from the rest of the flow without taking expressly into account the radial equilibrium among the strips; in each streamtube the flow is treated two-dimensionally. Differently from conventional BEM methods, the streamtubes are not defined by dividing the domain into equal area zones but dividing the flow into equal mass flow rate strips. In general, the area at the rotor entrance could be substantially different from the exit one then the use of equal areal passage strips could lead to generate errors in the calculation of the velocity and pressure distributions; to do this it is essential to know the mass flow rate and the axial distribution of the axial velocity which are calculated in the previous steps and in particular in equation (4.17).

For each streamtube the locally averaged axial velocity and tangential velocity are known at the inlet and at the outlet of the machinery stage; the rotational speed is also known from the design data. For each streamtube and for each correspondent aerofoil the velocity triangles are then known; with these information it is possible to calculate the mean line and the thickness distribution of the aerofoil which is responsible of achieving the wanted fluid deviation; to this end NACA 4 digit aerofoils are used in this document but all type of aerofoils could be used if necessary, changing the corresponding formulas where needed.

For each aerofoil lift and drag coefficient are calculated respectively with Weinig and Lieblein methods. This choice was made to keep this method fast but another selection could be made to increase the accuracy of the method; for example the use of a panel/integral boundary layer method (IBLM), could represent an interesting way to predict lift and drag coefficients, taking into account the effect of the values of the local Reynolds number; see [12] for instance.

Weinig in [1] found a way to predict the performance of a cascade of straight-line profiles using potential flow and conformal transformation methods; he determined that defining R as the radius of the circle that map conformally any

strip of the cascade plane and α_{st} as the inclination of the straight-line aerofoil of which we want to predict the performance, it is possible to define the following correlations:

$$\tan\alpha_{ST}=\tan\gamma\frac{R^2-1}{R^2+1} \tag{4.21 a}$$

$$\frac{c}{s}=\frac{1}{\pi}\left(\cos\gamma\ln\frac{R^2+2R\cos\alpha_{ST}+1}{R^2-2R\cos\alpha_{ST}+1}+2\sin\gamma\tan^{-1}\frac{2R\sin\alpha_{ST}}{R^2-1}\right) \tag{4.21 b}$$

$$k_0=\frac{\Gamma_{cascade}}{\Gamma_{single}}=\frac{4s}{\pi c}\frac{R}{R^2+1}\frac{\cos\alpha_{ST}}{\cos\gamma} \tag{4.21 c}$$

$$C_l=2\pi k_0\sin\delta \tag{4.21 d}$$

with γ the stagger angle in the real plane, δ the angle of attack and c/s the blade solidity.

By mapping a general cascade into a cascade of straight-line profiles and neglecting the drag contribution it is possible to determine the shape of the aerofoil that should be used to obtain the wanted fluid deviation at the corresponding strip. We choose to not neglect the drag contribution so we joined the Weinig method with the Lieblein method.

Lieblein in [2] found a way to correlate the drag coefficient to a parameter called diffusion factor, with an empirical correlation:

$$D=\left(1-\frac{\cos\beta_1}{\cos\beta_2}\right)+\frac{\cos\beta_1}{2\frac{c}{s}}(\tan\beta_1-\tan\beta_2) \tag{4.22 a}$$

$$C_d=2\frac{\sin^2\beta_{inf}}{\sin^2\beta_e}\frac{\mathring{\theta}}{c} \tag{4.22 b}$$

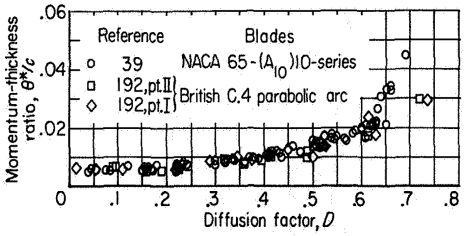

(4.22 c)

with β_e, β_i and β_{inf} the angles of the relative velocities in the velocity triangles.

Once C_d is known it is possible to calculate C_l with the following formula.

$$C_l = 2\frac{s}{c}\frac{c_{\theta_2} - c_{\theta_1}}{w_{inf}} - C_d \cdot \cos\beta_{inf} \tag{4.23}$$

Knowing C_d for each aerofoil it is also possible to calculate the hydraulic loss of the blades; adding this to the wall viscous loss, the hydraulic efficiency of the rotor stage can be found using the following equation:

$$\eta^R_{hy,2-3} = \frac{p_3^0 - p_2^0}{p_{3\,id}^0 - p_{2\,id}^0} \tag{4.24}$$

The value of the rotor hydraulic efficiency and the value of the losses at the stator stage (calculated in a similar way) could be used as new values of these quantities to start a new iteration of the method.

Once the method has finished iterating (usually after 3 or 4 iterations convergence is reached) for each streamtube the stagger angle of the equivalent straight-line profile is known. Using a 4 digit NACA aerofoil it is possible to calculate the real stagger angle supposing that a NACA aerofoil behaves as the correspondent straight-line profile when the line which connect the trailing edge to the point with ordinate y_A of the main line of the NACA aerofoil is parallel to the straight-line aerofoil. The reason of this assumption is the following: when that line is parallel to the flow the lift coefficient is equal to zero so, at least when both the straight-line profile and the 4 digit NACA aerofoil have no lift, they behave in the same manner. The angle of attack at which an aerofoil has no lift is called α_0 or zero lift angle; for a 4 digit NACA aerofoil it could be assumed as:

$$\alpha_0 = -100\frac{y_A}{l} \tag{4.25}$$

Once all the real aerofoils are determined it is possible to calculate the real shape of the blades simply stacking them in the spanwise direction. A scheme that summarizes the method explained in this section is shown in figure 36.

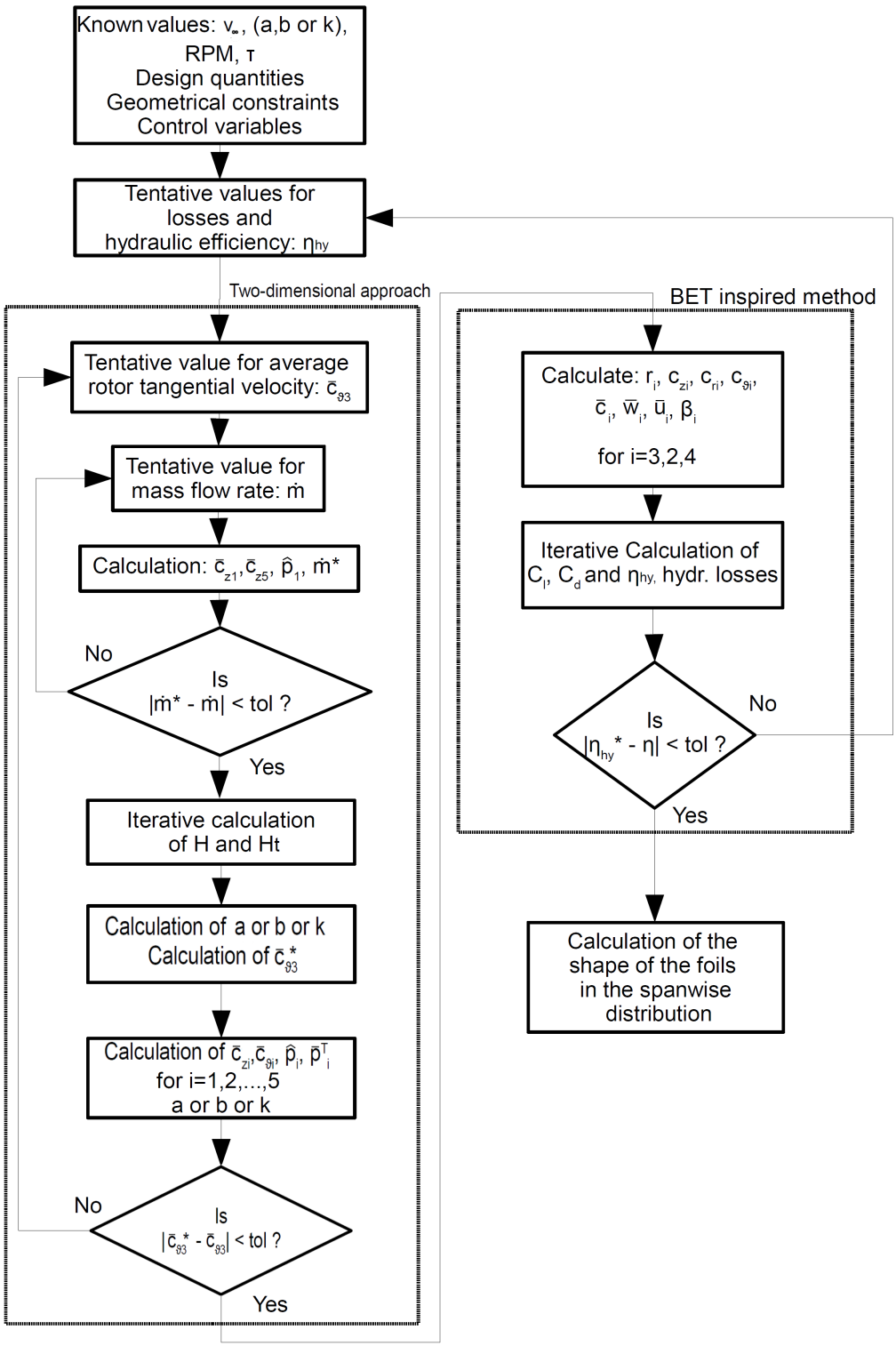

Figure 36: Flow chart of the method

4.2.2. Off-design point condition

In this condition the shape of the pump blades is known; what it has to be calculated now is then the behaviour of the propulsor if some of the design conditions are changed; for example, by changing the advancement speed of the cruise we could strongly influence the mass flow rate at the machinery stage altering the velocity triangles in the pump system. The equations used are the same of the previous paragraph but used in a different way; the method is now described underlining the differences from the use in the design point condition.

In this condition the thrust generated by the propulsor is known *a priori* so there is no possibility of knowing the mass flow rate without estimating the hydraulic head of the pump. The method is still an iterative method.

At the first step the mass flow rate is estimated; using equations (4.1), (4.2) and Bernoulli's equation the static pressure and the velocity components are calculated at the sections 0, 1 and 2 (see fig. 34). The same quantities are calculated for section 3 and 4 using a method inspired by BEM: the duct is divided in a predefined number of strips with the same mass flow rate and for each one it is calculated how the aerofoils deviate the flow; again the strips could have an area at the entrance of the stage that is different from the exit area. The rigorous way to do that is recalculating, each time the method finishes one iteration, the new exit area of the streamtubes and then extracting, from the 3D design of the blade, the exact shape of the aerofoils at those locations; this procedure is very tedious and, if the off-design points are not too far from the design point condition, the strips dimensions should not be too different from those used in the design condition. Therefore in the present work the shape of the strips and the shape of the aerofoils are assumed equal to the ones calculated in the design point condition; this will lead us to commit an error but its value is supposed to be small.

Once the streamtubes dimensions are fixed, the value of the hydraulic head is still unknown; to know that it is important to calculate the radial distribution of the velocity components. In the previous paragraph we used an imposed vortex design distribution and then we calculated the relative components; now we cannot do

that because we do not know *a priori* how the aerofoils deviate the flow. Conventional BETs use induction coefficients to calculate the flow deviation. In the present method a different approach is used; in particular for each aerofoil C_l and C_d values are calculated using the Weinig and Lieblein methods and the following identity is imposed to be true:

$$\frac{dh^T}{dr} = \frac{1}{2}\frac{dv_z^2}{dr} + \frac{v_\theta}{r}\frac{d(r\,v_\theta)}{dr} \tag{4.26}$$

The previous formula came from the total enthalpy definition and from the Euler equation, as explained in the previous chapter.

The aerodynamic coefficients calculated with the previous methods are not independent variables because C_l and C_d are functions of the velocity components at the leading edge (which are known) and of the velocity components at the trailing edge (which are unknown); furthermore, the radial distribution of the axial and tangential velocity are not known *a priori* and the total enthalpy distribution is dependent from the loss distribution and then from C_d. An iterative procedure is used; the velocity triangles at the trailing edge are hypothesized and C_l and C_d are calculated iteratively using the Weinig and Lieblein methods. After this the radial distribution of the total enthalpy is calculated taking into account the hydraulic losses while the radial distribution of the tangential velocity is calculated from the previous results. Using equation (4.26) it is then possible to calculate the axial velocity distribution and the axial velocity component for each streamtube, using as reference velocity the area averaged axial velocity (that is equal to the mass flow rate divided by the stage area), and as reference radius the radius at which the local axial velocity is equal to the averaged velocity. The iteration is then concluded and it is possible to do another iteration using the new values of the velocity components as new inputs.

Once velocity components and the static pressure for the sections 3 and 4 are computed, it is possible to calculate the same quantities at the exit section and then calculate the new value of the mass flow rate. The strategy adopted is to fix the exit pressure (in a subsonic propeller the exit pressure is usually equal to the

atmospheric pressure) and then calculate the exit velocity from the kinetic component of the total pressure. The exit area is known so, multiplying this value by the density and the axial velocity, it is possible to find the new mass flow rate value.

In the following figure is possible to see the flow chart of this part of the method.

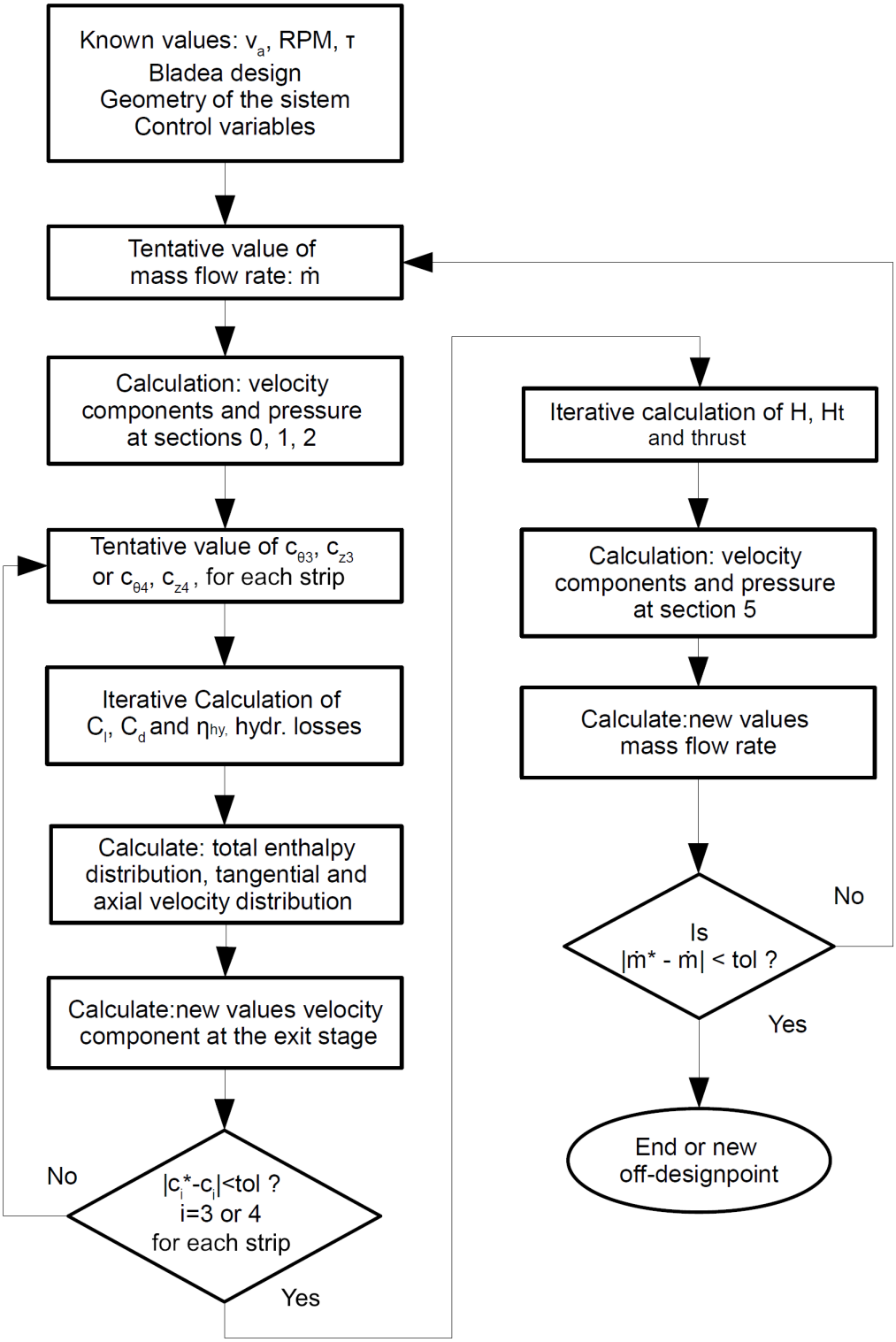

Figure 37: Flow chart of the method in the off-design point condition

4.3. References

[1] F.S. Weinig, **Theory of two-dimensional flow through cascades**, Princeton University press, Aerodynamics of turbines and compressors, pp. 13, 1964.

[2] S. Lieblein, **Experimental flow in two-dimensional Cascade**, national aeronautics and space administration, aerodynamic design of axial-flow compressors, pp.183, 1965.

[3] H. Glauert, **Airplane propellers**, Aerodynamic Theory, pp. 169–360. Springer, 1935.

[4] A. Betz, **Das maximum der theoretisch möglichen ausnützung des windes durch windmotoren**. Zeitschrift für das gesamte Turbinewessen, 1920.

[5] N. W. H. Bulten, **Numerical Analysis of a Waterjet Propulsion System**, Ph.D. thesis, Eindhoven University of Technology, 2006.

[6] R.I. Lewis, **Turbomachinery Performance Analysis**, Elsevier, chap. 8, 1996

[7] P. G. Hill & C. R., **Mechanics and Thermodynamics of Propulsion**, Reading, Addison Wesley, Mass.,1992

[8] E. Benini, **Propulsione Aerea**, Cleup, 2006

[9] S. Farokhi, **Aircraft Propulsion**, John Wiley & Sons Inc, chap. 7, 2008.

[10] Schlichting, **Boundary layer theory**, springer, 1979.

[11] R. H. Aungier, **Turbine Aerodynamics: Axial-Flow and Radial_Inflow Turbine Design and Analysis**, Asme Press, 2006.

[12] E. Benini, **Significance of blade element theory in performance prediction of marine propellers**, Ocean Engineering, Vol. 31, No. 8-9, pp. 957, 2004.

Page intentionally left blank

5. Design and Test of a Low Loaded Ducted Rim-Driven Propeller

The availability of more compact and more efficient brush-less motors, thanks to the use of rare-hearth permanent magnet technology, combined with the necessity of minimize the environmental impact of marine propeller are playing a key role in the transition from conventional propeller systems to electric ones. Among all different types of electric propellers Rim-Driven Propellers (RDPs) offer unique capabilities in term of overall performance. These propellers do not have a proper drive shaft because they are driven by the rim or, in other words, the mechanical torque is imposed directly to the shroud of the blades; RDPs are then inherently ducted propellers. It is not a new idea, RDPs were used in USSR ships in the middle of the 20th century [1]; however, only in the recent years, thanks to the developing of new electric motor technologies, they have come into wide use.

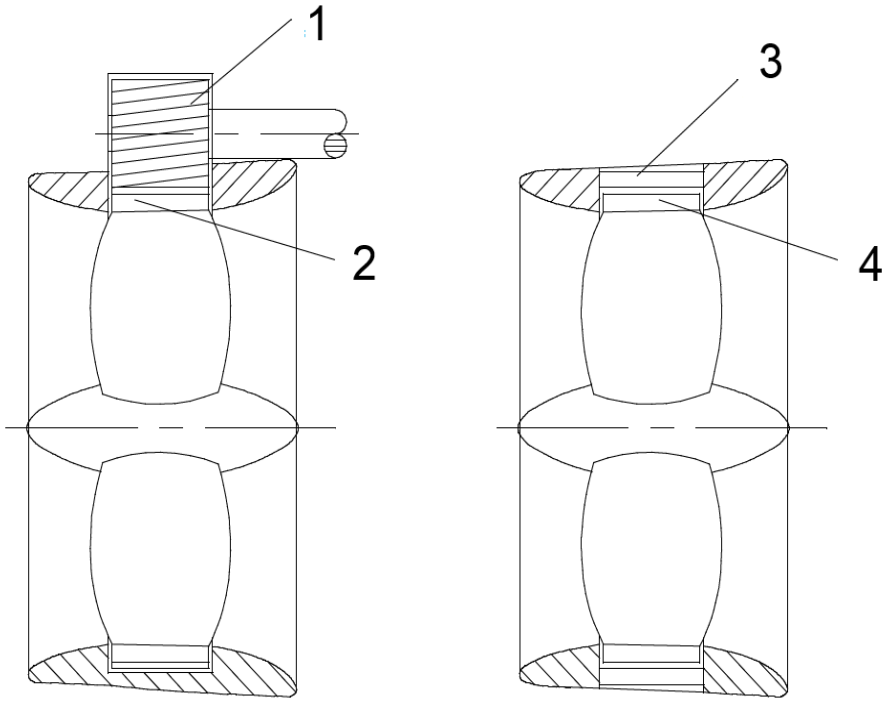

Figure 38: Scheme of two rim driven propellers. On the left an old RDP actuated by mechanical gears, on the right a new one actuated by an electric motor. 1) Small driving gear 2) large driven gear 3) electric stator 4) permanent magnet rotor. Image from [2]

“Advantages offered by the use of a RIM-driven propeller in thruster unit include:

- Reduced pressure head losses and more uniform wake in propeller disk due to elimination of struts and pod in thruster channel.
- Reduction in thruster-induced noise and vibration due to flow equalization in front of the propeller and elimination of tip vortices in wake of propeller blades.
- No risk of cable entrapment for propeller shaft in case of hub-less propeller design.
- No loss of energy due to gap between propeller blade and thruster channel wall” [2]

RDPs are used prevalently in the ducted propeller field but faint steps in this direction have been done even in waterjet propulsion; in [3] and [4] it is possible to see two preliminary studies of two different waterjet systems equipped with RDPs; in this documents noteworthy benefits are demonstrated from the use of this technology even though both authors agreed that several technical problems must be solved before using this kind of propellers inside a commercial waterjet system.

5.1. Design of a low loaded RDP with MPROP

Due to the belief that electrical motors and RDPs will hold a main role in the future of ship propulsion, a collaboration with the Abu Sharkh's research group at the University of Southampton and TSL technology was undertaken at the beginning of 2014; the fruit of this collaboration was the low loaded ducted RDP that is the subject of this chapter. The propeller was designed from scratch during a five months intern-ship at the University of Southampton and then built and tested; to design the RDP the method described in chapter 4 was used once implemented in a code called MPROP. This software is easy-fitting to the iterative geometry manipulation (typical of the design process) and easily usable joined with optimization algorithms. The code is able to virtually design a propeller for given technical and boundary conditions in a very short time: the design

procedure for this particular propulsor, once fixed all the variables and constraints, lasted five minutes, using a conventional laptop and without using any optimization algorithm. The code is designed to work with waterjets systems and ducted propellers with a single rotor, single rotor with stator and with two contra rotating rotors.

Few design constrains were imposed in the design phase:

- Maximum internal diameter of the hydraulic rotor of 0.1m.
- Total length of the propulsor of 0.15m.
- Minimum thrust at 0.5m/s equal respectively to 100mm 30.2N.
- Section of the duct made with a NACA 0023. The unusual shape of the duct was due to allow the housing of the electrical motor; the τ value was 0.6 at the design point condition (see eq. 4.5).
- Propeller rotor of three blades and a propeller stator of four blades, both designed with a pure constant-vortex design and shaped using 11 NACA four digit aerofoils for each blade.

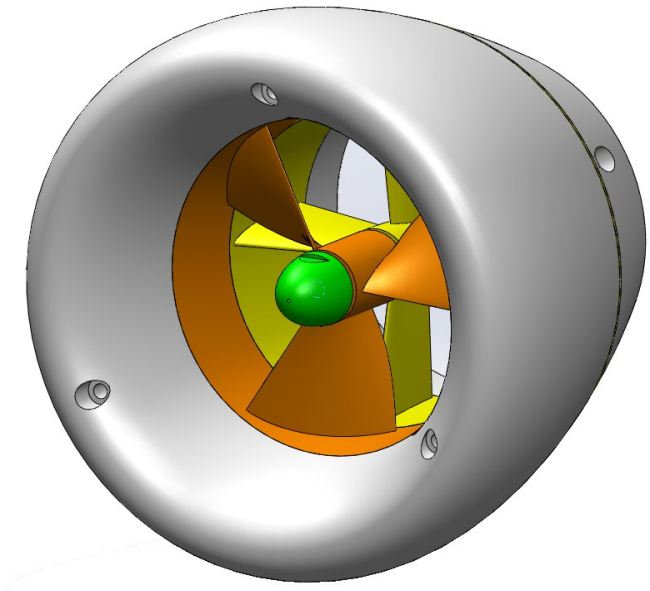

Figure 39: RDP developed at the University of Southampton

Looking at figure 39 it is possible to see the CAD representation of the RDP calculated with MPROP; the solidity from the hub to the tip of the rotor was between 1.0 and 0.4 whereas the solidity of the stator was between 1.6 and 0.5. The performance of the RDP predicted by MPROP are showed in the following table. The maximum predicted thrust was 36.45N at the minimum advancement speed of 0.2m/s; the minimum thrust was 16.35N at maximum advancement speed of 1.5m/s. The hydraulic power consumption was between 63.78W and 73.42W; the power consumption was at the minimum value when the advancement speed was at the maximum. The rotation speed was constant for all the advancement speeds and equal to the design rotation speed value of 1300RPM.

	Advancement speed [m/s]			
	0.2	**0.5**	**1.0**	**1.5**
Thrust [N]	36.45	30.2	23.59	16.35
Hydraulic power [W]	73.42	72.58	69.48	63.78
Mass flow rate [kg/s]	19.61	19.73	20.17	20.88
Total head rise [m]	0.309	0.302	0.279	0.240
Rotation speed [RPM]	1300	1300	1300	1300

5.1.1. Mesh and simulation setting

The behaviour of the RDP was investigated as function of the advance speed using the commercial CFD code, CFX. A multi block grid was constructed for this purpose (see fig. 40); rotor and stator domains were meshed using a structured grid whereas the surrounding environment was meshed using an unstructured grid. The mesh grid represented a circumferential portion of the total domain: 120° for the surrounding environment and the rotor domains and 90° for the stator domain; the surrounding environment domain had a radius of 0.7m and a length of 1.3m. The number of elements used was near to 12 millions of which 5.5 millions for the surrounding environment, 4 millions for the rotor and 2.5 millions for the stator. For the rotor and the stator meshes the Turbogrid mesher was used; the topology method used was “ATM optimized” and for the “boundary layer refinement control” the “first element offset” method was used with a y+ equal to

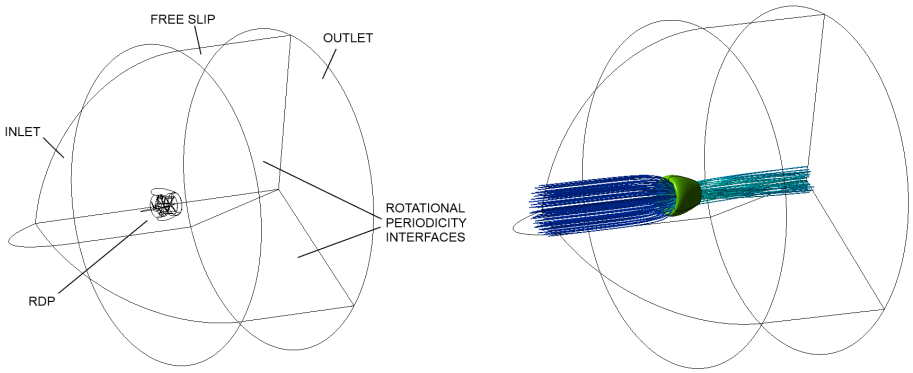

Figure 40: Computational domain for CFX simulation

30 for a Reynold number of 100000.

For the surrounding environment the ICEM mesher was used; a prismatic mesh of 20 layers was used on the external duct surface to better describe the boundary layer behaviour; the first layer thickness was between 1E-06m and 5E-06m. The remaining domain was meshed using tetrahedral elements; the minimum size was 1E-03m and the maximum was 2E-02m. The element size of the surface mesh was 5E-04m for the duct surface and the interfaces with rotor and stator whereas it was 1E-06m for the hub surface.

The turbulence model used was the k-ω SST and the heat transfer was set to isothermal (298.15K). The simulation was made without the possibility of cavitation because MPROP excluded this circumstance. Boundary conditions were applied as follows: on the inlet a velocity inlet condition was applied corresponding to the desired undisturbed velocity; four different advancement speeds were tested: 0.2, 0.5, 1, 1.5m/s. On the outlet, a relative static pressure condition was imposed with a value of 0Pa. On the lateral surfaces a rotational periodicity condition was imposed. All the wall surfaces, except the most external surface, were assumed to be smooth walls and a no slip condition was imposed; on the external surface it was applied a free slip wall condition. A rotating domain at 1300RPM was used for the rotor domain and 3 stage averaged velocity interfaces were used to connect the surrounding environment domain with the rotor domain, the rotor domain with the stator domains and the stator domain with the surrounding environment domain. The simulation was steady state.

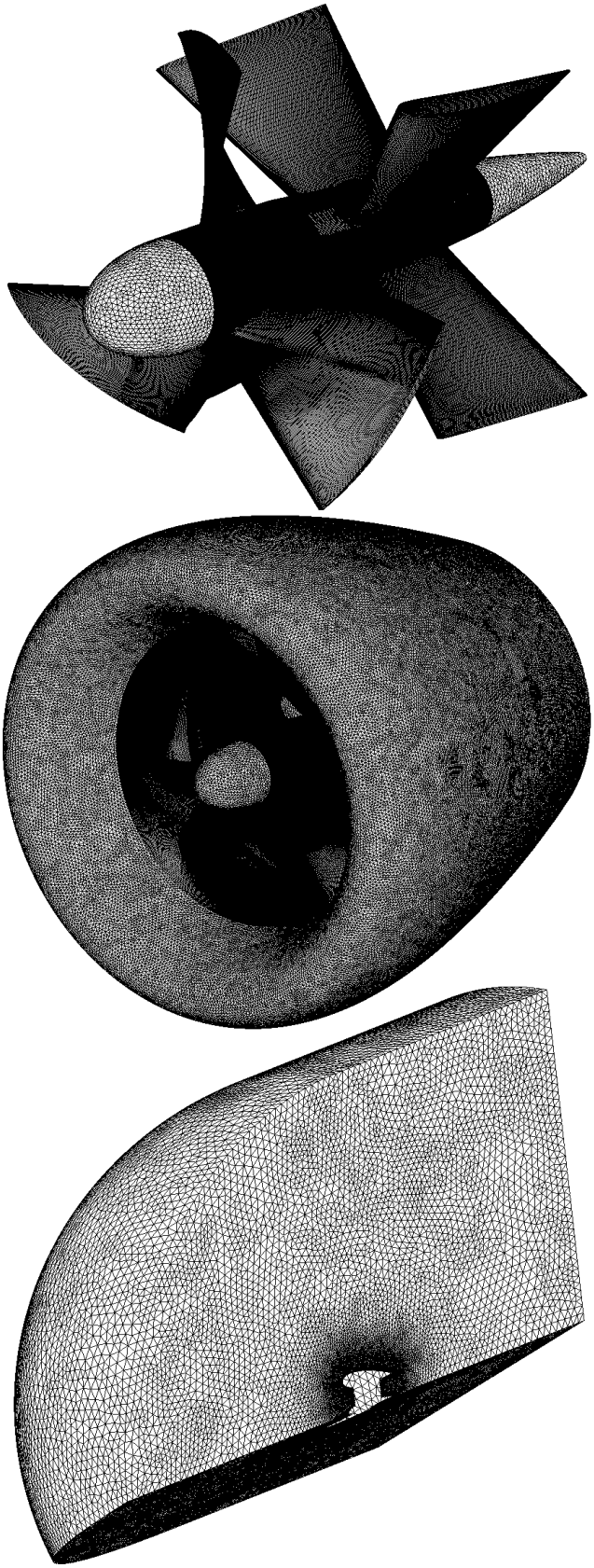

Figure 41: Surface mesh of the different domains

5.1.2. CFD results

This paragraph summarizes the results of the CFD analysis performed for the RDP at the different advancement speeds. The results were considered acceptable when the maximum residuals of the solution equations were less than $1 \cdot 10^{-4}$ and when the thrust, mass flow rate and power values were stable. The y+ value were lower than 1 on the walls of the duct in the surrounding environment domain whereas it was between 30 and 100 on the walls of the rotor and stator domains.

In the next table it is possible to see the overall performance of the RDP at different speeds. The maximum predicted thrust was 36.44N at the minimum advancement speed of 0.2m/s; the minimum thrust was 17.67N at maximum advancement speed of 1.5m/s. The hydraulic power consumption was between 53.29W and 60.65W; the power consumption was at the minimum value when the advancement speed was at the maximum. This behaviour had a trend similar to the one found using MPROP. Once again the rotation speed is constant and equal to the design rotation speed value of 1300RPM.

	Advancement speed [m/s]			
	0.2	**0.5**	**1.0**	**1.5**
Thrust [N]	36.44	31.54	24.27	17.67
Hydraulic power [W]	60.65	59.99	57.61	53.29
Mass flow rate [kg/s]	18.03	18.13	18.52	19.17
Total head rise [m]	0.270	0.264	0.264	0.214
Rotation speed [RPM]	1300	1300	1300	1300

In the next figure it is possible to see the velocity and relative total pressure distribution at 50% of the span of the RDP at the cruise speed of 0.5m/s.

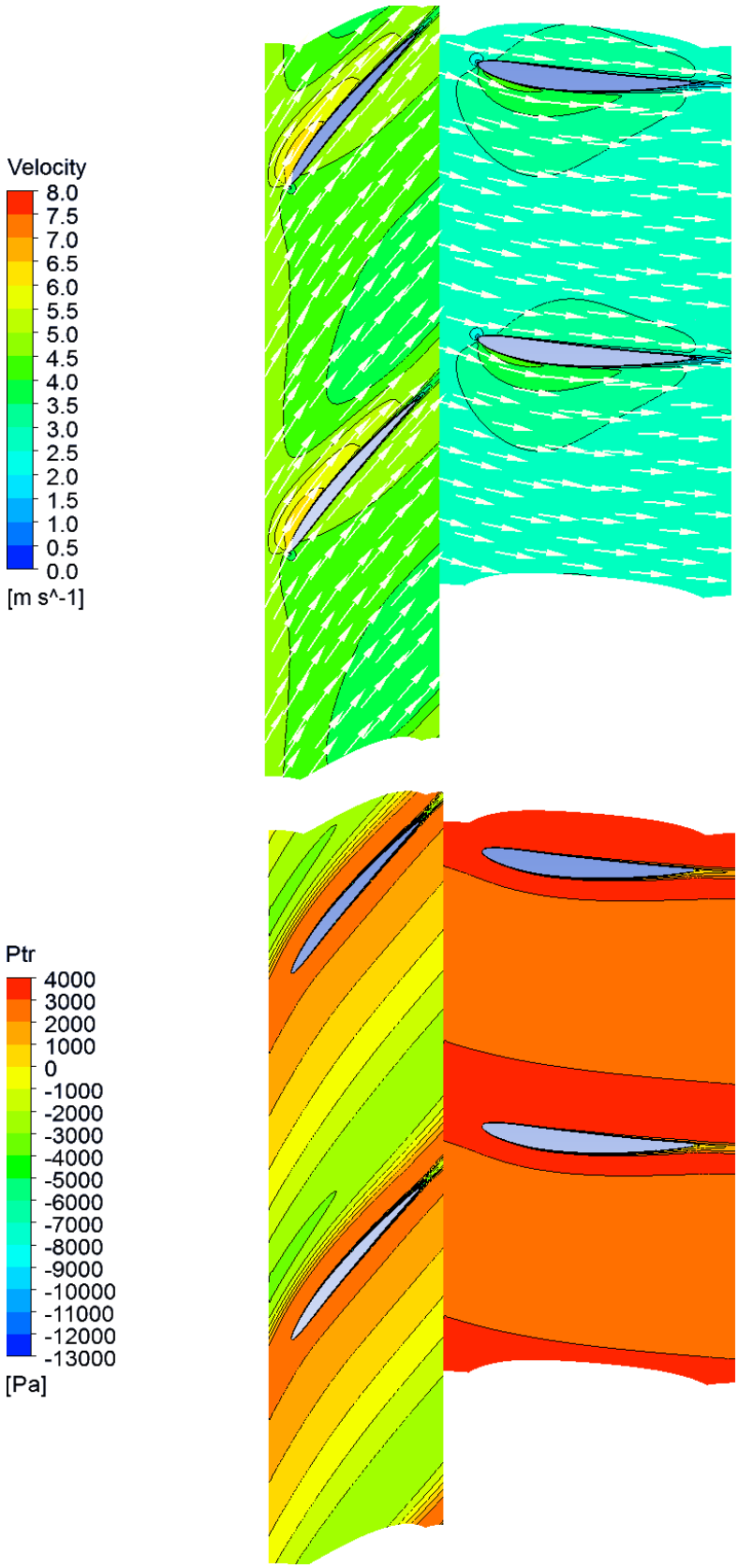

Figure 42: Velocity and relative total pressure distribution at 50% of the span at 0.5m/s

5.2. Experimental test and results

After the design and simulation procedures the RDP described since here was built and tested; the tests were done in the Solent towing tank at the Southampton Solent University (fig. 43). The towing tank is 60m length, 3.7m wide and 1.8m deep; the carriage top speed is 4m/s.

The RDP (fig. 44) was fixed with a clamp to the measurement structure which was mounted on the tank carriage; the structure was composed of a low drag arm, a load cell, two rotational joint and different supports (fig. 45). The carriage was able to go through the tank at a fixed speed allowing to measure the performance of the propulsor at different advancement speeds.

The test procedure was conducted first measuring the drag of the protruding part without the RDP then fixing the propulsor with the clamp to the structure; several tests have been done at different advancement speeds and at different rotation speeds.

Figure 43: Towing tank at the Southampton Solent University

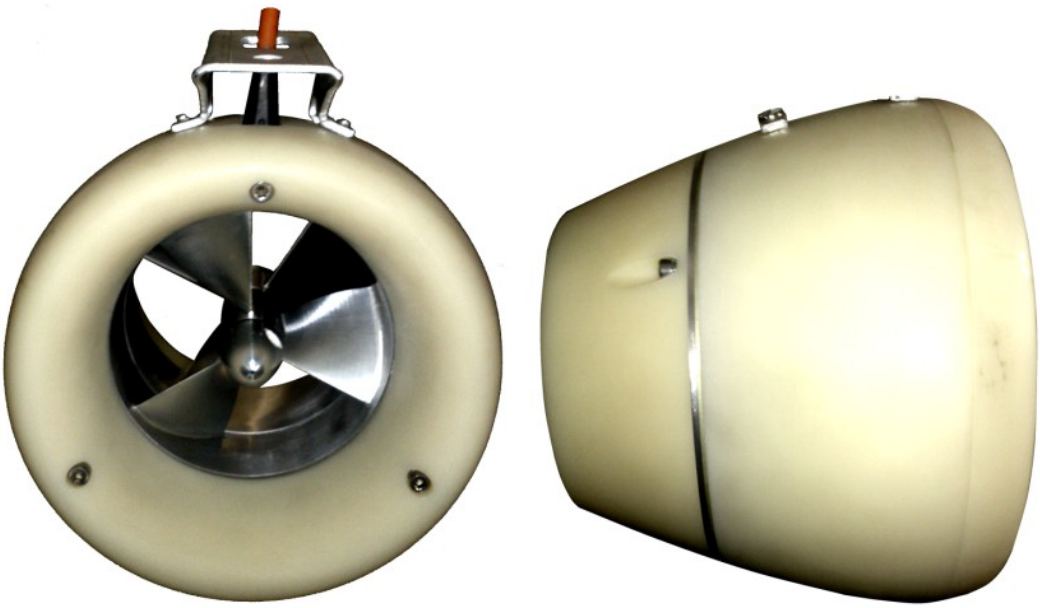

Figure 44: Front and lateral views of the RDP tested a the University of Southampton

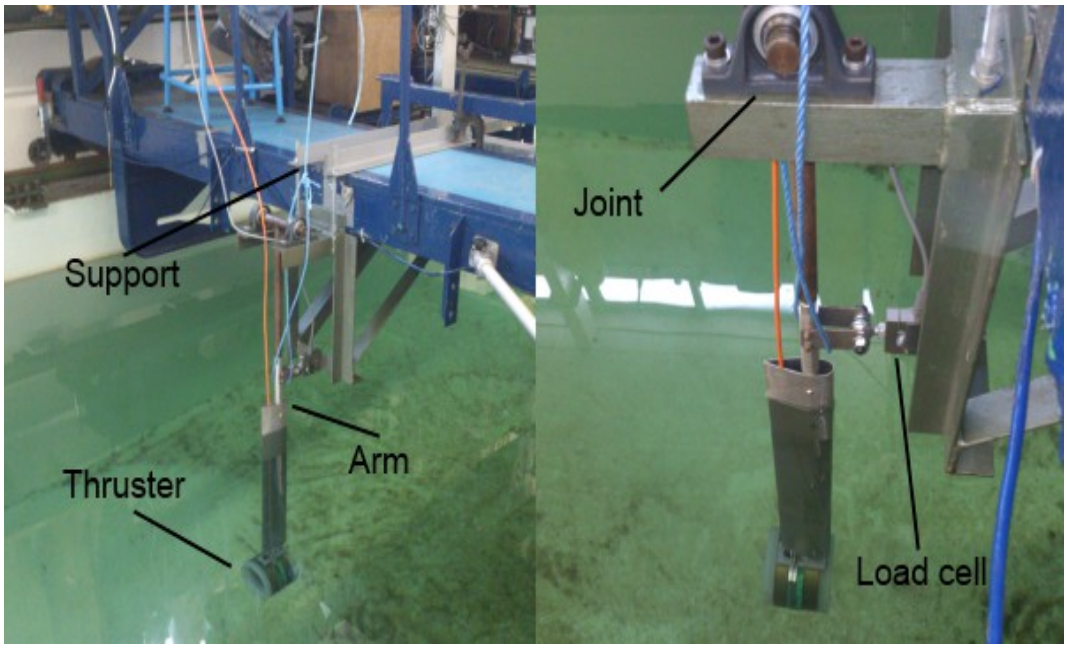

Figure 45: Experimental set up

Due to technical reasons the rotational speed was not exactly equal to 1300RPM and the advancement speeds were not exactly equal to the ones used in the previous paragraphs. The result that are shown in the following pages are then outcomes of a numerical interpolation. The error of the thrust measure could be assumed equal to ±0.3N. It was not possible to measure directly the hydraulic head and the mass flow rate which were not used as reference parameters. It was either not possible to measure the hydraulic power, but it was possible to measure the electric power; the hydraulic power was then estimated after the subtraction of all the losses contributes not directly connected to the hydraulic power.

The electrical losses removed were the cable loss, the diode loss, the copper loss and the core loss. The first two losses were directly measured whilst the last two were calculated using the following formulas:

$$\mathrm{CoreLoss_{Power}} = \mathrm{K_{cl}} \cdot \mathrm{RPM}^{1.6} \tag{5.1}$$

$$\mathrm{CopperLoss_{Power}} = 3 \cdot \mathrm{R_c} * \mathrm{I_p^2} \tag{5.2}$$

with RPM the rotation speed, I_p the phase current, K_{cl} the core loss coefficient and R_c the copper resistance. All the electrical coefficients were directly measured or estimated by the research group of the professor S. M. Abu Sharkh of the University of Southampton; see [5] and [6] reference.

In addition to these values, it was necessary to remove also the mechanical power associated to the bearing losses and gap loss. The bearing losses are due to the friction of the hub with the two bearings; they re calculated with the following formula:

$$\mathrm{T_{bearing}} = \left(0.18 \cdot \mathrm{F_{rotor}} \cdot \mathrm{R_{mean}}\right) \tag{5.3}$$

with R_{mean} equal to 0.0075m.

The gap loss was due to the fact that between the electric rotor and the electric stator there was a small layer of water that allowed the rotation but produced a non negligible viscous loss; this value was calculated by A. Dubas, at the time Ph.D. student at the University of Southampton, and it was estimated to be equal to 10.09W at 1300RPM; see [7] for reference.

The main results of the tests are summarized in the following table.

	Advancement speed [m/s]			
	0.2	**0.5**	**1.0**	**1.5**
Thrust [N]	35.10	30.89	23.84	17.67
Electric power without electric losses[W]	87.82	88.36	85.70	81.77
Mechanical losses [W]	13.42	13.55	13.27	13.02
Hydraulic power [W]	74.40	74.81	72.43	68.75
Rotation Speed [RPM]	1300	1300	1300	1300

5.3. Data Analysis

The results described in the previous paragraphs are summarized in the next table. It is possible to see how the MPROP thrust error was between -3.85% and 7.47% with an error at the design point (0.5m/s) of 2.17%; the error in the estimation of the power was between 1.32 and 7.22 with an error in the design point of 2.98%. This demonstrate that even though the method used to write MPROP does not take in account three dimensional fluid effects and use simplified model to predict blade coefficients, it is still a good method to design and predict the performance of a low loaded ducted propeller at least in the region near to the design point condition. The fact that the error is bigger in the zones farther from the design point was expected and the reason was probably that the models used by MPROP to estimate lift and drag did not predict well these coefficients when the incidence of the fluid flow was different from the optimal one; the use of more complex models to predict these coefficient will be tested in the near future to see if it is possible to increase the performance of the method.

The performance of CFX in the prediction of the thrust values were similar to the ones of MPROP in a region not too far for the design condition but substantially better at the advancement speed of 1.5m/s where CFX has no error respect to the test results. The behaviour of CFX in the prediction of the hydraulic power was, on the contrary, not good and the error was between 18.48% and 22.48%.

	Advancement speed [m/s]

	0.2	0.5	1.0	1.5
MPROP Thrust [N]	36.45	30.2	23.59	16.35
CFX Thrust [N]	36.44	31.54	24.27	17.67
Tests Thrust [N]	35.10	30.89	23.84	17.67
MPROP Hydr. Power [W]	73.42	72.58	69.48	63.78
CFX Hydr. Power [W]	60.65	59.99	57.61	53.29
Tests Hydr. Power [W]	74.40	74.81	72.43	68.75
Thrust Error MPROP [%]	-3.85	2.17	1.05	7.47
Power Error MPROP [%]	1.32	2.98	4.08	7.22
Thrust Error CFX [%]	-3.82	-2.10	-1.80	0
Power Error CFX [%]	18.48	19.81	20.47	22.48

From analysis made at later stage and not reported in this work, it was possible to find that several causes which could be the reason of the large discrepancy of the CFX power estimation; in particular the values of the density of the mesh at the duct surface, the value of the wall friction coefficient at the shroud surface and type of interfaces used for the rotor and stator mesh (stage method) could be responsible of part of the error: different settings could produce changes in the power prediction up to 10%. Unexpectedly these changes did not substantially affect the thrust value.

Anyway this work was not undertaken to validate CFX but, on the contrary, to validate the method at the root of MPROP; for these reason the results obtained were considered totally satisfactory. It is important to underline that the design procedure of the pump lasted not more than five minutes with MPROP whereas the simulation procedure lasted 20 hours with CFX; then this method, or similar ones, could allow to save a lot of time without loss in term of prediction capabilities.

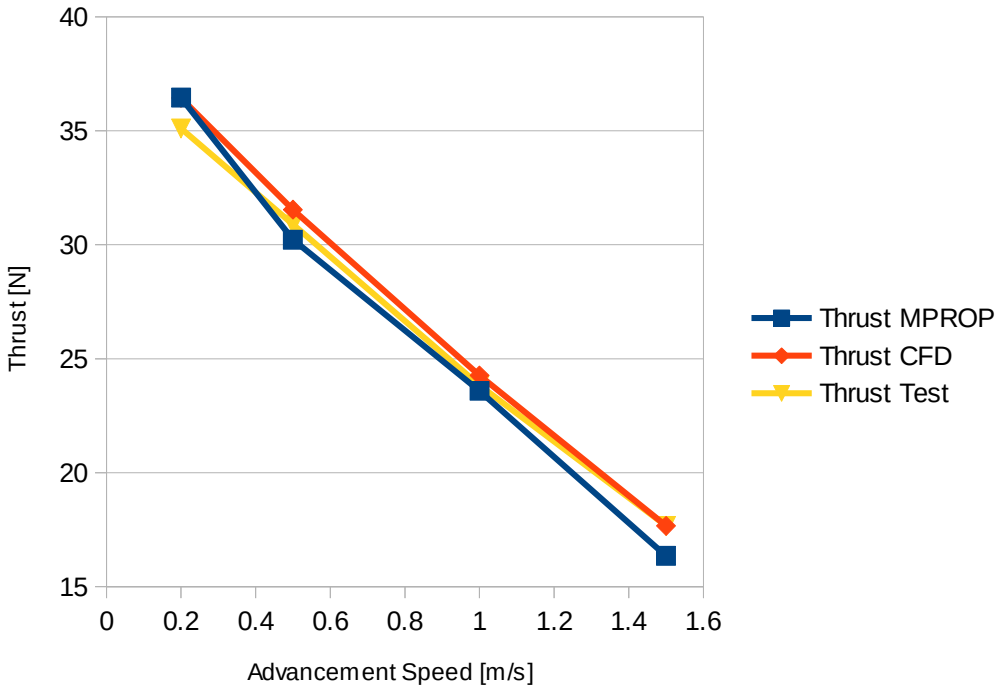

Figure 46: Thrust curves of the RPD obtained from MPROP, CFX and tests.

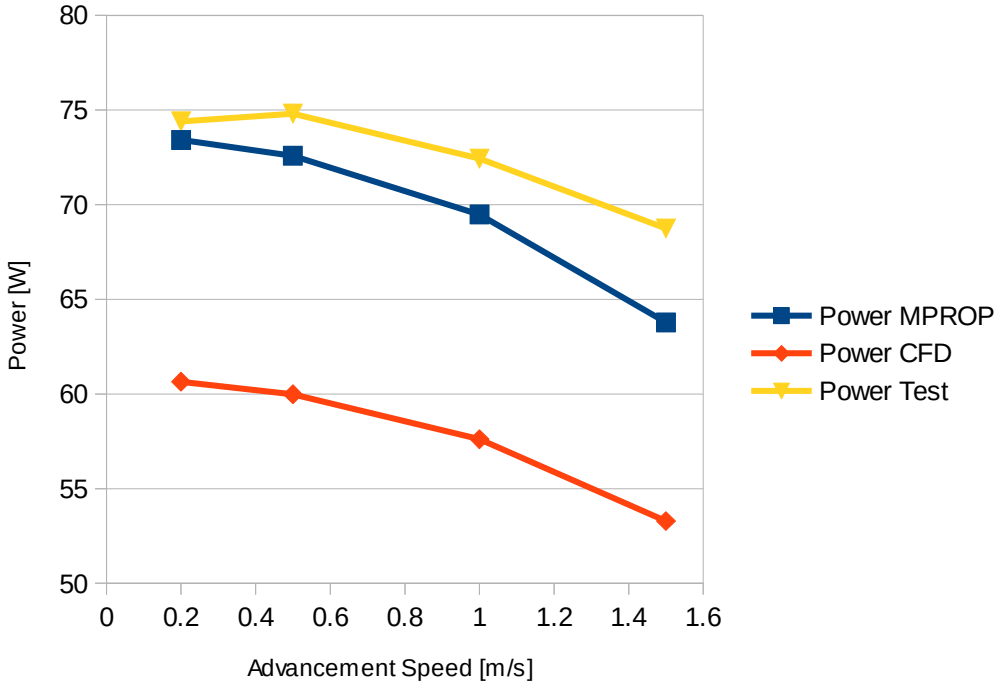

Figure 47: Hydraulic power curves obtained from MROP, CFX and tests.

5.4. References

[1] E. L. Lebedev et al., **Ship steering units**, Sudostroenie, (1969).

[2] A. Y. Yakovlev et al., **Numerical Design and Experimental Verification of a RIM-Driven Thruster**, Second International Symposium on Marine Propulsors smp'11, Hamburg, Germany, 2011.

[3] A.W. Hughes et al., **Use of an Electromagnetic Rim Driven Propulsor for Waterjet Propulsion Systems**, RINA Trans. A: Int'l J. of Maritime Engineering, 145, (A4), 41-52, 2003.

[4] T. P. Andersen, **Design of Rim Driven Waterjet Pump for Small Rescue Vessel**, Master's Thesis, Chalmers University of Technology, 2014.

[5] S. M. Abu Sharkh et al., **Performance of a Tip-Driven Electric Thruster for Unmanned Underwater Vehicles**, Eleventh International Offshore and Polar Engineering Conference, Stavanger, 2001.

[6] A.W. Hughes et al., **Design and Testing of a Novel Electromagnetic Tip-Driven Thruster**, Tenth International Offshore and Polar Engineering Conference, Seattle, 2000.

[7] A. J. Dubas, **Robust Automated Computational Fluid Dynamics Analysis and Design Optimisation of Rim Driven Thrusters**, Ph.D. Thesis, University of Southampton, 2014.

Page intentionally left blank

6. Conclusion

A study about inlet and pump system of a waterjet was done. In chapter 3 a different configuration from the traditional flush one was proposed and analysed showing the benefit of using a scoop inlet. A numerical tests campaign was done comparing a commercial Castoldi waterjet flush inlet and a scoop Boundary Layer Ingesting inlet derived from NASA studies at different speed and mass flow rates. The analysis showed that in the tested conditions the scoop inlet over performed the flush inlet in term of total pressure losses and flow distortion on the pump interface, revealing that there is still expensive room for improvements for this component and that, apparently, there are no scientific reasons to do not consider a scoop inlet as the main option for a waterjet inlet.

In chapter 4 a new method to design a generic duct propeller and to predicts its performance in the off design conditions was described. In chapter 5 an experimental campaign on a low loaded Rim Driven Propeller was detailed; the RDP was designed using the iterative method mentioned above with the aim of validate the method. The results obtained were totally satisfactory; the error in the estimation of the thrust was lower than 3% and whereas the error in the estimation of the power was lower than 7.5% demonstrating that, at least for the analysed test case class of propellers, the method its reliable and able to fast predict the performance of a duct propeller; this gave also the evidence that these kind of methods are still very significant in the framework of a procedure for a propeller design and analysis.

Page intentionally left blank

7. Acknowledgements

Many thanks to the University of Southampton, where I spent few but happy moments, to S. M. Sharkh, that welcomed me and helped in the design of the RDP, and to Aleksander Dubas that helped me many times and with whom I discussed with pleasure.

Many thanks to the TSL technology which gave me the opportunity of design and test an RDP without any assurance about successful results.

Many thanks to my friends and colleagues Giovanni Venturelli and Gianluigi Mistè that helped during these years with useful advices and happy moments.